Heavy Ion Physics with the ATLAS Detector at the LHC

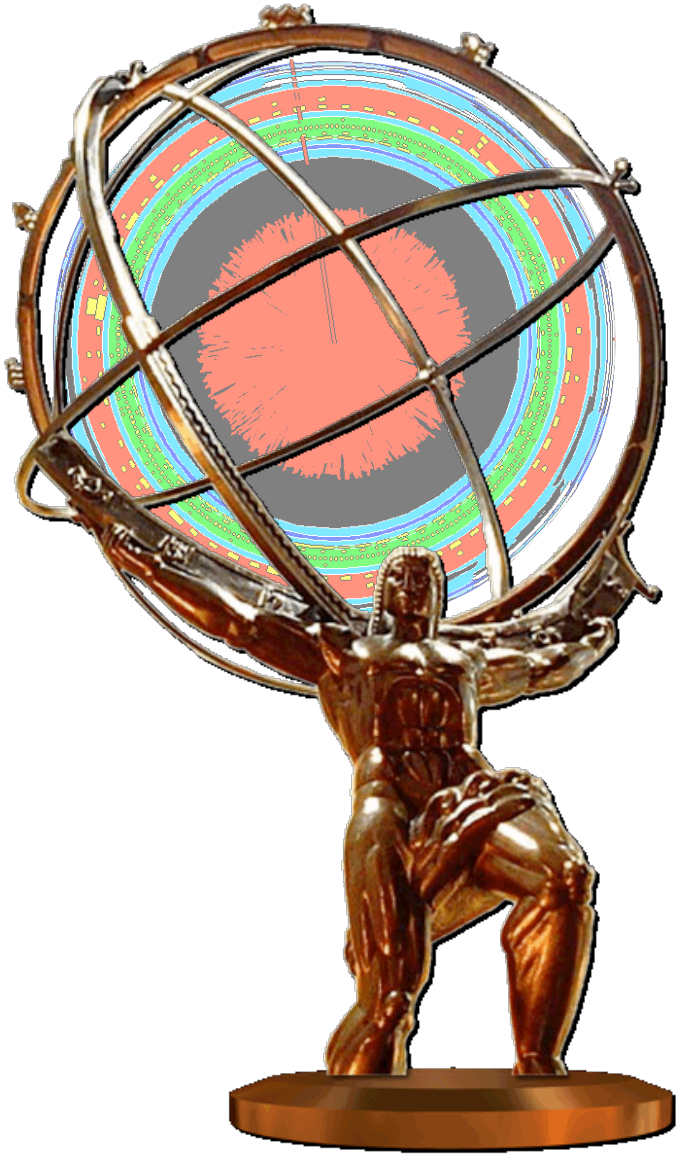

Heavy Ion Physics with the ATLAS Detector at the LHC

M.D. Baker, R. Debbe, P. Steinberg, F. Videbaek, S. White
Physics Department, Brookhaven National Laboratory, Upton, NY 11973

S. Bathe
RIKEN/BNL Research Center, Brookhaven National Laboratory, Upton, NY 11973

A. Angerami, B. Cole, N. Grau, W. Holzmann
Physics Department, Columbia University and Nevis Laboratories, Irvington, NY 10053

J. Hill, A. Lebedev, M. Rosati
Physics Department, Iowa State University, Ames, IA 50011

A. Ajitanand, P. Chung, J. Jia[1], R. Lacey
Chemistry Department, Stony Brook University, Stony Brook, NY 11794

(June 24, 2008)

[1] Also *Physics Department, Brookhaven National Laboratory, Upton, NY 11973.*

Abstract

The ATLAS experiment will participate in the Heavy Ion program at the Large Hadron Collider (LHC) and will use its large acceptance, high granularity calorimeters, silicon tracking detectors, and muon spectrometers to study hard scattering processes and jet quenching, quarkonia production and suppression, and global observables in Pb+Pb collisions. The longitudinal and fine transverse segmentation of the ATLAS electromagnetic calorimeter gives ATLAS unique capabilities for measuring complete jets and photons. Brookhaven National Laboratory, Columbia University, Iowa State University, and Stony Brook University propose a focused program to take advantage of ATLAS's strengths to study the physics of high-energy parton interactions with the quark-gluon plasma (QGP), the physics of Debye screening of Q-$\bar{Q}$ states in the QGP, and the physics of initial particle production and thermalization to characterize the properties of the QGP created in heavy ion collisions at the LHC. The proposed program can be accomplished for modest cost, will provide substantial physics impact and will have a positive impact on the physics program at the Relativistic Heavy Ion Collider (RHIC) due to the strong involvement of the proposing institutions in the RHIC program. Participation of US groups will strengthen the existing (and growing) ATLAS heavy ion program by bringing physics and analysis expertise developed at RHIC and will allow the US Nuclear Physics program to participate in an experiment that will have subtantial physics impact on the heavy ion community.

Contents

Chapter 1

Physics motivation and US ATLAS Heavy Ion goals

This chapter outlines the physics arguments for a US ATLAS Heavy Ion program starting with an overview of the current status of the RHIC program. It then describes how the LHC heavy ion program should help address many of the questions raised by the RHIC program and, potentially, make new discoveries. The ATLAS detector is described in brief with a focus on the unique features of the detector that will address some of the most important outstanding physics issues. The chapter concludes with a statement of the proposed research program, a discussion of the relationship of that program to the RHIC program, and a description of the structure of the remainder of the document.

1.1 RHIC program and current status of the field

Creation and study of the quark-gluon plasma (QGP) in the laboratory via high energy collisions of heavy nuclei has been one of the primary goals of the US and world-wide nuclear physics communities for the last few decades. This physics topic has been consistently identified in NSAC long-range plans over the last two decades as one of the top three priorities of the US nuclear physics community (e.g. [1]). The primary goals of the world-wide ultra-relativistic heavy ion effort are to understand the behavior of quantum chromodynamics (QCD) at high temperature where strongly interacting matter is deconfined [2, 3, 4, 5, 6] and to provide new insight on the properties of QCD in a regime where ordinary perturbative calculations are not possible. These goals are motivated by the possibility that strong interactions in the high temperature regime may exhibit unexpected characteristics that do not obviously follow from perturbative considerations. A first step on the path to accomplishing this goal is the creation of the QGP in the laboratory.

The experimental program at the Relativistic Heavy Ion Collider (RHIC) facility has largely accomplished this first goal [7, 8, 9]. While no individual RHIC results provides unequivocal evidence for deconfinement or chiral symmetry restoration, a consensus is developing in the RHIC and the world-wide ultra-relativistic heavy ion community that the full set of RHIC results can only be understood in the context of QGP formation shortly after the collision of two nuclei [10, 11, 12, 13]. More important, however, is the fact that the observation of strong elliptic flow at RHIC [14, 15, 16] has produced a paradigm shift in thinking about the properties of the quark-

gluon plasma at temperatures above, but near, T_c [6, 7]. Namely, there is a now a consensus in the heavy ion community that the QGP created in heavy ion collisions at RHIC is strongly-coupled (a state called the "sQGP"), with very small shear viscosity to entropy ratio η/s [17, 18]. This deduction from the RHIC data has fueled strong interest in the use of string theory methods, via the AdS/CFT correspondence, [19, 20, 21] to perform calculations relevant to RHIC results (see Refs. [22, 23, 24, 25, 26] and [27] and references therein). Thus, in addition to providing the first widely accepted demonstration of QGP formation in the laboratory, the RHIC program has also produced a major conceptual advance in understanding the properties of the QGP and is driving new theoretical techniques to understand QCD in the strong-coupling limit.

The observation of strong jet quenching at RHIC [28, 29, 30, 31] has been a critical ingredient in the development of the consensus that nuclear collisions at RHIC produce the quark-gluon plasma. Measurements in the high-p_T sector at RHIC have produced several startling and important results, all potentially providing information on the mechanisms by which a high momentum quark or gluon interacts with the medium. These include single high-p_T hadron suppression [28, 29, 30, 32, 33], disappearance of the di-jet signal in di-hadron correlations [31], strong quenching of heavy quarks observed via single electrons [34], the observation of strongly modified di-jet angular correlations [35] suggestive of a Mach cone, and long-range pseudo-rapidity correlations of moderate-p_T hadrons with a high-p_T trigger hadron [36]. High p_T quarks and gluons provide an essential probe of QGP properties since the quenching of these particles is directly sensitive to the mechanisms by which the quarks and gluons interact with the medium [37, 38, 39, 40, 41]. Ideally, jet quenching measurements would allow us to determine whether high-p_T quarks and gluons interact with individual color charges in the medium or whether they have collective/longer-range/non-perturbative interactions with the medium [42]. Answering this question would provide valuable insight on the mechanisms by which the strong coupling of the sQGP is achieved.

However, in spite of the great successes of the RHIC program and the conceptual advances that have resulted from RHIC results, there exists no single framework within which to understand the full set of energy loss results and there is, as yet, no unique, quantitative measurement of medium properties – either of transport properties(e.g. η/s) or quenching parameters (e.g. $\hat{q}$). The community does not understand the physics producing the strong coupling, the mechanism for the apparent rapid thermalization of the created matter, the physics responsible for light quark and gluon quenching, the origin of the heavy quark quenching, or whether we are seeing Mach cones. While future theoretical efforts and future measurements at RHIC will surely advance the current understanding, we will show in this proposal how measurements at the LHC using the ATLAS detector can make important and unique contributions that we believe will substantially advance the understanding of the nature of the quark gluon plasma.

New insight is particularly needed in the area of jet quenching. None of the striking results in the high-p_T sector described above is fully understood or *uniquely* explained by a single theoretical description of the interaction of high-p_T quarks/gluons in the QGP. Attempts to extract quantitative information from RHIC data produce dramatically different results [43] due to theoretical disagreements over the role of collisional energy loss [44, 45, 46], the effects of transverse flow on energy loss [47, 48], different approximations used in the energy loss calculations and different treatments of the strong coupling constant. Unfortunately, the most precise measurements from RHIC – single hadron suppression – provide little ability to constrain theoretical descriptions of energy loss [49, 50], and even di-hadron measurements appear to be relatively insensitive to the energy loss mechanisms in the p_T range currently accessible at RHIC [50]. To complicate the situ-

ation further, it has been argued that measurements of heavy quark quenching via single-electron suppression at RHIC [34, 51], and the relative suppression of pion and proton yields at high p_T [52] could indicate contributions from non-perturbative energy loss mechanisms. This current situation partly results from a lack of convergence in the theoretical understanding of jet quenching, but it also is due to the fact that p_T reach of the measurements at RHIC is limited and the fact that all the quenching measurements are made with hadrons instead of complete jets. The reliance on hadrons causes serious energy loss biases in measurements of single hadron and di-hadron suppression [49] and makes all quenching measurements "indirect" – since the quark/gluon jet is never observed. Jet quenching provides potentially one of the most important tools for understanding medium properties, but a qualitative change in the way the measurements are performed, namely making measurements with complete jets, is essential to improving the current confused situation.

Another important physics problem raised by the RHIC program is that of Debye screening of quarkonium states. To date, J/ψ measurements at from RHIC and the SPS have defied straightforward interpretation, so it cannot yet be concluded that the effects of Debye screening of $Q\bar{Q}$ states in the quark-gluon plasma have been observed experimentally. This situation is due to the many difficulties with the interpretation of J/ψ measurements including uncertainties regarding the production process, limited understanding of cold [53] and hot hadronic absorption/dissociation processes, and the possible effects of J/ψ formation via coalescence of $c\bar{c}$ pairs [54]. There is also the important question of whether the J/ψ will survive in the QGP at temperatures well above T_c [55, 56, 57]. This last issue is of particular importance as the unexpected similarity of J/ψ suppression seen at RHIC and the SPS has been explained as resulting from the combination of survival of primordial J/ψ in the medium and quenching of other $c\bar{c}$ states that feed into the J/ψ[55]. The ψ' has not yet been measured at RHIC because of its small production rate, so no study comparing the suppression of different $c\bar{c}$states and testing the expected lower dissociation temperature of the ψ' is yet available at RHIC. Well-understood experimental measurements of quarkonium dissociation will provide a powerful tool for testing theoretical predictions of Debye screening in the QGP and will, as a result, provide valuable insight on the properties of the QGP. As will be discussed below, measurements of bottom quarkonium states – especially a the LHC – have the potential to provide such tests.

Another area where LHC measurements can make a significant impact is in the physics of saturation at low x and the study of the "colored glass condensate" (CGC). There is no consensus regarding how much the initial particle production at RHIC is influenced by strong field effects in the nuclear wave functions. Theoretical studies have shown that saturation effects can sufficiently modify the initial conditions for the evolution of the quark-gluon plasma to undercut some of the conclusions drawn from the RHIC data [58]. But, while calculations based on saturation qualitatively predicted the low multiplicities at RHIC and while more detailed saturation models can provide an excellent *post facto* description of initial particle multiplicities and pseudo-rapidity distributions at RHIC [59, 60], these calculations cannot be tested properly until we can compare their predictions [61] to measurements at higher energies where much lower x values can be probed.

To summarize, the success of the RHIC program has generated a number of new and important physics questions and problems that are as yet unsolved. New measurements at higher energy, probing physics at low x, and using full jets to probe the properties of the medium have the potential to advance the field and provide new insight on the properties of the QGP and the nature of the strong interaction at high temperature.

1.2 LHC Heavy Ion program

The start of the LHC Heavy Ion program in 2009 or 2010 will surely produce as dramatic a revolution in the study of the quark-gluon plasma in the laboratory as RHIC produced when it first started operation in 2000. Pb+Pb collisions at the LHC are expected to produce a quark gluon plasma with initial energy density roughly an order of magnitude larger than at RHIC [62, 63], with larger ($\times$ 2) initial temperatures [62] and longer lifetimes ($\times$ 1.5) for the QGP [62] than achieved at RHIC. The increase in the collision energy from RHIC to the LHC will provide a critical test of the application of saturation-inspired models in the description of A+A particle multiplicities (see section 4). Measurements of elliptic flow resulting from the higher initial energy densities will test our interpretation of elliptic flow results from RHIC.

Arguably, the most important component of the LHC heavy ion program will be the measurements of jet quenching and the use of jets as a tomographic probe of the medium. The increase in hard scattering cross-sections between the top RHIC energy ($\sqrt{s_{\rm NN}} = 200$ GeV) and the LHC ($\sqrt{s_{\rm NN}} = 5.5$ TeV for Pb+Pb) [64] will extend the p_T range accessible in quenching measurements by at least a factor of 10. For example, a single Pb+Pb run at design luminosity will produce nearly a million jets with $E_T > 100$ GeV[64]. As a result of the copious production of high-energy jets at the LHC, full jet measurements will finally be possible in Pb+Pb collisions, and these measurements should dramatically improve the understanding of jet quenching mechanisms. The energy loss bias will be reduced to the extent that a high-energy quenched jet should still be reconstructed, even if radiative energy loss produces a re-distribution of energy within the jet [65]. Direct measurement of the modified fragmentation functions of the jets [66] will provide more detailed tests of energy loss calculations, thereby reducing the current theoretical ambiguities and improving the utility of quenching measurements as probes of the QGP. Measurement of the inclusive jet E_T spectrum will, in principle, provide sensitivity to collisional energy loss [67, 68] as well as exhibit effects from non-perturbative energy loss that might transfer radiated energy to the medium [24]. The statistics for bottom and charm jets will be sufficient to perform detailed measurements of heavy quark quenching at high E_T. The rate for hard photon-jet processes will be sufficient to allow measurements of photon-tagged jet quenching for photon and jet transverse energies up to 100 GeV. Measurement of the acoplanarity of di-jet pairs at the LHC should provide sensitivity to the expected angular diffusion of high-p_T partons in the medium – an unavoidable consequence of radiative and collisional energy loss [69] that has, so far, eluded detection at RHIC. The large rates for jets will make possible the measurement of all of the above observables as a function of collision centrality, angle with respect to the event plane, and pseudo-rapidity. Taken together, these measurements will provide a degree of sensitivity to the physics of jet quenching that will be difficult to achieve at RHIC. Hard-scattered quarks and gluons may be the only probes that we have that are directly sensitive to the nature of the interactions in the medium. Thus, an improved understanding of the physics of quark and gluon interactions with the medium is essential; full jet measurements at the LHC are the most likely means to accomplish this goal.

The LHC will also provide a new opportunity to explore the physics of deconfinement through the measurement of both charm and bottom quarkonium states. In particular, the ability to measure $b\bar{b}$ quarkonia states has the potential to dramatically improve the current confused situation with experimental probes of deconfinement. Bottom production requires a Q^2 roughly a factor of ten larger than that required for charm production so the production process is harder and, in principle, more amenable to pQCD calculation though theoretical uncertainties in how $b\bar{b}$ pairs

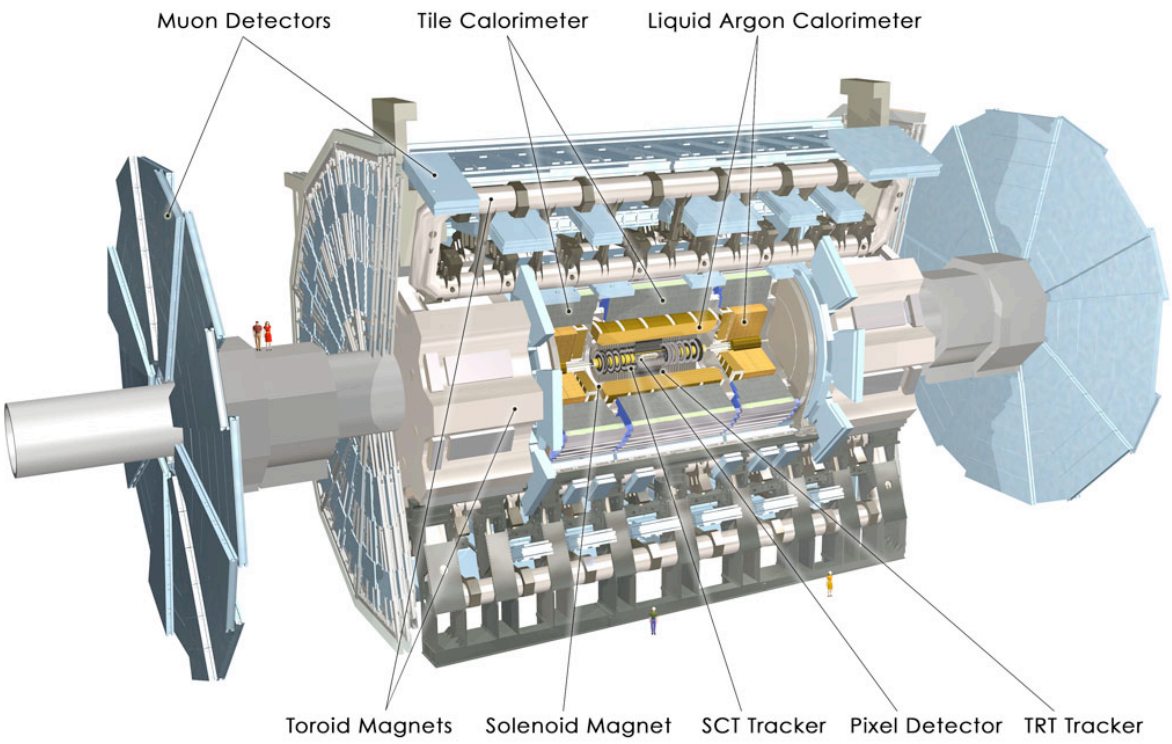

Figure 1.1: The ATLAS detector at the LHC

evolve into Y states persist. The relative yield of the Y and Y′ states is expected to be closer than the yields of ψ and ψ' [61] making comparison of states with different nominal screening scales easier. Also, recent analyses of the temperatures at which the different quarkonia states melt [57] show that that the Y is the only state that survives to $2T_c$. The relatively low multiplicity of $b - \bar{b}$ pairs in Pb+Pb collisions at the LHC is expected to give little recombination contribution to production of Y states [61]. Thus, while it would be naive to assume that Y measurements will be completely free of complications, there is good reason to expect that the measurement of Upsilon production and suppression at the LHC will significantly advance the understanding of Debye screening/deconfinement in the QGP. Certainly, the Y states provide the first new experimental tool for studying Debye screening in the QGP since the advent of J/ψ suppression measurements in NA38 nearly two decades ago [70].

1.3 ATLAS detector

Figure 1.1 provides a schematic view of the ATLAS detector showing all major detector components. The detector can be viewed as having three largely independent detector systems: the inner detector, the calorimeters, and the muon spectrometers. The inner detector consists of silicon pixel (Pixel), silicon strip (SCT), and transition radiation tracker (TRT) detectors. The calorimeter system consists of barrel and end-cap liquid argon electromagnetic calorimeters, a traditional hadronic calorimeter (Tile Calorimeter), end-cap liquid argon hadronic calorimeter, and forward

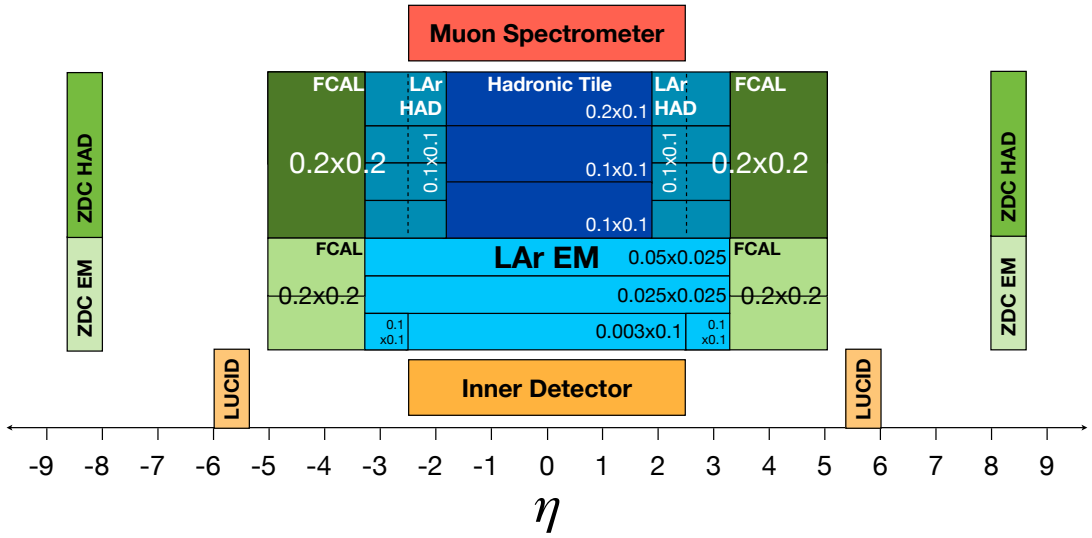

Figure 1.2: The pseudo-rapidity coverage of various components of the ATLAS detector by layer.

EM and hadronic calorimeters. The muon spectrometers consist of toroidal magnets and tracking detectors covering both the barrel and end-cap regions of the detector.

The pseudo-rapidity coverage of the ATLAS detector broken out into its various detector components is shown in Fig. 1.2. The ATLAS calorimeters allow measurement of jets over the pseudo-rapidity interval $|\eta| < 5$, identified photons over the interval $|\eta| < 2.4$ and charged particles over the interval $|\eta| < 2.5$. The muon spectrometers, covering $|\eta| < 2.7$ allow measurement of Y states over a range $|\eta| < 3.5$. A forward luminosity monitoring detector will provide $dN_{ch}/d\eta$ measurements over $5.4 < |\eta| < 6.1$. The ATLAS ZDC (see Chapter 6) will cover $|\eta| > 8$ for neutral particles, both neutrons and photons.

One of the unique components of the ATLAS detector relevant to this proposal is the liquid argon electromagnetic calorimeter shown in a diagram of the full ATLAS calorimeter system in Fig. 1.3. The electromagnetic calorimeter, broken into separate "Barrel" and "End-cap" sections as shown in Fig. 1.3, is longitudinally segmented into three layers with the first layer consisting of "strips" that are finely segmented in the η direction ($\Delta\eta \approx 0.003$). This fine segmentation of the first EM sampling layer extends over $|\eta| < 2.4$ and provides valuable separation between single photons and photon pairs produced in neutral hadron (primarily π^0 and η) decays. Because of the fine segmentation of the first sampling layer, this separation can be utilized for neutral hadron transverse momenta as large as 100 GeV/c (see Chapter 3). The longitudinal segmentation of the EM calorimeter allows for improved compensation and provides the best intrinsic jet energy resolution of the detectors at the LHC. The clear advantages of the ATLAS calorimeters for performing jet, di-jet, γ-jet, etc. measurements and the importance of the jet quenching measurements at the LHC provides an overwhelming case for ATLAS participation in the LHC heavy ion program.

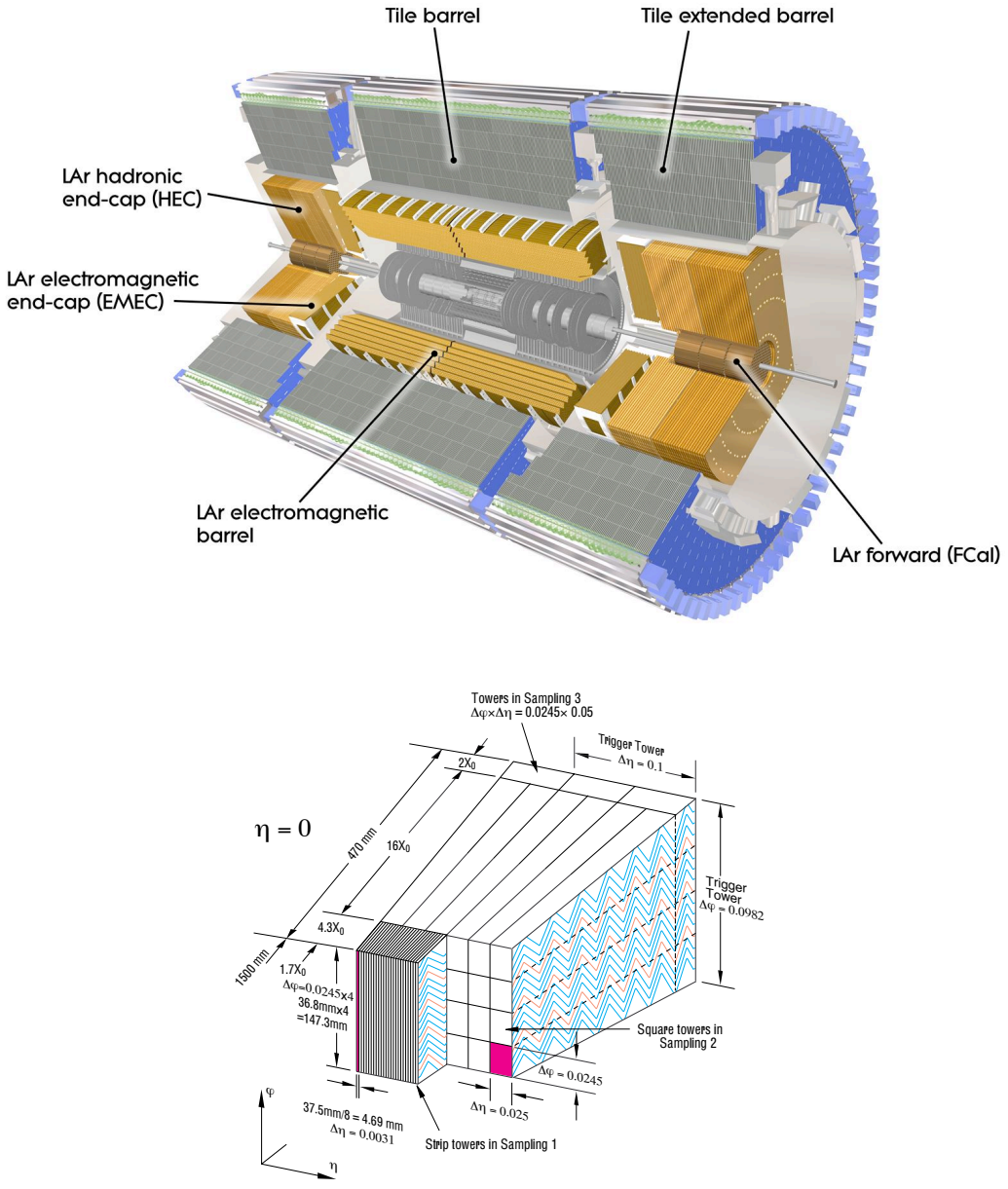

Figure 1.3: (top) Diagram of the ATLAS calorimeter system (bottom) Diagram showing longitudinal segmentation of ATLAS electromagnetic calorimeter.

1.4 ATLAS Heavy Ion program

ATLAS first started serious discussions regarding participating in the LHC heavy ion program in 2001. In the Spring of 2004, ATLAS submitted a Letter of Intent to the LHC Experiments Committee (LHCC) [71] proposing a heavy ion program that would focus on global observables and hard probes (jets, photons, and quarkonia). The eventual decision by the ATLAS experiment to participate in the LHC heavy ion program was motivated by the fact that the ATLAS detector has several advantages in carrying out heavy ion measurements – especially in the measurement of jets and photons.

- Large acceptance, high quality electromagnetic and hadronic calorimeters with fine transverse segmentation and longitudinal segmentation.
- Nearly hermetic external muon spectrometers.
- High precision silicon inner detector.
- High-rate trigger and data acquisition system designed for triggering on rare, high-p_T particles/jets.

On receiving positive encouragement from the LHCC, ATLAS made heavy ion measurements an official part of the ATLAS scientific program and established a Heavy Ion working group to carry out the goals described above. The scientific program described in this proposal is an integral part of the ATLAS Heavy Ion working group's plans and is coordinated with the remainder of the institutions participating in the ATLAS Heavy Ion program (see Section 9.5).

1.5 Proposed US ATLAS Heavy Ion program

This proposal describes a plan by institutions in the US (US ATLAS-HI) to take advantage of the unique strengths of the ATLAS detector to pursue a focused study of hard processes in heavy ion collisions at the LHC with the goal of using jet quenching and quarkonia measurements to provide detailed, quantitative information about the properties of the quark-gluon plasma created in heavy ion collisions at the LHC. To accomplish this goal, we will also participate in measurements of global observables in Pb+Pb collisions as these will be essential for constraining bulk properties of the medium and providing reaction plane measurements that will be essential for performing differential measurements of quenching as a function of path length in the medium [72]. We will also participate in p+p measurements as needed to provide the necessary baseline measurements for the Pb+Pb program

We plan to participate in first measurements of charged particle $dN_{ch}/d\eta$, $dE_T/d\eta$ and charged particle, electromagnetic and hadronic elliptic flow in Pb+Pb collisions at the LHC. The $dN_{ch}/d\eta$ measurements will be performed over the range $|\eta] < 2.5$ and $5.4 < |\eta| < 6.1$. The electromagnetic $dE_T/d\eta$ measurements will be performed over the range $|\eta| < 3.2$ while the total $dE_T/d\eta$ measurements will be performed over the range $|\eta| < 5$. Charged particle v_2 measurements will be made over the pseudo-rapidity interval $|\eta| < 2.5$ while calorimetric v_2 measurements will be performed over the range $|\eta| < 5$.

We will measure jet energy spectra, jet charged particle fragmentation functions, jet charged particle j_T distributions, jet shapes, and di-jet angle and energy correlations to separately quantify

collisional and radiative energy loss of hard-scattered partons in the quark-gluon plasma. We will use a combination of muon tagging and displaced vertex tagging to separately measure bottom and charm quark energy loss. A combination of direct photon identification and photon isolation will be used to perform high-statistics measurements of prompt photon production and γ-jet pairs to calibrate and further improve the precision of the jet quenching measurements and to extend jet measurements to low E_T. We propose to use the unique capabilities of the ATLAS electromagnetic calorimeter to statistically measure prompt photons down to and possibly below 10 GeV with the goal of detecting jet-conversion photons and medium-induced photon bremsstrahlung associated with jets. The wide calorimetric coverage and tracking coverage of the ATLAS detector will be used to study the medium response to the passage of high energy jets with the goal of clarifying the exciting, but poorly understood jet modifications observed at RHIC. We will make all of the above measurements as a function of collision centrality, angle with respect to the event reaction plane, and pseudo-rapidity. We will measure jets over the pseudo-rapidity range $|\eta| < 5$, photons over the range $|\eta| < 2.4$, and charged hadron fragmentation over the range $|\eta| < 2.5$.

The quarkonia portion of the proposed program focuses on measurement of Upsilons (Y) over the pseudo-rapidity range $|\eta| < 3.5$ with sufficient mass resolution to resolve the Y and the Y$'$ states. The Y and Y$'$ measurements will, by themselves, provide a direct probe of Debye screening of quarkonium states. Direct photon, Z, single muon, and muon tagged jet measurements will provide benchmarks for Y suppression within the Pb+Pb measurements and will be used to assist interpolation of full energy p+p Y measurements to $\sqrt{s_{\rm NN}} = 5.5$ TeV.

1.6 Connection with RHIC, RHIC-II programs

The scientific programs at RHIC and the LHC will be complementary and, together, will provide a comprehensive study of the properties of the quark-gluon plasma over an estimated initial temperature range $T_c < T < 5T_c$. Results from both programs will be required for the development of a systematic understanding of how the QGP is formed from initial semi-hard partonic scattering and emission, how it thermalizes, how it evolves dynamically, and how it hadronizes. Results from the LHC and RHIC will surely influence the thinking about results from the other program. In particular, measurements from the LHC that test concepts developed using RHIC results will certainly have an immediate and important impact on the RHIC program.

The interaction between the RHIC and SPS Heavy Ion programs provides a good model for the positive impact that the LHC Pb+Pb program will likely have on the RHIC program. In many places, but especially in the area of jet quenching, results from RHIC stimulated analysis of SPS data that would otherwise never have been performed – often with surprising and interesting results. A good example is provided by the strong distortion of the di-hadron correlation seen at RHIC [35]. This result from RHIC stimulated similar investigations by the CERES experiment which found similar features [73, 74] in their data. The fact that a similar modification of the di-jet shape is observed at SPS energies, where the p_T range of hard processes is extremely limited and where quarks dominate, necessarily constrains theoretical interpretations of the effects. The synergy between the SPS and RHIC programs has provided a substantial net benefit for the field as a whole. However, unlike the situation at the SPS where the heavy ion program was largely shut down when RHIC started operation, RHIC will be able to take full advantage of the insights gained from the LHC program and systematically explore the consequences of those insights –

something that the LHC will not be able to do because of limited heavy ion running time. The institutions participating in the ATLAS Heavy Ion program have a history of strong involvement in and leadership of the RHIC heavy ion program and will use that involvement to facilitate the feedback of advances from the LHC program to the RHIC program and vice versa.

1.7 Proposal structure

The remainder of this document is structured as follows: Chapter 2 more fully explains the physics motivation and goals of complete jet measurements at the LHC and summarizes the ATLAS performance in carrying out full jet measurements in a heavy ion background. Chapter 3 describes the physics motivation for direct photon and photon-jet measurements and shows the results of studies of background rejection and direct photon efficiency in heavy ion collision along with reconstructed photon-jet correlations. Chapter 4 describes in more detail the physics impact of global measurements and shows results from studies of $dN_{ch}/d\eta$, $dE_T/d\eta$, event plane reconstruction and v_2 measurement. Chapter 5 describes ATLAS quarkonia measurements and the physics impact of these measurements. Chapter 6 describes the nearly completed ATLAS zero degree calorimeter and the contribution of the calorimeter to the ATLAS Heavy Ion program. Chapter 8 describes the specific US computing needs for heavy ion physics and describes a plan to satisfy those needs. Chapter 9 provides a management plan and describes operational needs for the ATLAS Heavy Ion program. Chapter 10 summarizes the motivation for the ATLAS Heavy Ion program and US participation in the program and summarizes the results shown in Chapters 2 through 5 from physics performance studies to illustrate the unique contributions that ATLAS will make to the LHC Heavy Ion program.

Chapter 2

Jet reconstruction and measurement

This chapter describes the physics motivation for complete jet measurements in heavy ion collisions at the LHC extending the discussion from the introduction, and shows results for ATLAS jet reconstruction performance in Pb+Pb collisions. It also shows results on measurements of jet fragmentation properties, di-jet correlations, and heavy-flavor tagged jets.

2.1 Physics motivation

As emphasized in Chapter 1, a major aspect of the heavy ion physics program at the LHC is the extension and clarification of the understanding of the effects of hot, dense QCD matter on hard probes, specifically jets. Prior to RHIC startup, several groups predicted the energy loss of a fast-moving, colored parton traversing a colored medium via perturbative gluon bremsstrahlung and multiple elastic scattering, leading to "jet quenching" [38, 75]. Evidence for this pQCD energy loss has been established through the measurement of high-p_T single particle suppression [28]. The suppression is quantified by the nuclear modification factor, R_{AA}, defined as the ratio of single particle yields in Au+Au collisions, Y_{Au+Au}, compared to p+p single particle rates, Y_{p+p}, scaled by the number of binary nucleon-nucleon collisions (N_{coll}):

$$R_{AA} = \frac{Y_{Au+Au}}{\langle N_{coll} \rangle Y_{p+p}}. \tag{2.1}$$

The nuclear modification factor for three different particle species, measured by PHENIX, is shown in the left panel of Fig. 2.1: direct photons, which do not strongly interact in the nuclear medium, are not suppressed while a factor of 5 suppression is measured in π^0 and η production. The level of π^0 suppression is apparently consistent with a particular pQCD energy loss model [40]. However, it has been argued, many models of energy loss can describe this data even when the details of the mechanism and implementation differ greatly between those models[76].

Further evidence for jet quenching comes from the azimuthal correlation of two high-p_T particles. These serve as a proxy for direct jet reconstruction, which is difficult at RHIC due to the high-multiplicity underlying event. Two-particle correlations in p+p suggest that high-p_T particle production is dominated by hard scattering [31, 79]. Two high-p_T particles from the trigger jet are correlated at $\Delta\phi \sim 0$ while two high-p_T particles at $\Delta\phi \sim \pi$ are fragments from a di-jet pair. Such correlations are seen in the histogram on the right panel of Fig. 2.1. Measurements of

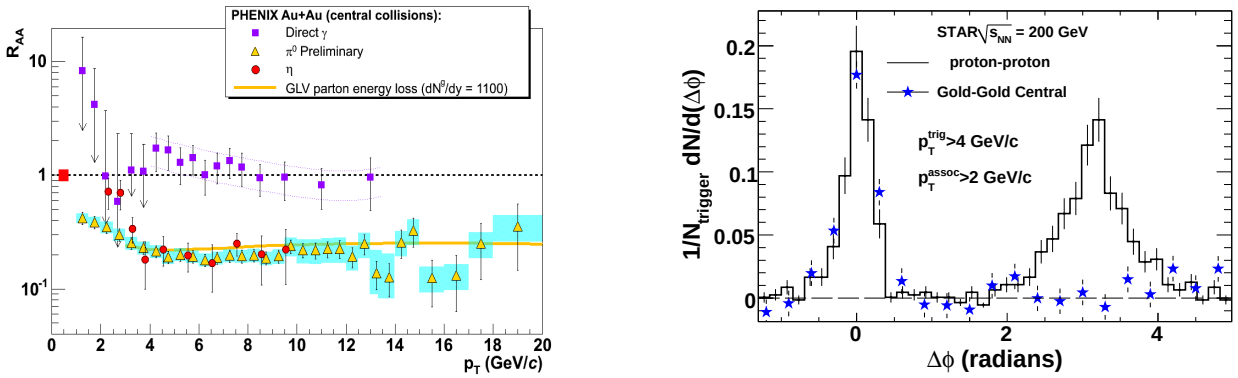

Figure 2.1: (left) Nuclear modification factor for direct photons, π^0, and η [77]. R_{AA} <1 is evidence of jet energy loss. (right) Azimuthal angle ($\Delta\phi$) correlations of two high-p_T charged hadrons [78] with trigger hadron $p_T > 4\,\mathrm{GeV/c}$ and associated hadron $p_T > 2\,\mathrm{GeV/c}$. The recoil jet (at $\Delta\phi \sim \pi$) is strongly suppressed in central Au+Au compared to p+p correlations [31].

these correlations in Au+Au indicate a substantial suppression of the recoil jet at $\Delta\phi \sim \pi$ while the trigger jet is essentially unmodified, as shown by the blue stars. These results suggest that the trigger jet originates from the surface of the interaction region and is unaffected by the nuclear environment while the recoil jet traverses a significant length in the medium and appears to be largely absorbed [31].

In addition to the suppression of light quarks and gluons, a quantitatively similar suppression of single, non-photonic electrons, dominantly from charm and bottom quark decays, has been observed (see the left panel of Fig. 2.2) [51, 80]. Since the heavy quark mass kinematically suppresses forward gluon radiation (a phenomenon known as the "dead cone"), heavy quark energy loss was expected to be much less than that for light quarks [82]. A comparison of the fractional energy loss from collisions and radiation of different quark species expected at the LHC is shown in the right panel of Fig. 2.2. Unfortunately, interpretation of the single, non-photonic electron suppression is not straightforward. Large uncertainties arise in calculating the charm cross-section in next-to-leading-log (NLL) Therefore, a theoretical understanding of the relative contribution of charm and bottom at a fixed electron p_T is not well constrained. Experimentally several early measurements of the charm-to-bottom ratio exist, but suffer from large statistical and systematic uncertainties.

Since these initial discoveries of energy loss of high-p_T particles, measurements sensitive to the medium's response have been made utilizing jets as probes of the medium. As shown in the left panel of Fig. 2.3, lower-p_T azimuthal correlations in Au+Au show a yield peaked at $\Delta\phi \sim \pi \pm 1.1$ rad as a "shoulder", non-existent in p+p and d+Au [35]. One possible explanation of this additional yield at these large angles is the existence of a Mach cone generated by a supersonic jet traversing the medium [83, 84]. The Mach angle is fixed by the speed of sound in the medium and, therefore, should not depend on the p_T of the particles, consistent with recent RHIC data [85]. The "shoulder" position shows a common centrality dependence at different collision energies and for different colliding species. Because the medium is similar for the energies and species considered, this indicates that the effect is a universal property of the produced medium, like the speed of sound, which would be similar across energies and geometries. Three-particle correlations, which are sensitive to differences between conical emission and bent/deflected jets, are consistent with

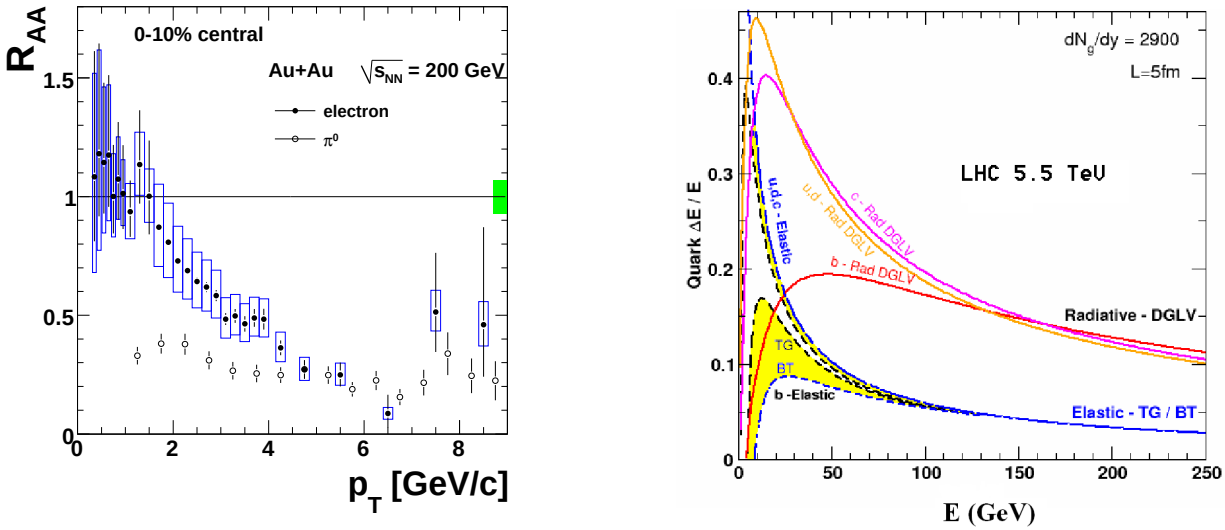

Figure 2.2: (left) The measured single particle suppression for non-photonic electrons (mainly from semi-leptonic decay of charm and bottom mesons) and π^0s from PHENIX Collaboration [80]. (right) The calculated radiative and collisional energy loss in $\Delta E/E$ for various flavor of quarks at the LHC from Ref [81].

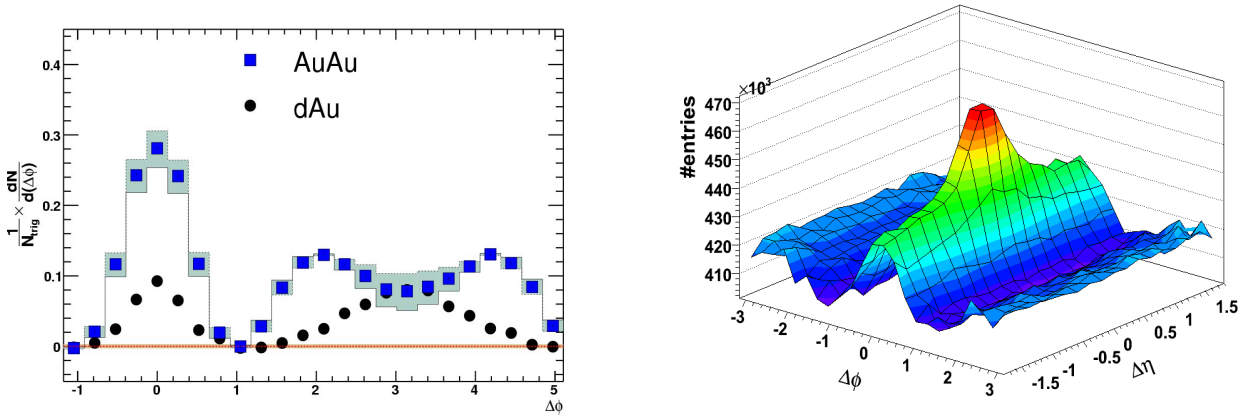

Figure 2.3: (left) Lower-p_T azimuthal correlations in central Au+Au showing a large yield at $\Delta\phi \sim \pi \pm 1.1$ rad [90]. (right) $\Delta\phi$ x $\Delta\eta$ correlations showing an extended "ridge" in $\Delta\eta$ [88]. The p_T ranges are $3 < p_T < 4$ GeV/c for trigger hadrons and $p_T > 2$ GeV/c for associated hadrons.

conical emission [86, 87].

The right panel of Fig. 2.3 shows two-particle correlations in $\Delta\phi$ and $\Delta\eta$, which reveal an extended "ridge" in η associated with the trigger jet [88]. In fact, this ridge may extend over least 4 units in $\Delta\eta$ [89]. Despite the increasing number of confirming experimental measurements, the interpretation of this observation is still debated. It should be noted that these results on the medium response are statistically determined from correlations rather than event-by-event. No direct observation of a cone or a ridge has been made in a single event.

With all of these exciting discoveries there are surprisingly few details that are currently under-

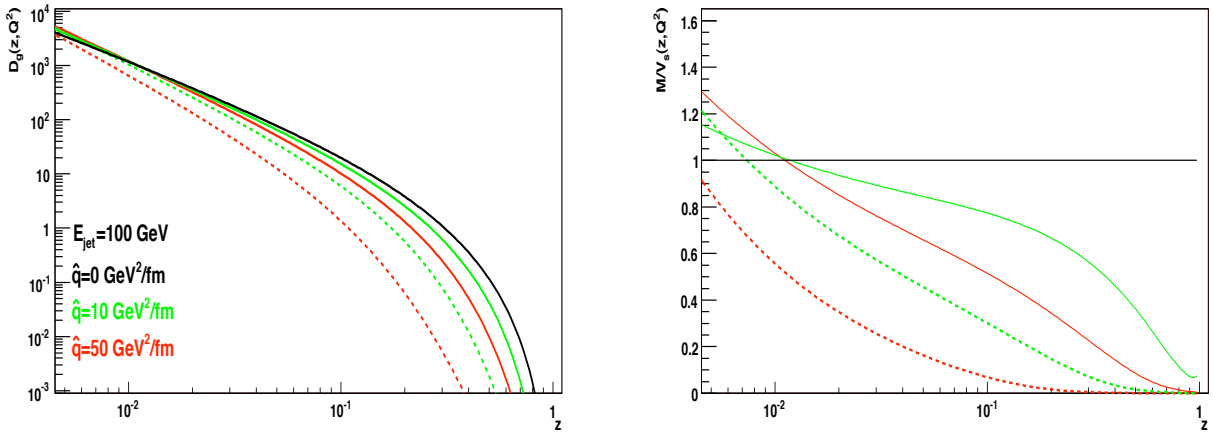

Figure 2.4: (left) Gluon to pion fragmentation functions in vacuum (black), in medium with $\hat{q} = 10\text{GeV}^2/\text{fm}$ (green) and $\hat{q} = 50\text{GeV}^2/\text{fm}$ (red) for 100 GeV jets passing through 2 fm of medium (solid) and 6 fm of medium (dashed). (right) The ratio of the in-medium modified fragmentation functions to the vacuum [92].

stood about the energy loss mechanism. Debate continues about the dominance of gluon radiation over elastic scattering at momentum scales relevant to RHIC measurements. For example, within a given model, experimental data can tightly constrain the transport coefficient or the color charge density of the medium [91]. However, models still vary greatly between each other, *e.g.* estimates of the transport coefficient differ by a factor of $\sim$10. This is due to the fact that R_{AA} shows little sensitivity to the underlying energy loss mechanism; its observed value can be reproduced by almost all existing models [76].

Understanding energy loss is also experimentally challenging because two-particle correlations are "energy-loss biased". That is, a high-p_T particle has a higher probability of being detected if it loses relatively little energy due to fluctuations in the number of scatterings (punch-through) or traversing a short path length in the medium by being emitted tangentially. Requiring two high-p_T particles exacerbates this single particle bias by requiring a second high-p_T particle from the recoil jet in the same event. Some combination of these effects probably dominates high-p_T two-particle correlations [76].

These experimental constraints can be overcome at the LHC where copious high-E_T jets will be available that should be visible above the background. This will allow, for the first time, direct jet reconstruction in a heavy ion environment on an event-by-event basis. By fully reconstructing the jet, the entire energy of the primary, hard-scattering process, including the energy lost by the primary parton, should be measurable. This will significantly reduce the energy loss biases. Of course, this assumes that the lost energy remains inside the jet cone, but this is the current expectation from standard energy loss models [65].

Once full jet reconstruction is available, jet tomography will be performed. Energy loss via gluon bremsstrahlung will be tested by studying the effects of energy loss on fragmentation functions, D(z). Here, z is the longitudinal momentum fraction of a jet carried by a fragment. An example of a modification of the D(z) in medium[92] is shown in Figure 2.4. The characteristic pattern for energy loss is the suppression of high-z (high-p_T) fragments whose lost energy is

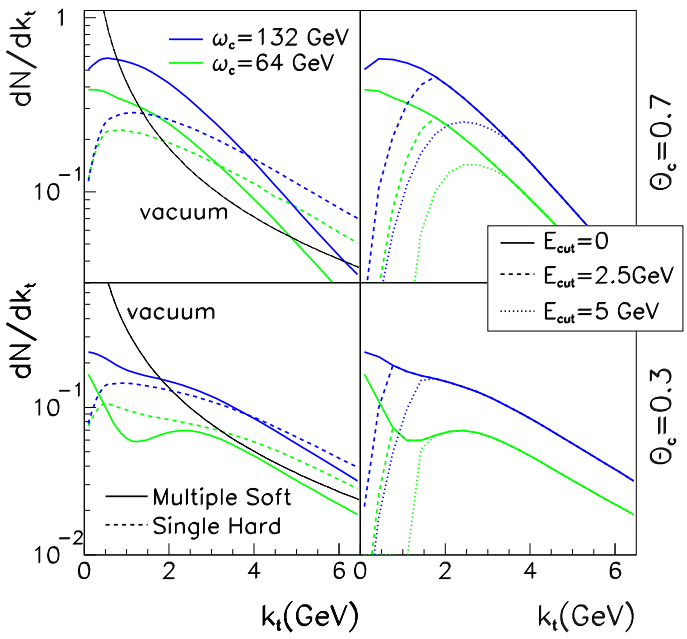

Figure 2.5: Gluon transverse momentum with respect to the jet axis (j_T in the text) distributions for different energy (E_{cut}) and angular cuts (θ_c) of the gluons. The vacuum distribution is shown in the thin solid lines. The different colored lines indicate two different medium transport properties (ω_c). Dashed lines indicate medium response and different energy cuts. Hard, in-medium gluon radiation results in increased yield at large k_t (j_T).

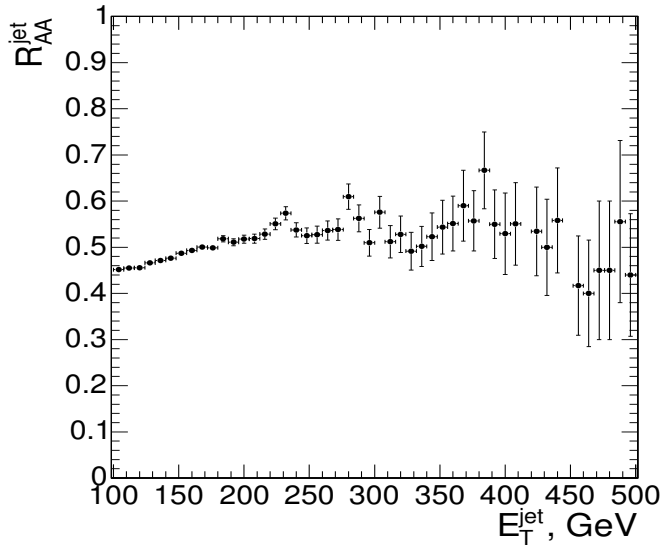

Figure 2.6: Calculated jet (cone size $R = 0.5$) R_{AA} in central Pb+Pb collisions from Ref. [67] including effects from both collisional energy loss and radiative energy loss outside the jet cone.

transported to lower-z (lower-p_T) fragments. The ratio of the modified D(z)to the vacuum D(z) is below 1 at high z and above 1 at low z.

Another tool to study gluon bremsstrahlung is by measuring the hard radiation from the interaction of the jet with the medium. This is done via the j_T distribution. Here, j_T is defined as the transverse momentum of a fragment with respect to the jet axis. The high-j_T distribution is dominated by parton splitting in the fragmentation chain and should be enhanced by the additional hard radiation from jet-medium interactions. An example of the possible modification of the j_T distribution [65] is shown in Figure 2.5. The plot shows different j_T distributions (labeled as k_t) for gluons from jet fragmentation and energy loss with different gluon energy cuts and different maximum angles from the original parton. Even with a 5 GeV cut on the gluons, which cuts away much of the underlying event background, additional gluons are measured at large j_T resulting from the hard gluon radiation in the jet.

Collisional energy loss can be studied by looking at the jet R_{AA}. If all of the lost energy was recoverable by jet reconstruction, the jet spectrum should scale with N_{Coll} like the direct photon spectrum (see Figure 2.1). Consequently, any energy lost not recoverable by full jet reconstruction, will result in the softening of the jet spectrum. Collisional energy loss results in energy imparted to the medium and, thus, not radiated within the jet cone. This softening can be measured like the single particle suppression by measuring the jet R_{AA}. An example of such jet $R_{AA} < 1$ from collisional energy loss is shown in Figure 2.6. Clearly with these observables jet reconstruction opens up new avenues of studying energy loss at the LHC.

2.2 ATLAS calorimeter and jet measurements

The ATLAS calorimeter is uniquely suited to perform full jet measurements and, thus, to make important and unique contributions to the understanding of jet energy loss and medium response to jets. The calorimeter (see Fig. 1.3) is nearly hermetic, covering 2π in azimuth, with the barrel and end-caps covering $|\eta| < 3.2$, and the forward calorimeters (FCAL) covering $3.2 < |\eta| < 5$. An active pre-sampling layer in front of the electromagnetic calorimeter improves the energy resolution for electromagnetic showers that originate in the inner detector. The calorimeter is longitudinally segmented with three electromagnetic and three hadronic measurements over most of the coverage of the calorimeter. The longitudinal segmentation of the calorimeter provides improved separation between electromagnetic and hadronic showers and is helpful in Pb+Pb collisions where the soft hadron background ranges out faster with depth than electromagnetic showers. In particular, because of the 2 T magnetic field, soft particles impact the front of the calorimeter at a shallow angle and deposit a large fraction of their energy into the first layers of the electromagnetic calorimeter. On average 60% of the background energy is deposited within the pre-sampler and first electromagnetic layer with the result that the second and third electromagnetic layers are less sensitive to soft hadron background.

As noted in Section 1.3, the fine η segmentation of the first electromagnetic layer ($\Delta\eta \approx 0.003$ in the barrel) is particularly valuable for carrying out jet measurements. The typical energy deposit in one of the cells in the first electromagnetic layer in a central HIJING [93] Pb+Pb event is $\approx$ 30 MeV while the peak energy deposit for a 1 GeV photon is typically a factor of 10 larger. Thus, electromagnetic showers from neutral hadrons and or prompt photons can be easily distinguished from the Pb+Pb underlying event (see Section 3.2).

2.3 Jet reconstruction in Pb+Pb collisions with ATLAS

The goal of the heavy ion jet analysis is to use algorithms developed for p+p measurements so that the calibrations obtained from p+p data can be used for Pb+Pb measurements with only modest adjustments. Currently, two complementary jet reconstruction algorithms are being explored: a seeded cone algorithm [94, 95] and an implementation of the k_T algorithm [96, 97, 98] optimized for fast execution time (Fast-k_T [99]). The cone and k_T algorithms differ significantly in the way they find jets, in their sensitivity to jet shape, and in the way they are adapted to the underlying event in Pb+Pb collisions. The use of multiple jet algorithms with different sensitivity to jet shape provides essential control over systematics in Pb+Pb jet measurements, especially as we do not know *a priori* the nature of the underlying event or the effects of jet quenching on the jet shape.

2.3.1 Seeded cone algorithm

The seeded cone algorithm operates on calorimeter towers. Towers are defined from energy sums of all the calorimeter layers within $\Delta\eta$x$\Delta\phi$=0.1x0.1. The towers within a given radius $R = \sqrt{\Delta\phi^2 + \Delta\eta^2}$ of the seed tower are clustered and iterated on until a convergence of the 4-vector of the jet is reached. For this algorithm, the underlying event background must be subtracted prior to reconstructing the jets. An η-dependent average cell energy, $\langle {E_T}^{\text{cell}} \rangle(\eta)$ is calculated for each layer of the electromagnetic and hadronic calorimeter. The $\langle {E_T}^{\text{cell}} \rangle(\eta)$ values are obtained excluding cells from high-E_T towers and the neighboring regions to prevent jets from biasing the background estimates. After the $\langle {E_T}^{\text{cell}} \rangle(\eta)$ values have been subtracted from all calorimeter cells, the resulting background-subtracted tower energies are input into the seeded cone algorithm to reconstruct jets. In this analysis, a cone of $R = 0.4$ and a seed tower energy threshold of 5 GeV are used. An example of the results of the background subtraction procedure is shown for a single event in Fig. 2.7.

The iterative cone jet algorithm will produce a candidate jet only when the transverse energy inside the cone is a local maximum in (η, ϕ). However, in the presence of heavy ion background, not all such maxima are true jets. Our studies of the behavior of the ATLAS seeded cone algorithm indicates that it is not particularly sensitive to fluctuations in the number of soft particles in the cone but is sensitive to hard or semi-hard particles in the underlying event, particularly correlated particles arising from mini-jets and charm or bottom hadrons. Figure 2.8 shows an example of such a jet compared to a real jet from PYTHIA. The "raw" candidate jets returned by a standard cone algorithm, therefore, need to be subjected to background discrimination before they can be accepted as true jets. The HIJING generator without quenching produces a large number of mini-jets and heavy quarks, thereby generating an underlying event for which correlated fluctuations are relatively common. Thus, it provides a valuable testing ground for procedures to reject fake jets.

The characteristics of the raw fake jets returned by the cone algorithm were studied using a separate sample of HIJING events generated without quenching but with a cut on the maximum p_T, $p_T < 10$ GeV/c, of outgoing partons in hard scattering processes. In this sample of events, all jets reconstructed above 10 GeV/c are in principle fake jets returned by the cone algorithm [1]. Several variables sensitive to the energy profile in the jet were evaluated. The most useful variable

[1] In reality, HIJING also produces jets and/or high-p_T hadrons from hard gluon radiation off a "soft" string. These are removed with cuts on the maximum hadron p_T for the fake jet analysis.

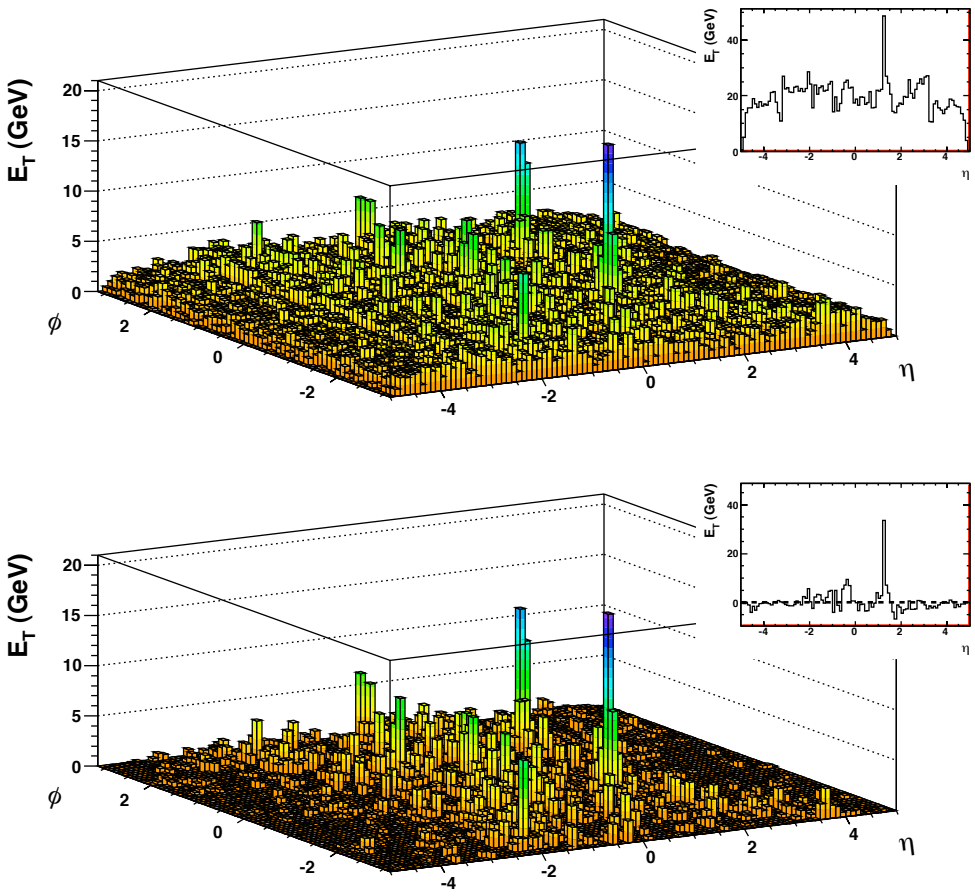

Figure 2.7: (top) Tower energies for a PYTHIA [100] di-jet event embedded into a HIJING event without quenching. (bottom) Tower energies in the same event after layer- and η-dependent subtraction of $\langle {E_T}^{\text{cell}} \rangle$ to remove the underlying event. The background- subtracted tower energies are then used as input to the seeded cone algorithm. The inset figures show the η-dependence of the energy in the towers integrated over $-0.5 < \phi < -1.5$ rad, which picks out the jet at $\phi \sim$-1 rad The large background from the underlying event is suppressed by the background subtraction.

for rejecting fake jets was found to be j_T^{Sum}, which is defined as

$$j_T^{\text{Sum}} = \sum_{cell} E_T^{cell} \sin R_{cell} \quad , \tag{2.2}$$

where $R_{cell} \equiv \sqrt{\Delta\phi^2 + \Delta\eta^2}$ is the jet cone angle between the cell and the jet axis. This variable assigns higher weights to cells with larger energy or cells at large angles from the jet axis. For real jets, j_T^{Sum} depends both on the jet energy and on the angular distribution of fragments in a jet, but in a non-trivial way due to the narrowing of the jet cone with increasing energy. For fake jets we find that j_T^{Sum} is roughly proportional to the E_T of the false jet. The dependence of the separation

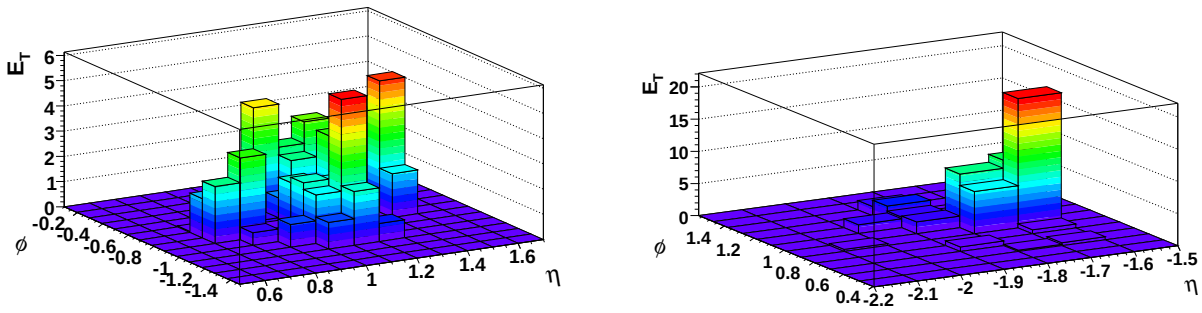

Figure 2.8: Demonstration of difference between false and true candidate jets returned by the iterative cone algorithm. (left) E_T distribution in $\Delta\eta \times \Delta\phi = 0.1 \times 0.1$ towers for a false jet resulting from nearby above-average E_T towers. (right) A similar distribution for a real jet (with an atypically asymmetric fragmentation).

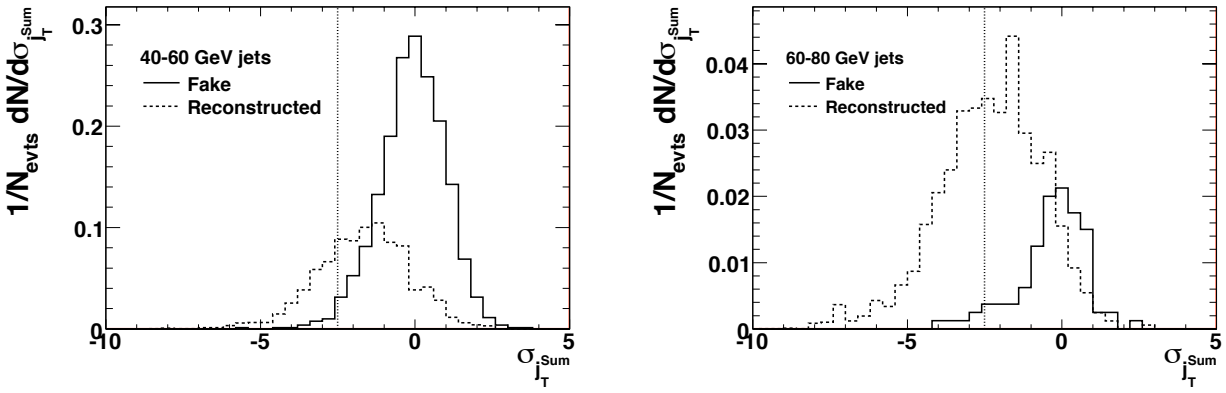

Figure 2.9: Comparison of the E_T-dependent $\sigma_{j_T^{\mathrm{Sum}}}$ cut (see Eq. 2.3) for two different jet energies 40-60 GeV (left) and 60-80 GeV (right). Jets with $\sigma_{j_T^{\mathrm{Sum}}} >$ -2.5 are removed.

between real and false jets on jet E_T is removed by making an E_T-dependent cut:

$$\sigma_{j_T^{\mathrm{Sum}}} = \frac{j_T^{\mathrm{Sum}}\left(E_T\right) - \langle j_T^{\mathrm{Sum}} \rangle \left(E_T\right)}{\sigma\left(E_T\right)}, \tag{2.3}$$

where $\langle j_T^{\mathrm{Sum}} \rangle \left(E_T\right)$ and $\sigma\left(E_T\right)$ are the E_T-dependent average value and width, respectively, for the *fake* jet j_T^{Sum} distribution. Figure 2.9 shows the distribution of $\sigma_{j_T^{\mathrm{Sum}}}$ for false (solid) jets and real (dashed) jets. The false jet distributions are centered at 0 and have widths of 1 as seen from Eq. 2.3. With increasing cone E_T energy the separation of the real and fake jets increases. A cut of $\sigma_{j_T^{\mathrm{Sum}}} > -2.5$ rejects most of the fake jets, but also produces an E_T-dependent efficiency loss that is particularly severe at low E_T. Such a cut can be tuned to optimize between the desired purity and efficiency and also on the characteristics of the background. We note that the actual Pb+Pb background is likely to have substantially lower level of correlated fluctuations than produced by HIJING without quenching. The background rejection technique described here can, then, be

used with a less restrictive cut on the discriminator variable and with a corresponding improved efficiency at low p_T.

2.3.2 k_T algorithm

The k_T algorithm [96, 97, 98] finds jets by recursively clustering towers until a cut-off criterion is reached. The extent of clustering can be controlled by a parameter, D, which was chosen to be $D = 0.4$ for the studies presented below. A particular advantage of this algorithm is that no fixed geometry (e.g. a cone) is imposed on the reconstructed jet. In the case of the Fast-k_T algorithm [99], the underlying event is handled in a completely different way from the cone algorithm. Following Cacciari and Salam [99], the jet reconstruction is performed directly on heavy ion events without background subtraction. In addition to real jets, the background towers are clustered into soft jets as shown in Fig. 2.10 for a HIJING [93] embedded PYTHIA[100] event. There are two jets from the embedded PYTHIA event which are clearly visible above the heavy ion background. The different shaded regions denote the jet candidates in this event (bottom left panel), most of them are jets primarily composed of background. The bottom right panel shows, for each jet, the ratio of maximum to average tower energy, E_T^{max}/E_T^{avg}, within the jet, plotted as function of the jet η. Clearly, this variable distinguishes between the PYTHIA jets and background jet candidates. It should be noted that this ratio for a jet with a Gaussian distribution in R is $1/\sigma$, where σ is the width of the energy profile in R. Therefore the background jets are much wider than the signal jets, as expected, and have lower values of E_T^{max}/E_T^{avg}. The η dependence of the ratio is parameterized as $r(\eta)$ and shown as the solid line in the lower right panel of Fig. 2.10. The difference between the actual E_T^{max}/E_T^{avg} and the parameterization is calculated for each jet candidate. This results in a difference distribution with a mean (μ) and a root-mean-square (RMS). A cut

$$(E_T^{max}/E_T^{avg} - r(\eta)) < \mu + 2 \times RMS$$

selects background jets. These jets are then used to estimate the underlying event background which is subsequently subtracted from the real jets.

2.4 Jet reconstruction performance

2.4.1 Method of evaluation

The performance of the seeded cone and k_T algorithms was evaluated through an extensive simulation study. In the simulation, a merged event is constructed by embedding a PYTHIA di-jet event into a simulated Pb+Pb HIJING event without quenching and without a hard scattering cut which would remove mini-jets. In heavy-ion collisions, the performance of the jet reconstruction algorithm is very sensitive to fluctuations in the underlying background. Thus mini-jets, heavy quarks, and other correlated sources produce many fake jets at low E_T. The HIJING events likely represent an upper limit of the event multiplicities (in $dN_{ch}/d\eta$) comparing to other models at the LHC (see Fig. 4.1). These simulations therefore represent a "worst case scenario" for the underlying background in Pb+Pb collisions.

Merging jets into background events occurs after each event is passed through a full GEANT simulation of the ATLAS detector. The merged events are then passed through the reconstruction chain and data analysis software. The resulting jets from the merged events are matched to the

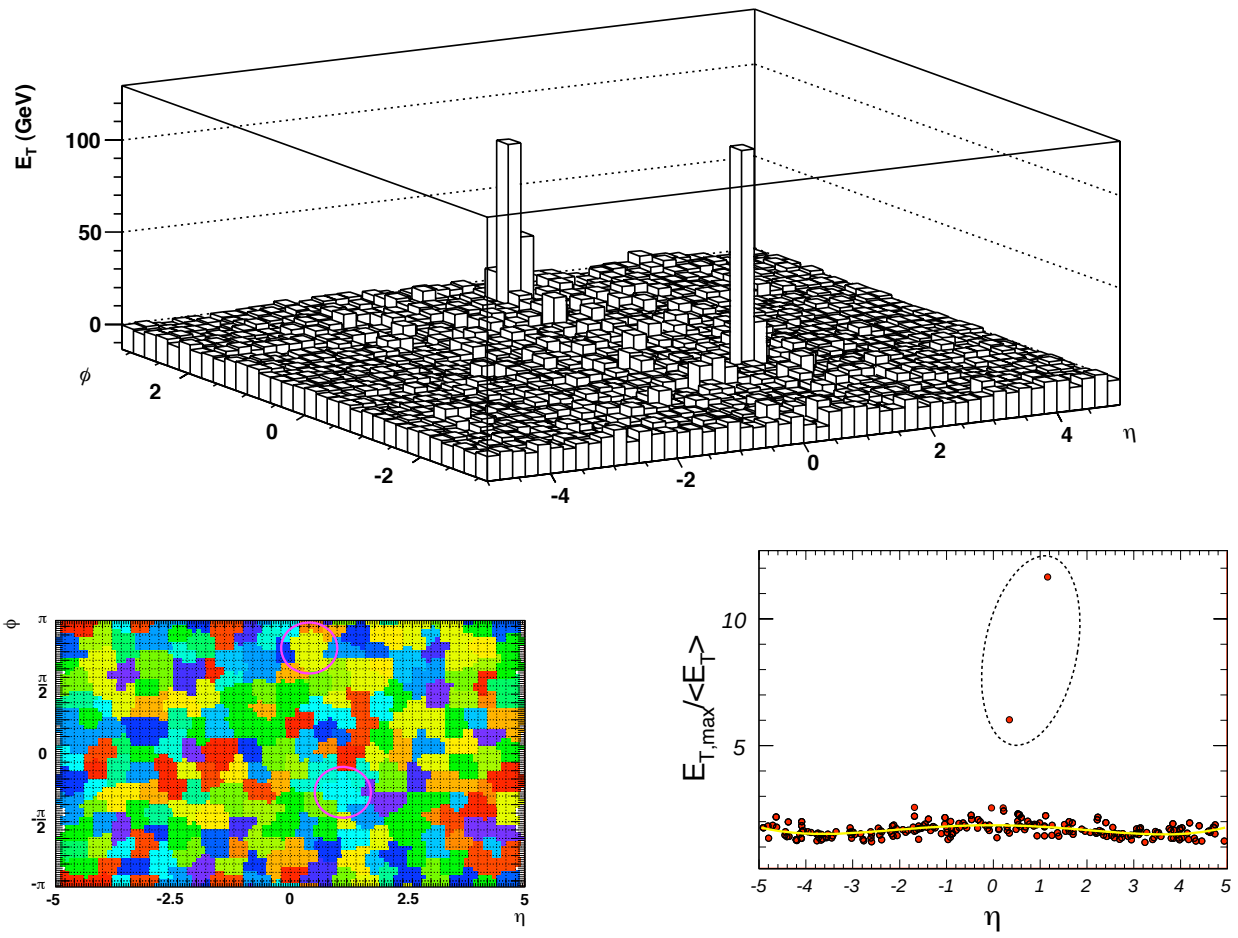

Figure 2.10: (top) Tower energies from a single PYTHIA di-jet event embedded in an event from unquenched HIJING with $dN_{ch}/d\eta = 2700$ at mid-rapidity and run with the Fast-k_T algorithm. (lower left) Each of the different, colored patches represent a jet defined by the algorithm. Every tower, even those with energy predominantly from the underlying event, is incorporated into a jet. (lower right) Distribution of maximum-to-average tower energy in reconstructed jets for this event. The two embedded PYTHIA jets (indicated by the circled points and areas) are distinguishable from the fake, background jets in this variable.

truth jets, which are defined as the jets found with the same jet algorithm with the PYTHIA final state particles as input. A match is found if the reconstructed jet and truth jets are close enough in angular space ($R = \sqrt{\Delta\phi^2 + \Delta\eta^2} < 0.5$). If multiple reconstructed jets are matched to the same truth jet, the jet with the smallest R is chosen to be the matched jet. In determining efficiencies and fake rates all reconstructed and truth jets are considered and not, for instance, only the highest energy jets in the event. The performance of each jet algorithm is evaluated based on a few key quantities: energy resolution, energy scale, efficiency and fake rate. These quantities are evaluated at the truth jet E_T, η, and ϕ unless otherwise specified.

b (fm)	$dN_{ch}/d\eta\|_{\|\eta\|<0.5}$
2	2700
4	2200
6	1700
8	1070
10	460

Table 2.1: Fixed impact parameter values used to produce HIJING events and their corresponding mid-rapidity ($|\eta|$ <0.5) charged particle multiplicity.

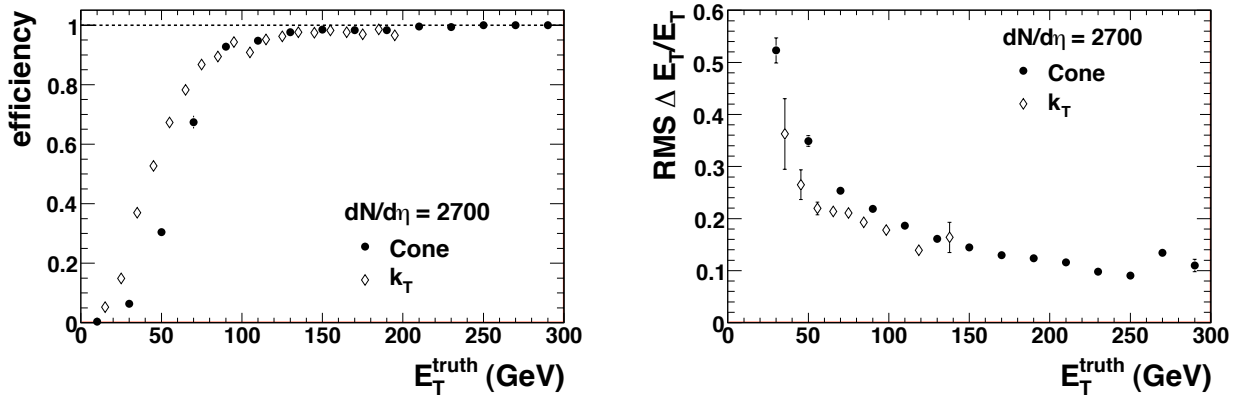

Figure 2.11: Comparison of efficiency (left) and E_T resolution (right) for the cone (closed) and k_T (open) algorithms for reconstructing jets in $dN_{ch}/d\eta = 2700$.

In order to evaluate the centrality dependence of performance quantities in this and other physics studies, HIJING events were generated at a set of fixed impact parameters. For these impact parameters, the mid-rapidity ($|\eta| < 0.5$) charged particle multiplicity ($dN_{ch}/d\eta$) was evaluated with the results shown in Table 2.1. When discussing the centrality dependence of jet reconstruction performance and other results in later chapters, we will quote $dN_{ch}/d\eta$ since such a quantity is, in principle, less subject to the assumptions of the HIJING model. We note, however, that the correlated semi-hard production in HIJING has a greater impact on jet performance than fluctuations in the soft background so different models for Pb+Pb events producing the same $dN_{ch}/d\eta$ will not necessarily give the same jet performance.

2.4.2 Performance results

Figure 2.11 shows the comparison of the jet performance for cone and k_T jets for the highest multiplicity environment simulated. The efficiency is shown in the left panel. While there are differences at low-E_T, primarily due to how the fake background is handled, the efficiencies converge to better than 95% at $E_T > 120$ GeV. The jet energy resolution is defined as the root-mean-square of the distribution of $\Delta E_T/E_T = \left(E_T^{truth} - E_T^{reco}\right)/E_T^{truth}$. A better resolution for the k_T algorithm is observed.

The jet performance results have been studied as a function of background multiplicity. Figure 2.12 shows the jet reconstruction efficiency for seeded cone jets as a function of E_T^{truth} and as a

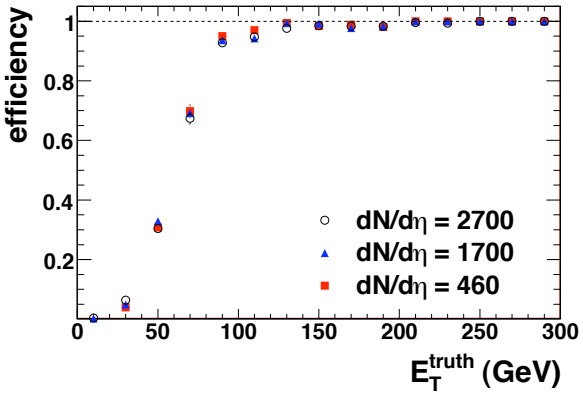

Figure 2.12: Jet reconstruction efficiency for jets reconstructed with the seeded cone and k_T algorithms as a function of input jet E_T and as a function of HIJING Pb+Pb multiplicity.

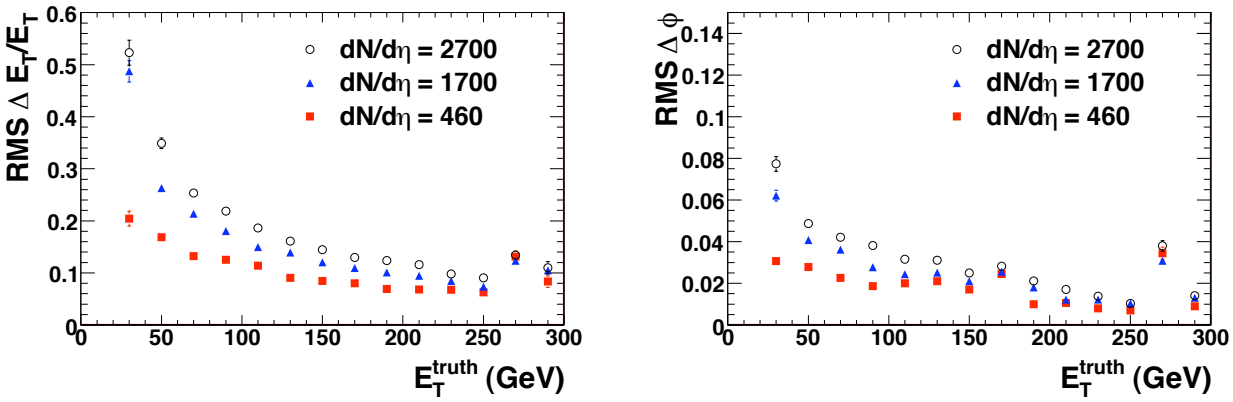

Figure 2.13: (left) Jet energy resolution as function of truth jet E_T for three multiplicity bins for seeded cone jet algorithm. (right) The azimuthal angular resolution of the seeded cone jets as function of truth jet energy.

function of HIJING multiplicity. There is little to no dependence of the efficiency on multiplicity. This result is a combination of two effects. First, the shape of the efficiency curve is most influenced by the 5 GeV tower E_T seed cut in cone algorithm. A lower seed cut would result in higher efficiency at lower jet E_T but would generate more background jets. Second, for the results presented in Fig. 2.12 the same background rejection cuts have been applied for all centralities. For actual data analysis, the cuts would depend on centrality becoming less severe for more peripheral collisions. Thus, the results in Fig. 2.12 represent worst-case results for non-central collisions.

Figure 2.13 shows the energy and position (in ϕ) resolution as a function of truth jet E_T for cone jets for several Pb+Pb multiplicity bins. Both energy and position resolution of cone jets improve with increasing jet energy and for lower multiplicity environments. Although not shown, the position resolution in η is comparable to that in ϕ for all multiplicities. We note that many physics models predict that $dN_{ch}/d\eta$ for the most central Pb+Pb events is closer to $dN_{ch}/d\eta = 1700$ than 2700 (see Fig. 4.1), for which case we should expect a significant improvement of the resolution in the real data.

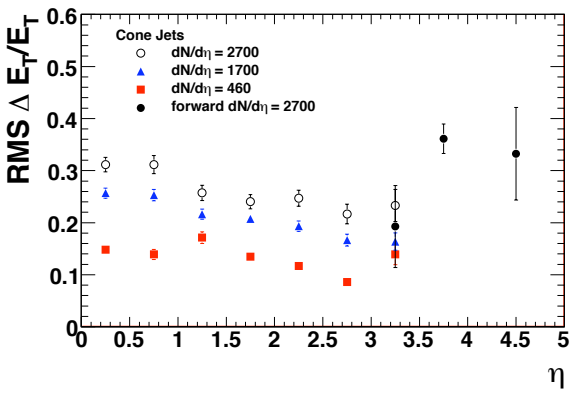

Figure 2.14: Jet energy resolution for $E_T > 50$ GeV seeded cone jets as a function of η for HIJING Pb+Pb events of different centrality, $dN_{ch}/d\eta|_{\eta=0}$.

The pseudo-rapidity dependence of the jet performance has also been evaluated. Figure 2.14 shows the jet energy resolution for seeded cone jets with $E_T^{truth} > 50$ GeV and for three different multiplicity bins. The points with $|\eta| < 3.2$ are obtained from jets reconstructed in the barrel and the end-cap calorimeters while the open points with $|\eta| > 3.2$ are from jets reconstructed in the forward calorimeters, an analysis which has only been carried out for the most central Pb+Pb sample. The improvement in energy resolution as η increases in the barrel and end-cap regions is due to the decrease in the underlying HIJING background. In the most forward rapidity region, the energy resolution deteriorates due to larger segmentation of the forward calorimeters. However, due to a lower underlying background, the resolution is comparable to that for mid-rapidity. In summary, over the entire η coverage of the calorimeter, 20-30% jet E_T resolution is obtained in the highest occupancy environment.

Figure 2.14 compares the reconstructed cone jet spectrum with the input and fake jet spectra. Even without correcting for efficiency and energy resolution, the reconstructed spectrum already matches the input spectrum above 80 GeV quite well. The fake jet spectra before and after the rejection cuts are shown by the dashed line and squares, respectively. These rates fall much faster than the input jet spectrum given by PYTHIA. The impact of these performance results on physics results can be seen in Fig. 2.15 which shows the ratio of reconstructed and input jet spectra without correction. Above 80 GeV the required corrections are of order 20%, much smaller than the factor of two jet suppression predicted by Lokhtin (see Fig. 2.6). We note, for completeness, that no adjustment of the jet energy scale after background subtraction has been applied. Distortions of the jet energy scale due to the background subtraction are included in Fig. 2.15. Based on these results, we expect the systematic errors in the measurement of the jet spectrum to be sufficiently controlled that the spectrum can provide direct sensitivity to collisional energy loss and large-angle radiative energy loss.

A summary of important performance variables, jet reconstruction efficiency, fake rate, and E_T resolution, are listed in Table 2.2 for 70 GeV reconstructed seeded cone jets in three multiplicity bins.

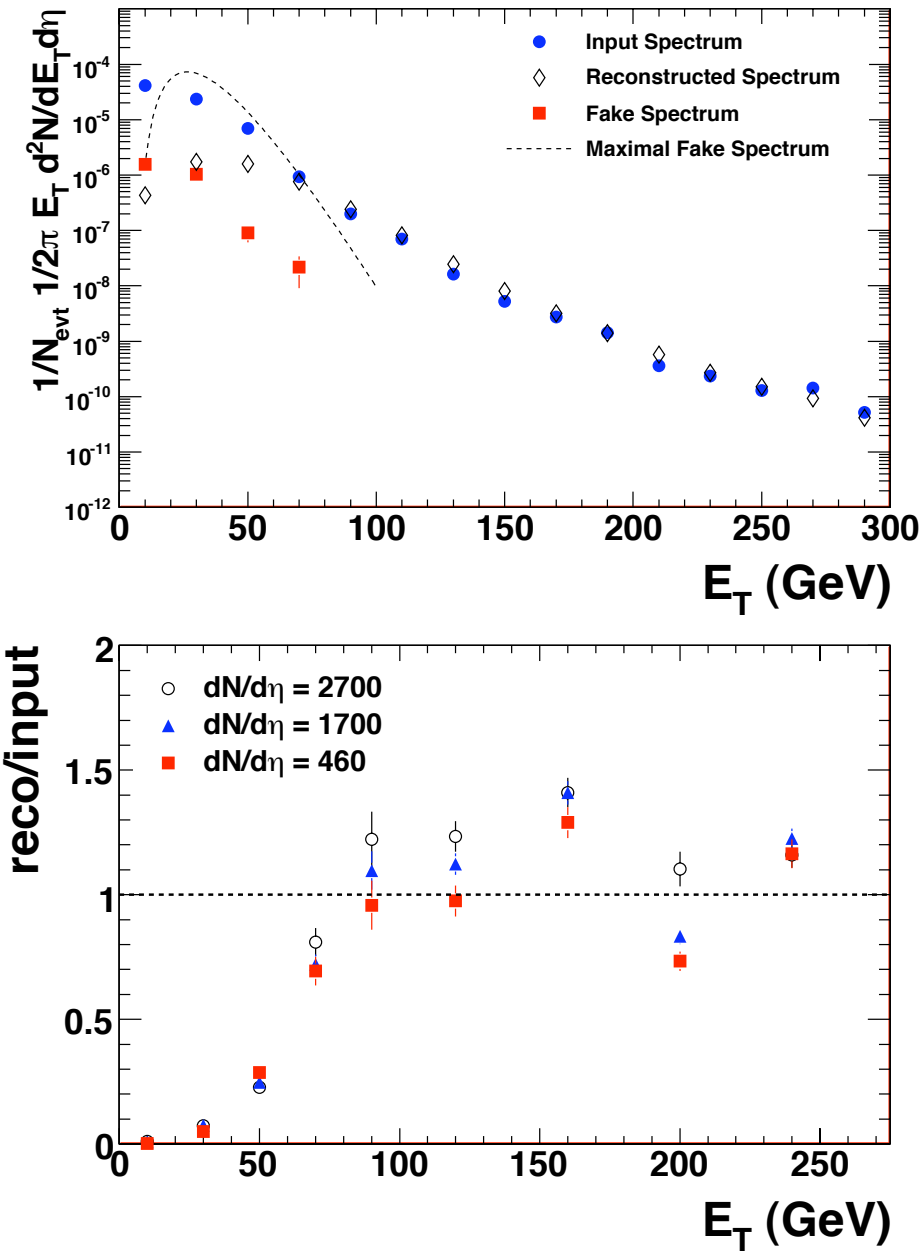

Figure 2.15: (top) Input (filled circles), raw reconstructed (diamonds), and fake (squares) spectra for cone jets in central ($dN_{ch}/d\eta = 2700$) Pb+Pb collisions. The reconstructed spectrum is not corrected for efficiency or energy resolution. The dashed line represents the absolute fake jet rate from pure HIJING events prior to background jet rejection (see text for details). (bottom) Ratio of reconstructed to input jet spectrum for three different Pb+Pb collision centralities without efficiency and resolution corrections to the reconstructed spectra.

$dN_{ch}/d\eta\|_{\eta=0}$	efficiency	B/(S+B)	$\sigma_{\Delta E_T/E_T}$
2700	70%	3%	25%
1700	70%	1%	21%
460	70%	$\ll$1%	15%

Table 2.2: Relevant jet reconstruction quantities for 70 GeV seeded cone jets reconstructed in different $dN_{ch}/d\eta$ backgrounds: efficiency, fake fraction, and jet energy resolution.

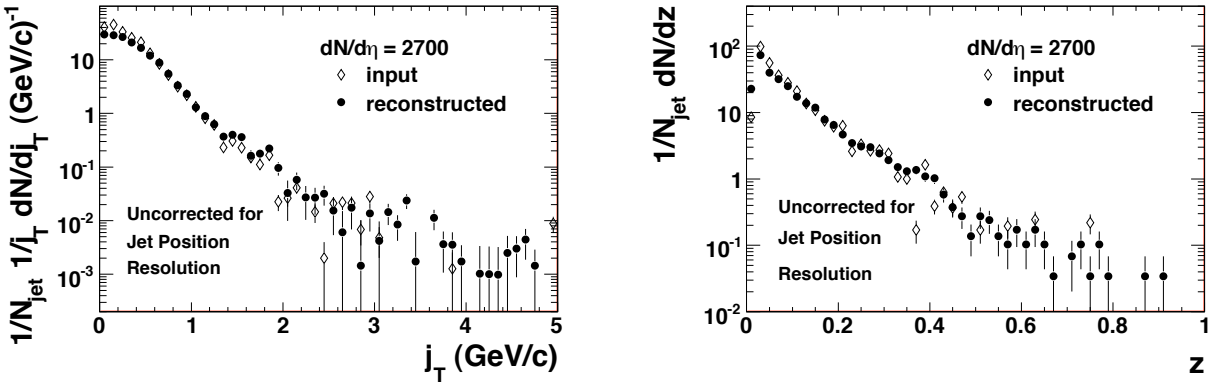

Figure 2.16: (left) Input (open) and reconstructed (closed) j_T distribution (see Eq. 2.4). (right) Input (open) and reconstructed (closed) fragmentation functions (see Eq. 2.5). The reconstructed quantities are uncorrected for position and energy resolution, which accounts for any difference with the input distributions.

2.5 Jet Fragmentation

Full jet reconstruction provides new variables, sensitive to in-medium energy loss, that are currently not available at RHIC. The first of these is the transverse momentum of fragments with respect to the jet axis, j_T,

$$\begin{aligned} j_T &= |\hat{p}_{jet} \times \vec{p}_{frag}| \\ &\approx p_{T,frag} \sin R \quad , \end{aligned} \tag{2.4}$$

where $\hat{p}_{jet}$ is the jet direction, $\vec{p}_{frag}$ is the three momentum vector of the fragment, $p_{T,frag}$ is the particle transverse momentum with respect to the beam, and $R = \sqrt{\Delta\phi^2 + \Delta\eta^2}$ is the jet cone variable. The j_T distribution has a soft core governed by non-perturbative physics and a power law tail resulting from hard radiation of the parton shower. Jet in-medium energy loss is expected to modify the distribution of hard fragments associated with the jet and can be detected as a modification of the j_T distribution [65].

Another observable of interest is the modification of the jet fragmentation function. The frag-

mentation variable, z, is the longitudinal fraction of the jet momentum carried by the fragment,

$$\begin{aligned} z &= \frac{\hat{p}_{jet} \cdot \vec{p}_{frag}}{|\vec{p}_{jet}|} \\ &\approx p_{T,frag} / E_{T,jet} \cos R. \end{aligned} \tag{2.5}$$

The interaction of the jet with the medium is expected to soften the fragmentation function by reducing the number of fragments at large z and increasing the number of fragments at small z (see Ref. [92] for a recent analysis).

The reconstructed fragmentation function, $D(z)$, and the j_T distribution are obtained using charged tracks with $p_T > 2$ GeV/c reconstructed from the silicon detectors (Pixel and SCT) in the ATLAS Inner Detector (see Chapter 4 for more details on tracking performance). The tracks are required to match to hits in the calorimeter taking into account the bending due to the magnetic field. The measured j_T distribution and fragmentation function are shown in Fig. 2.16 for the highest multiplicity Pb+Pb events considered. These distributions have been corrected for a an approximately constant tracking reconstruction efficiency of 70% (as shown in Fig. 4.10), they are not corrected for the position and energy resolution of the reconstructed jets. These distributions are also compared with the distributions for final state truth charged particles within an $R = 0.4$ cone around the truth jet axis. Since no medium modifications are simulated, the truth and reconstructed distributions should be essentially the same, as is indeed observed. Small differences between the truth and reconstructed distributions are entirely attributed to the jet position and energy resolution.

2.6 Di-jet correlations

The large η acceptance of the ATLAS calorimeter system provides nearly complete acceptance for di-jets making possible a variety of correlation measurements. Jets traversing the medium are also expected to multiple scatter as a consequence of energy loss [69]. Therefore, angular correlations between the back-to-back di-jets should be broadened in central Pb+Pb collisions relative to p+p collisions [64]. The left panel of Fig. 2.17 shows the conditional yield of detecting a second, associated jet (B) given a leading jet (A) as a function of their relative azimuth, $|\Delta\phi|$ in central Pb+Pb collisions. The seeded cone jet reconstruction algorithms are used and no efficiency and energy resolution corrections were applied. The distributions show a clear peak at $|\Delta\phi| = \pi$, indicating the back-to-back emission of di-jets, and very little background at other $|\Delta\phi|$. Integrating the distribution gives a 60% probability for detecting a jet with $E_T > 70$ GeV that is associated with a leading jet with $E_T > 100$ GeV. This high coincidence rate is due to the large detector acceptance and accurate measurements for single jets. A more sensitive probe of multiple scattering might be the p_{out} distribution which measures the momentum acoplanarity of the associated jet compared to the leading jet. The variable p_{out} is defined as

$$p_{out} = E_T^B \sin R. \tag{2.6}$$

and its distribution is shown in the right panel of Fig. 2.17.

At RHIC, the studies of the medium response to jet energy loss are important tools to understand properties of the produced medium. In principle, such studies can also be explored with

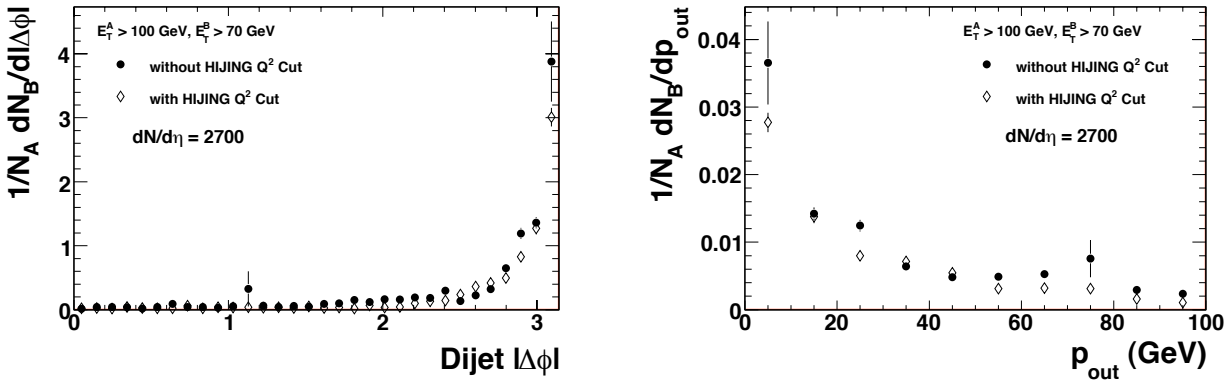

Figure 2.17: Conditional yield for finding an associated jet above 70 GeV (B) given a leading jet above 100 GeV (A), plotted as a function of (left) di-jet $|\Delta\phi|$ and (right) p_{out} (see Eqn. 2.6).

ATLAS. However, ATLAS's abilities for measuring medium response are difficult to quantify as there is no consensus on the mechanism of medium response, and thus no model implementations of this effect exist that could be used to generate LHC events. Still, if a ridge exists and is associated with a high-E_T jet and extends to ± 4 units in $\Delta\eta$, the ATLAS calorimeter, covering $|\eta| < 5$, will certainly encompass the entire ridge. Furthermore, a possible Mach cone and ridge associated with di-jets can be studied on an event-by-event basis as opposed to statistically averaging over many events as has been done at RHIC. These are some of the physics capabilities that will be explored in the near future.

2.7 Heavy quark jet reconstruction

To understand heavy quark energy loss, it will be important to identify bottom and charm jets. Fortunately, the excellent jet reconstruction capability of the ATLAS detector and excellent capabilities for tagging heavy quark mesons and associated semi-leptonic decay muons make the direct study of the heavy-quark energy loss feasible. Once the high energy jets are reconstructed, two tagging methods to can be applied to identify the flavor of the reconstructed jets: 1) tagging charm and bottom mesons directly via their displaced decay vertices and associating these heavy mesons to reconstructed jets; 2) associating semi-leptonic decay muons directly to reconstructed jets. A first attempt of the latter approach is described in this section.

To leading order in QCD, most of the muon-tagged jets come from hard-scattering processes that lead to di-jet events. The reconstructed jet and muon could either belong to the same truth jet, or they belong to different jets of the di-jet. Due to the weak decay of light hadrons in flight, a portion of the muons may not be associated with heavy quark jets. In addition, only a fraction of the heavy quark jets contribute to high p_T muons via the semi-leptonic decay of heavy quark mesons. Based on these considerations, the performance of muon tagging for heavy quark jets has been quantified by the two most important parameters. The first parameter is the purity of heavy quark jets in the the tagged jet sample, and the second parameter is the tagging efficiency for jets that are known to come from heavy quarks.

To estimate the purity of heavy quark jets in the tagged jet sample, PYTHIA minimum bias

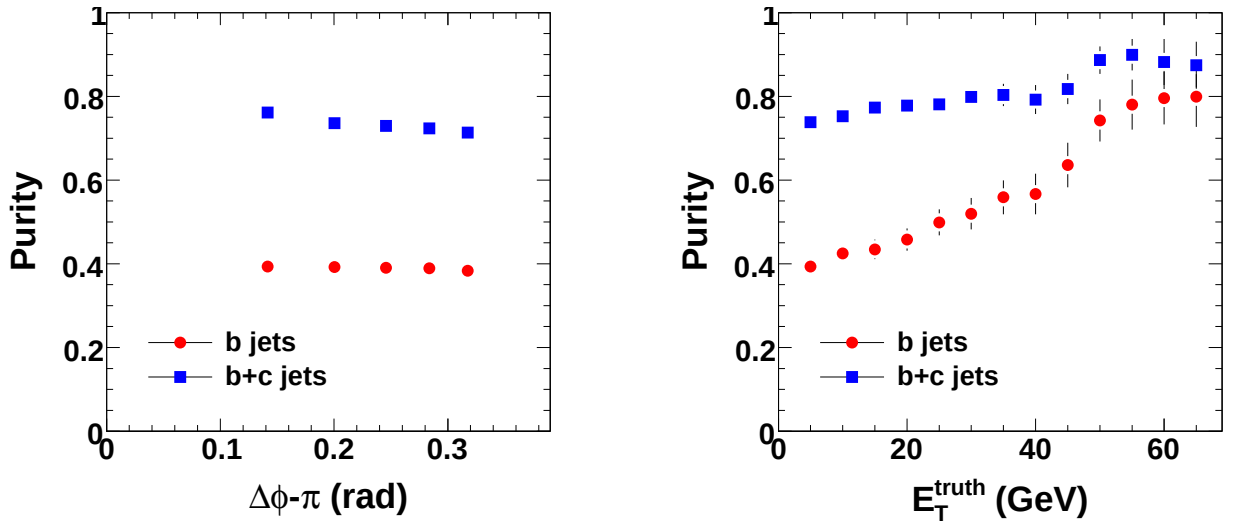

Figure 2.18: Bottom jet (red circles) and heavy flavor (blue squares) tagging purity as a function of azimuthal angle difference between the tagged jet and muon at the away-side ($\Delta\phi \sim \pi$) requiring a muon with $p_T > 5$ GeV (left) and as a function of truth muon E_T (right).

events were generated with the requirement that each event contain at least one muon with $p_T > 5$ GeV/c and one jet with $E_T > 35$ GeV. The resulting events were then embedded into central HIJING Pb+Pb events ($dN_{ch}/d\eta = 2700$ at mid-rapidity) generated as described in Section 2.4.1. The jets were reconstructed with the seeded cone jet algorithm as described in the Section 2.3.1. Single muon candidates were reconstructed using the standard tracking and muon identification software in ATLAS [101]. Details of the muon reconstruction are given in Chapter 5.

The purity of heavy quark jets in the tagged jet sample is defined as the ratio between the number of jets of interest, *i.e.* those from heavy quarks, and the total number of jets. To identify the heavy quark jets, the jets reconstructed from the merged event are first matched to the truth jets, which are obtained by applying the seeded cone algorithm to the final state particles in the input PYTHIA event. The matching criteria requires the three-dimensional opening angle between the reconstructed jet and truth jet, θ, to satisfy $\theta < 0.2$ rad. Input (truth) jets are tagged as bottom jets by tracing the PYTHIA ancestry information back to the original string. If it is a bottom string and the truth jet in question has more than 50% of the bottom quark energy, the truth jet is considered to be a bottom jet. Otherwise, the truth jet, and hence the matched reconstructed jet, is either a charm jet or light quark jet.

The purities of the muon-tagged jets are shown in the left panel of Fig. 2.18 as a function of the azimuthal angle difference between the muon and tagged jet. The red circles show the bottom-tagged purity; about 40% of the tagged jets come from bottom quarks. The blue squares show the heavy flavor-tagged purity is about 70%. This suggests 30% of the tagged jets come from charm quarks and remaining 30% of the tagged jets come from light quarks and gluons. To summarize, the jets tagged by muon $p_T > 5$ GeV contains approximately equal number of bottom, charm and light quark/gluon jets.

The purity of heavy quark jets in the tagged jet sample also depends strongly on the trigger muon p_T. This is shown on the right panel of Fig. 2.18. The red circles are bottom-tagged pu-

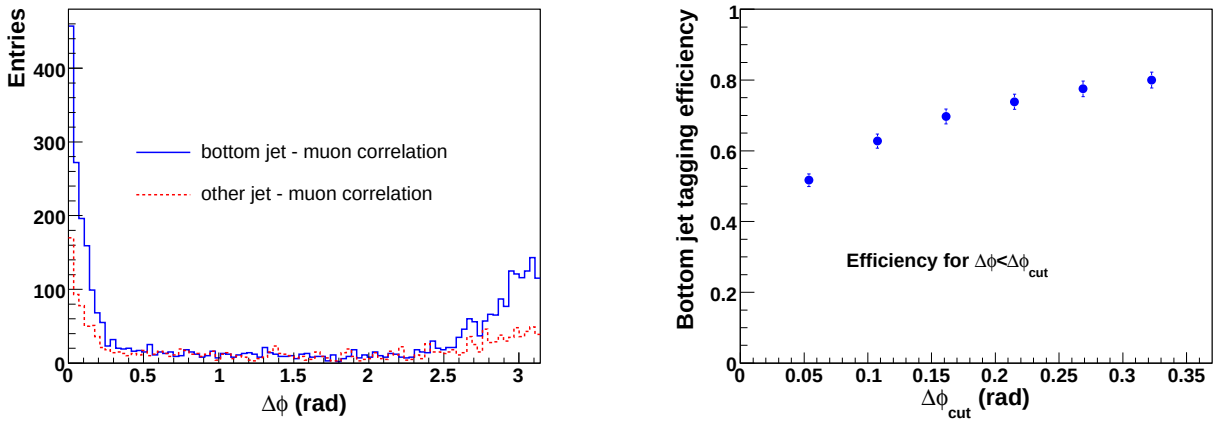

Figure 2.19: (left) Azimuthal correlation between the reconstructed jets and the muons. The solid line and dashed line are for tagged bottom jets and other jets, respectively (right) Jet tagging efficiency as a function of angular cuts ($\Delta\phi < \Delta\phi_{cut}$).

rity and the blue squares show the heavy flavor-tagged purity. For muons at $p_T \gtrsim 60$ GeV/c, approximately 80% of all tagged jets are bottom-jets.

Further improvement is possible if we consider the correlation between muon p_T and jet E_T. Since heavy quark jets have much harder fragmentation functions, *i.e.* the leading heavy meson contributing to the muon carries most of the energy of the jets, the muon p_T and jet p_T should be much closer to each other than for muons from light hadron decays. Thus a high E_T jet correlated with a low p_T muon mostly likely indicates a gluon jet or light quark jet.

The minimum bias PYTHIA events used for the purity study contain a limited number of bottom jets. For an accurate estimation of the tagging efficiency for bottom jets at ATLAS, a separate set of PYTHIA events containing bottom jets was generated, requiring at least one muon with $p_T > 5$ GeV/c, and at least one jet with $E_T > 35$ GeV. These events were embedded into central ($dN_{ch}/d\eta = 2700$) HIJING Pb+Pb events, and analyzed using the same procedure applied to minimum-bias PYTHIA events. The same procedures for matching the reconstructed jets with truth bottom jets are carried out. Figure 2.19 shows the azimuthal correlation between reconstructed jets ($E_T > 35$ GeV) and muons ($p_T > 5$ GeV/c) for the bottom (blue) and non-bottom (red) jet samples. The muons either come directly from the tagged bottom jet themselves (peak around $\Delta\phi \sim 0$, or they corresponds to muons from a bottom jet recoiling from another bottom jet (peak around $\Delta\phi \sim \pi$). For the non-bottom jet sample, fewer jets are measured, however a correlation with muons is still observed.

The narrow azimuthal correlation between the tagged jets and the muon can be used to improve the purity of the bottom jets by making a matching cut in $\Delta\phi$. The tagging efficiency is defined as the probability for a bottom jet to be within the matching cut. The efficiency for tagging the bottom jet back-to-back to the muon is shown in Fig. 2.19. A cut of 0.16 rad gives a 70% tagging efficiency while relaxing the cut to 0.32 rad gives an efficiency of 80%.

Using high-p_T muons to tag heavy flavor jets will be an important tool in studying the heavy flavor energy loss. A clear correlation in muon-jet $\Delta\phi$ is observed from heavy flavor jets. By cutting on this muon-jet $\Delta\phi$ and the muon p_T it is possible to tune the purity of the heavy flavor sample and the tagging efficiency.

2.8 Summary

- Utilizing the large acceptance, finely-segmented ATLAS calorimeter, jets in a heavy ion environment can be measured with high efficiency and excellent position/energy resolution over a broad range in energy ($E_T > 40$ GeV), pseudo-rapidity (± 5) and multiplicities (at least up to $dN_{ch}/d\eta = 2700$). These unprecedented reconstruction capabilities for full jets will significantly reduce the energy-loss biases intrinsic in leading hadron and di-hadron correlation analyses at RHIC.

- The full jet and di-jet measurements possible with the ATLAS detector will provide direct constraints on the mechanisms for energy loss and jet-medium interactions. In particular, the jet fragmentation (via $D(z)$) and the jet shape (via the j_T distribution and di-jet $\Delta\phi$ and p_{out}) can be reliably quantified. These measurements are sensitive to jet energy loss and medium response.

- Combining the jet reconstruction with the muon identification capability of the ATLAS detector allows the study of heavy quark energy loss, which will be of particular use to quantify the role of radiative and collisional energy loss.

- Full jet reconstruction combined with the direct photon capability of the ATLAS calorimeter (described in detail in the next chapter) provides a means to probe the properties of the medium using γ-jet correlations.

- All of the measurables described here will be studied as a function of global variables, such as centrality and the angle with respect to the reaction plane.

- In tandem, these techniques will allow ATLAS to undertake a comprehensive program of tomographic studies of the energy loss and the properties of the medium.

Chapter 3

Photons and γ-jet correlations

This chapter describes the physics need for direct photon and γ-jet measurements with ATLAS, the techniques available in ATLAS for photon detection, and its capabilities for photon physics and γ-jet correlations, both with and without isolation. The ability to efficiently separate photons and neutral hadrons without an isolation cut over a broad acceptance is a unique strength of ATLAS. In addition to providing an optimal window on jet energy loss, this particular aspect of the analysis provides the unique capability to measure non-isolated photons from fragmentation or from the medium.

3.1 Physics motivation

Direct photons are a useful tool, complementary to jet and di-jets, for "tomographic" studies of the microscopic properties of the sQGP. They can be studied either inclusively, or in coincidence with jets (known as "γ-jet" events). γ-jet events are a particularly useful probe because the medium is transparent to photons. Therefore the γ's can be used to measure the original energy and direction of the away-side jets, which should be strongly modified by the medium. They not only provide a model independent way for calibrating the jet reconstruction algorithms (e.g. energy scale and resolution), but also help to extend the jet reconstruction to lower E_T where the jet reconstruction efficiency degrades (as shown in Fig. 2.12). This measurement should be able to eliminate the trigger bias intrinsic to the jet-jet coincidence measurements where there is no absolute calibration of jet energy (since both jets being modified by the medium). Thus, the study of γ-jet events provides direct access to the average behavior as well as fluctuations of the energy loss process.

"Direct" photons refer to those photonss that are produced during the initial creation and space-time evolution of the fireball, which should be distinguished from "decay" photons from the electromagnetic decays of hadrons. To leading order in pQCD, most direct photons come from γ-jets events generated by the initial hard-scattering processes such as QCD Compton scattering ($qg \to \gamma q$) and annihilation ($q\bar{q} \to \gamma g$) processes, and these photons are called "prompt" photons. The main difficulty facing the γ-jet analysis is the relatively small production rate. The cross-section of γ-jet events, compared to jet-jet events, is typically down by a factor of 100–1000 for E_T below 200 GeV at LHC energies. The background photons from various decay modes, such as $\pi^0, \eta \to \gamma\gamma$, create a large background to the direct photon sample. Figure 3.1 shows the direct γ to $(\pi^0 + \eta)$ ratio as function of transverse energy estimated from a next-to-leading order (NLO)

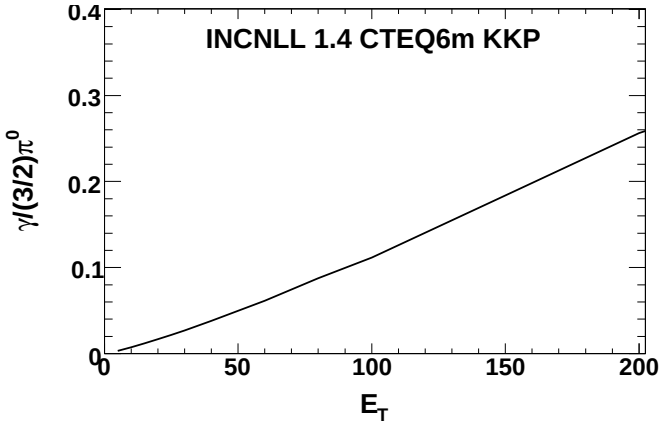

Figure 3.1: Next to leading order calculation of the direct γ to neutral hadron ratio as function of transverse energy. The η yield is estimated to be 50% of that for π^0.

calculation [102], which is around 0.1 for E_T of 100 GeV.

The main challenge for the γ-jet analysis is to derive an algorithm which can effectively reject the decay photons while maintaining a reasonable fraction of direct photons. In this section, the performance of ATLAS detectors for single γ and for γ-jet measurements is evaluated. Two methods are described to reject decay photons. In the first, a shower shape cut based on the highly segmented first layer of the calorimeters provides a factor of 3–5 rejection. An additional factor of 10 rejection can then be achieved by a set of isolation criteria. The largest rejection power is then obtained by combining the shower shape and isolation cuts, which are largely orthogonal to each other. Future prospects and comparisons to ALICE and CMS are discussed in the end.

3.2 Photon identification

The design of the ATLAS electromagnetic calorimeter is optimal for direct photon identification. The first layer of the electromagnetic calorimeter, which covers the full azimuth and $|\eta| < 2.4$, has very fine segmentation along the η direction (ranging from 0.003–0.006 units). This layer provides detailed information on the shower shape, which allows a direct separation of photons, π^0, and η on a particle-by-particle level. Deposited energy distributions for a typical single γ, single $\pi^{0'}$ and single η meson are shown in the upper panels of Fig. 3.2. Characteristically different shower profiles are seen. The energy of a single photon is concentrated across a few (typically 3) strips, with a single maximum in the center, while the showers for $\pi^0 \to \gamma\gamma$ and $\eta \to \gamma\gamma$ are distributed across more strips, often with two or more peaks. The broad shower profile for π^0 and η reflects the overlap of showers for two or more decay photons, which are typically separated only by a few strips. The strip size of 0.003 units roughly corresponds to the minimum opening angle between two decay photons for a 50 GeV π^0. The opening angle for an η meson with the same energy is about 4 times bigger. Even when the two peaks are not resolved, the multi-photon showers are measurably broader on a statistical basis. Thus the strip layer allows the rejection of π^0 and η decay photons over a very broad energy range.

In Pb+Pb collisions, the shower profiles at the strip layer can be distorted by the high occu-

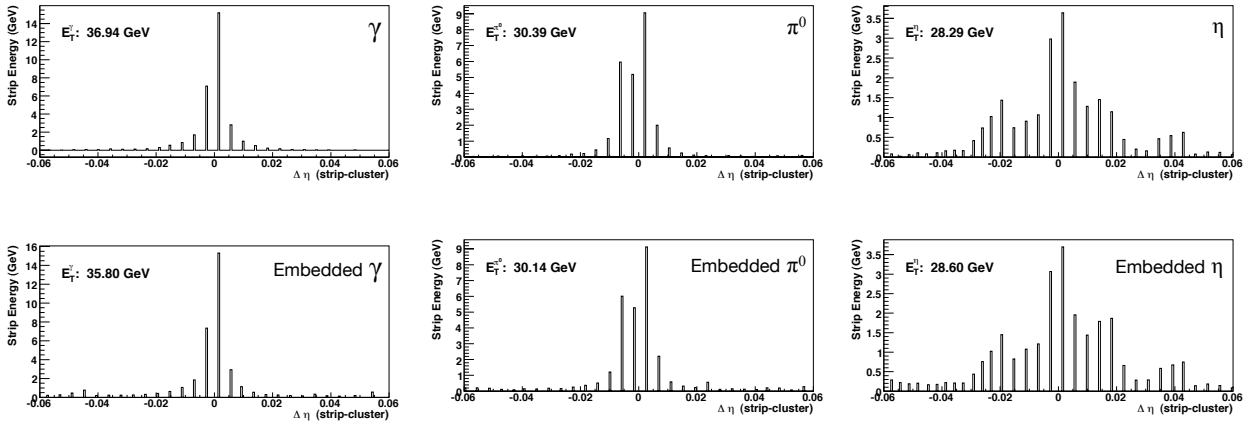

Figure 3.2: The energy deposition in the strip layers around the direction of (upper left) a single photon, (upper middle) a single π^0 and (upper right) a single η as well as for (lower panels) the identical particles embedded in one central ($b = 2$ fm) Pb+Pb event. The energy values are the reconstructed energies.

pancy environment. To study such occupancy effects, single photons, π^0's and η's have been embedded in Pb+Pb events generated with HIJING. The official ATLAS detector simulation, digitization and data analysis procedures have been used to simulate and analyze the merged events and to reconstruct the embedded jet and photon. The lower panels of Fig. 3.2 show the strip layer energy distributions surrounding the direction of single particles embedded in central Pb+Pb events. The γ, π^0 and η in these panels are the same ones used in the upper panels. Despite the huge number of low-energy particles produced in Pb+Pb events, the underlying background only introduces, on average, a few hundred MeV background for each strip. In comparison, a single photon typically deposits 40-50% of its total energy in the strip layer. Thus the energy deposited in each strip by a high energy single γ, π^0 and η is typically several GeV. In this case, the shower shape for the embedded particle is almost unchanged by the background. One expects the rejection to work down to very low energy (about 10 GeV), and the performance for the background rejection and identification efficiency should not depend strongly on the event centrality.

To distinguish direct photons from neutral hadrons, a set of cuts has been developed based on the shower shape in the strip layer. These cuts reject those showers that are anomalously wide or exhibit a double peak around the maximum. In total, six variables are used to define the cuts, the most important being:

- Fracs1: the fraction of energy in 8 strips around the core of 6 strips, i.e $(E(\pm 7) - E(\pm 3))/E(\pm 7)$.
- E2diff: energy of second peak minus the minimum energy between the two peaks.

The cuts on these variables have been tuned as function of photon energy and pseudo-rapidity. In general, better rejection can be achieved using a tighter cut, but at the expense of reduced efficiencies. The performance has been quantified via photon efficiency (ϵ_γ) and relative rejection ($R_{\rm rel}$). The former is defined as the fraction of photons passing the cuts. The latter is defined

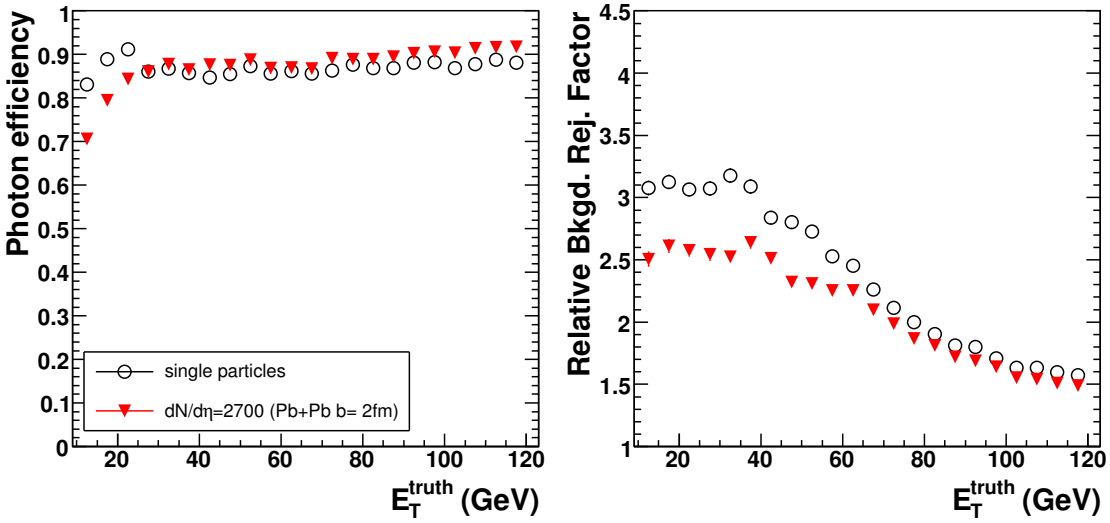

Figure 3.3: (left) Photon identification efficiency and (right) relative rejection factor for neutral hadrons for the loose cut set for p+p (open circles) and central ($b = 2$ fm, $dN/d\eta = 2700$) Pb+Pb collisions (filled triangles). These are averaged over the entire range $|\eta| < 2.4$

simply as the ratio of the efficiencies for γ and neutral hadrons,

$$R_{\rm rel} = \frac{\epsilon_\gamma}{\epsilon_{\pi^0 \text{ or } \eta}} \tag{3.1}$$

The relative rejection basically reflects the gain on the signal (direct photon yield) relative to background (neutral hadron yield). The absolute rejection can also be used, which is defined as

$$R_{\rm abs} = \frac{1}{\epsilon_{\pi^0 \text{ or } \eta}} \tag{3.2}$$

thus $R_{\rm abs} \approx R_{\rm rel}$ if the efficiency for direct photons is close to one.

In this analysis, two sets of cuts have been developed, a "loose" cut set and a "tight" cut set. The performance for these two sets is summarized in Fig. 3.3 for the loose cuts and in Fig. 3.4 for the tight cuts. The variations from point to point are not due to statistical fluctuations, which typically are smaller than the symbol size, but are caused by the fact that the cuts are currently tuned by hand bin-by-bin in E_T. The loose cuts give a factor of 1.5–3 relative rejection with a photon efficiency of about 90%; the tight cuts give a factor of 3–5 relative rejection with an efficiency of about 50%. The efficiency is almost independent of E_T, η, and centrality, by construction. The corresponding rejection factors vary weakly with the E_T, η, and centrality. The η dependence (not shown) is roughly $\pm 25\%$ relative to the η-averaged value with the best performance near midrapidity. The E_T and centrality dependence are shown, with the 30–50 GeV clusters in p+p having the best performance.

The identified photons are well reconstructed, even in heavy ion collisions. Figure 3.5 shows the absolute spatial resolution in ϕ and η averaged over the entire acceptance as a function of E_T. The resolution is shown for single photons (labeled as $dN/d\eta = 0$) and for photons embedded

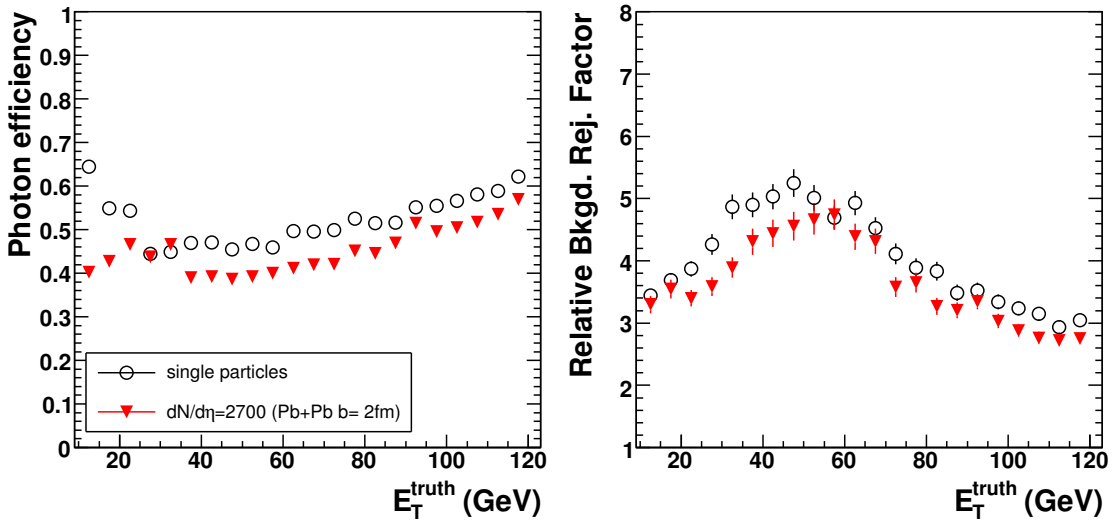

Figure 3.4: (left) Photon identification efficiency and (right) relative rejection factor for neutral hadrons for the tight cut set for p+p (open circles) and central ($b = 2$ fm, $dN/d\eta = 2700$) Pb+Pb collisions (filled triangles). These are averaged over the entire range $|\eta| < 2.4$.

in Pb+Pb collisions for three different centralities, indicated by their midrapidity particle densities. For E_T around 100 GeV, the η resolution is about 0.0003, while the ϕ resolution is about 0.0006 (0.6 mr). Figure 3.6 shows the relative resolution for E_T, again averaged over the acceptance, which is about 2% at an E_T of 100 GeV.

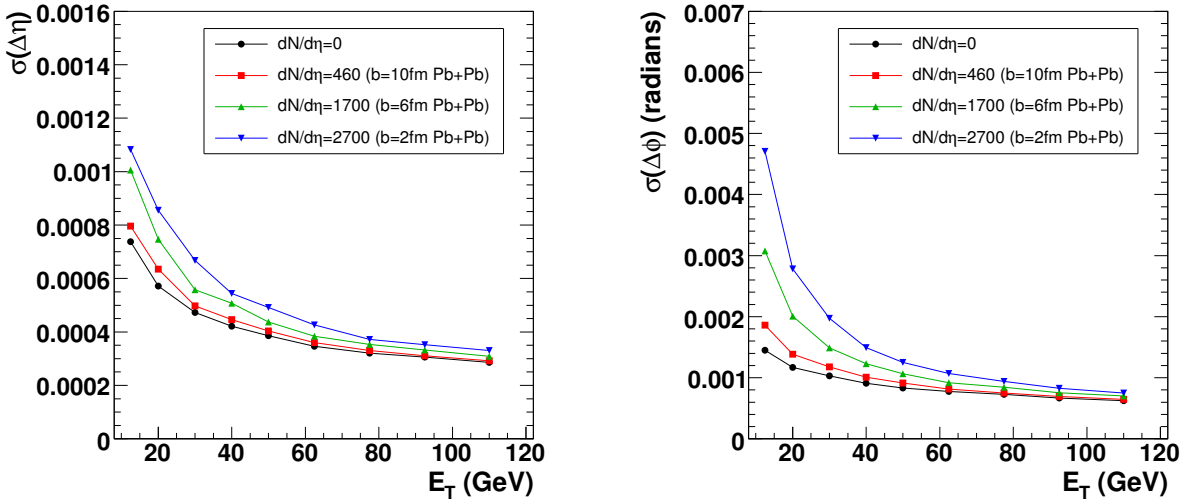

Figure 3.5: Angular resolution, (left) pseudo-rapidity and (right) azimuthal angle, vs. E_T for single photons and single photons embedded in Pb+Pb HIJING events.

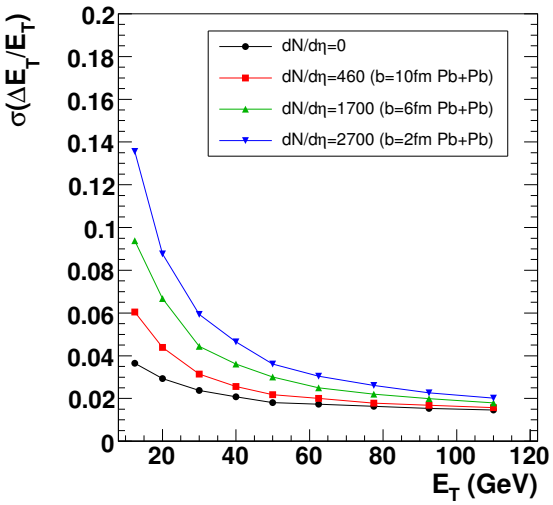

Figure 3.6: Relative energy resolution vs. E_T for reconstructed single photons and those embedded in Pb+Pb HIJING events.

3.3 Isolation cuts

One difference between direct photons and decay photons is that the direct photons are usually isolated but decay photons come from hadrons that are the fragments of jets: jet$\rightarrow \pi^0, \eta \rightarrow \gamma + \gamma$. The decay photons typically merge into one cluster, but they have other hadrons in the neighboring angular space coming from the same original jet. Thus the direct photons can be distinguished from decay photons based on a set of isolation criteria. The isolation cuts are defined by using the charged tracks and total tower E_T in a cone around the jets. These cuts are tuned to maximize the rejection while keeping reasonable efficiency. This is achieved by varying the p_T threshold for charged tracks and the isolation cone size, or by varying the energy sum threshold and corresponding cone size. In general, the isolation efficiency drops with increasing cone size and decreasing p_T threshold or total E_T sum. The rejection, on the other hand, follows the opposite trend. We determine the best cuts separately for three Pb+Pb centralities and p+p and summarize them in Table 3.1. For example the cuts for most central Pb+Pb events requires that all charged tracks in a cone of $0.02 < R < 0.2$ radian should be below 2.5 GeV/c in p_T, and the total energy in a cone of $R < 0.2$ radian surrounding the cluster should be less than $31 + 0.025E_\gamma$ GeV. The requirement of $0.02 < R$ is necessary to avoid false rejection of genuine isolated photons due to conversions.

The performance of the isolation cuts for p+p and central Pb+Pb events is summarized in Fig 3.7. In the most central collisions (corresponding to 0.5% of the cross-section in HIJING), the efficiency is about 65% and the absolute rejection is about 8 for $E_T > 50$ GeV/c. In p+p collisions, the efficiency is about 90% with a absolute rejection factor of about 16 above 50 GeV/c. The increase of rejection with E_T is mainly due to the increase of jet multiplicity and jet energy which makes the isolation cut more effective.

	$dN/d\eta = 2700$	$dN/d\eta = 1700$
Track based cut	$0.02 < R < 0.2$ GeV/c $p_T < 2.5$ GeV/c	$0.02 < R < 0.25$ GeV/c $p_T < 2.5$ GeV/c
Energy based cut	$R < 0.2$ $\sum E_T < 31 + 0.025E_\gamma$ GeV	$R < 0.2$ $\sum E_T < 17.2 + 0.025E_\gamma$ GeV
Efficiency	0.60	0.70
Absolute rejection at 50 GeV	8	10
	$dN/d\eta = 460$	p+p
Track based cut	$0.02 < R < 0.35$ GeV/c $p_T < 2.0$ GeV/c	$0.02 < R < 0.5$ GeV/c $p_T < 1$ GeV/c
Energy based cut	$R < 0.2$ $\sum E_T < 5.6 + 0.025E_\gamma$ GeV	$R < 0.2$ $\sum E_T < 0.9 + 0.025E_\gamma$ GeV
Efficiency	0.70	0.91
Absolute rejection at 50 GeV	14	16

Table 3.1: The isolation cuts used in this analysis for three Pb+Pb centrality bins and p+p collisions. The track based cut requires all charged tracks in the specified cone should have energy below the p_T threshold, similarly the energy based cut require the total energy in the cone surrounding the cluster should have energy less than the threshold.

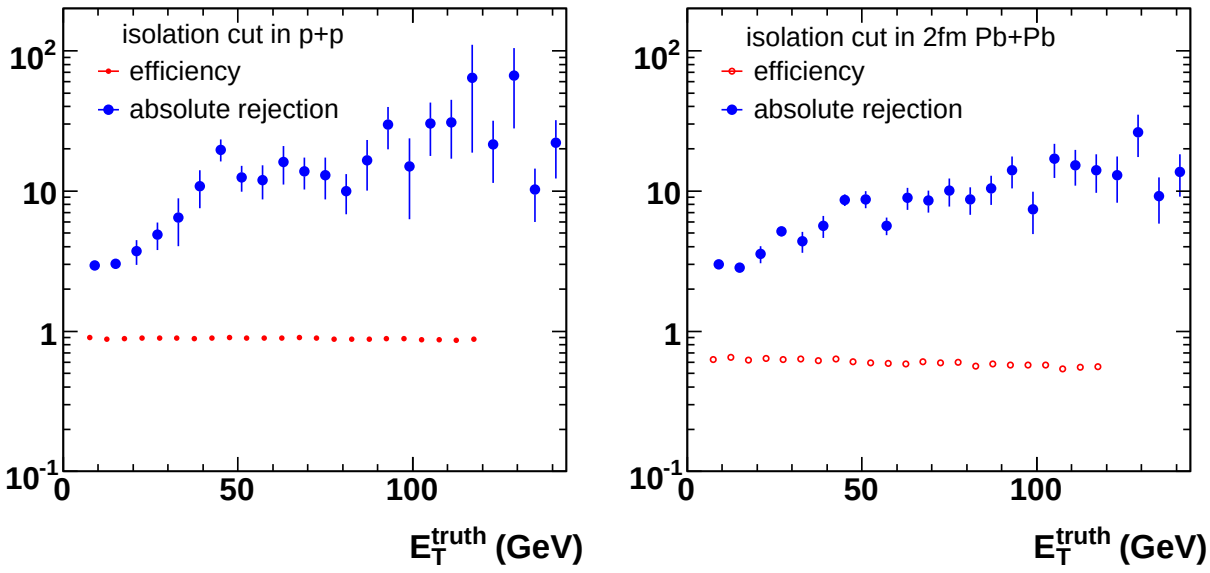

Figure 3.7: The photon efficiency and absolute rejection for background neutral hadrons for the isolation cuts (see Table. 3.1) as a function of energy in (left) p+p and (right) central Pb+Pb events.

3.4 Combined photon identification and isolation cuts

The combined performance for direct γ identification using both the shower shape and isolation cuts is summarized in Fig 3.8. In this study, about 140k PYTHIA di-jets are generated and em-

bedded into the Pb+Pb HIJING events, similar to what was done for jet reconstruction in Chapter 2. To speed up the simulation, these di-jet events were generated with seven $\sqrt{Q^2}$ cuts in the 10–100 GeV range each with comparable statistics, which were then combined into a single jet spectrum by weighting them with the corresponding di-jet cross-section. PYTHIA also provides the spectra of π^0 and η mesons from jet fragmentation. After applying the γ-identification and isolation cuts, we obtain the spectrum of remaining neutral mesons that survive the cuts, which are the background for the direct photons.

To compare with the direct photon yield passing the same set of cuts, the NLO pQCD calculation of Fig. 3.1 is used to generate a realistic hadronic background. The expected direct photon yield is obtained by multiplying the expected spectra of π^0 and η mesons with the ratio $\gamma/(\pi^0+\eta)$. The expected direct photon yield is then multiplied by the measured photon identification efficiency to obtain an estimated reconstructed photon spectrum. Figure 3.8 shows the spectra of jets (open circles), $\pi^0+\eta$ (solid squares), $\pi^0+\eta$ passing the cuts (solid circles), expected γ (solid line), and expected γ passing the cuts (dashed line). As the figure shows, above 60 GeV/c, the cuts suppress the yield of background neutral hadrons below the direct photon yield.

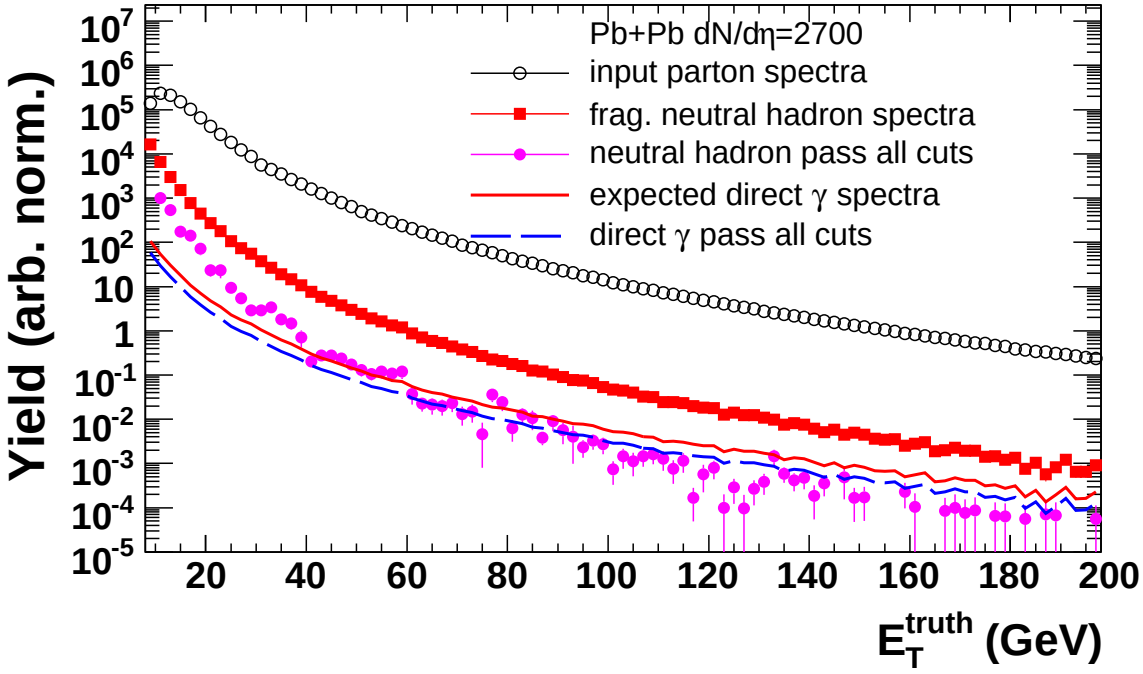

Figure 3.8: The performance of the shower shape cuts and isolation cuts on PYTHIA di-jets embedded into $b = 2$ fm Pb+Pb events. The spectra shown are for input jets (open circles), input $\pi^0+\eta$ (solid square), remaining $\pi^0+\eta$ (solid circles), expected direct γ (solid line) and remaining direct γ (dashed line).

Figure 3.9 shows the ratio of direct photons to remaining neutral hadrons passing the cuts as function of photon energy in central Pb+Pb events. Assuming no suppression for neutral hadrons, $S/B = 1$ is reached for 100 GeV/c photons (left panel). By assuming a factor of 5 suppression of high p_T yields for π^0 and η, the S/B is improved by a factor of 5, which leads to a $S/B \sim 1$ for 30 GeV photons. This should be compared with the original S/B, which is less than 0.1 below

100 GeV according to the NLO pQCD calculations shown in Fig. 3.1. Note that the improvement of S/B towards high E_T is partly due to the increase of $\gamma/(\pi^0+\eta)$ ratio.

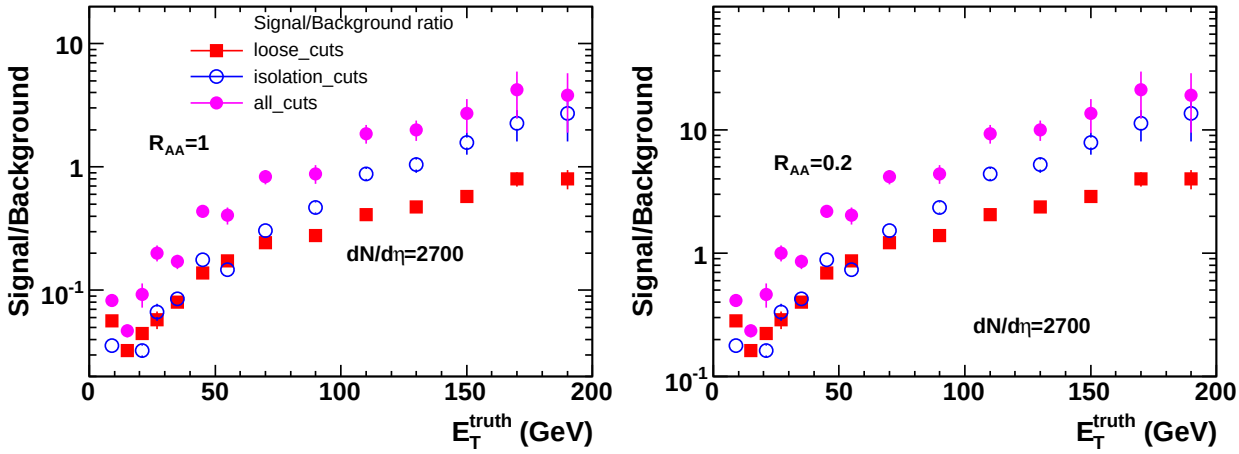

Figure 3.9: The ratio of direct photons over background neutral hadrons passing the the loose shower shape cuts only (solid squares), isolation cuts only (open circles) and combined cuts (solid circles) in central Pb+Pb events, assuming (left) no suppression for hadrons, and (right) a factor of 5 suppression for hadrons.

The centrality dependence of the direct photon performance is summarized in Fig. 3.10. The S/B ratio is the best in p+p collisions, which is about factor of 4–5 larger than that for most central Pb+Pb events. However, by taking into account the benefit one gains from the likely hadron suppression, we expect to achieve a similar level of performance that is approximately independent of the event centrality.

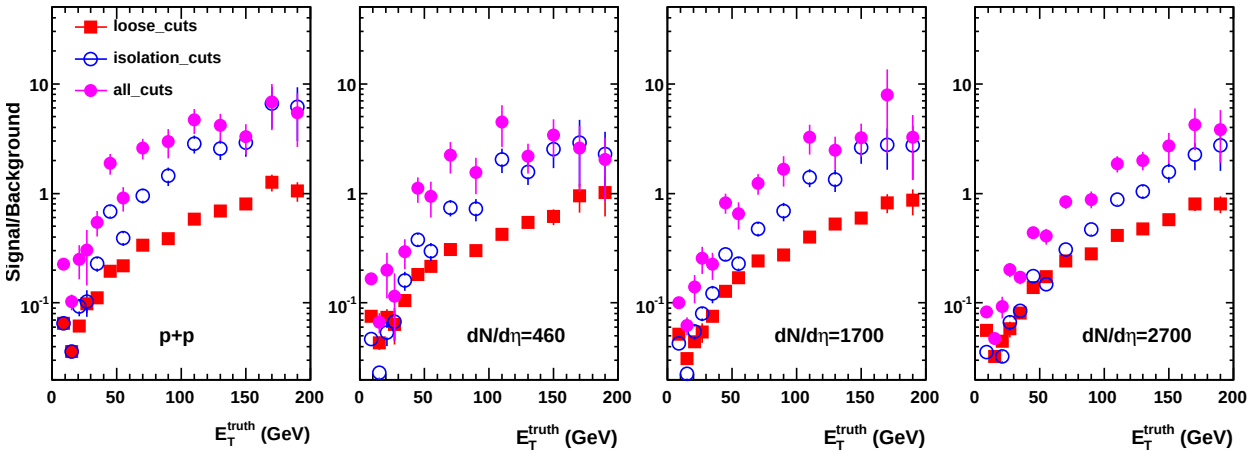

Figure 3.10: The ratio of direct photons over background neutral hadrons passing the loose shower shape cuts only (solid squares), isolation cuts only (open circles) and combined cuts (solid circles) for different occupancies under the assumption that $R_{\rm AA} = 1$ for all centralities.

3.5 Rate estimate

The number of expected direct photons observed per year is based on the following assumptions:

- 3 weeks/year running at 60% up time, which gives 0.5nb^{-1} integrated luminosity for minimum bias Pb+Pb collisions.
- Estimation of the direct photon yield based on the next to leading order pQCD calculation shown in Fig. 3.1.
- Photon reconstruction efficiency of 50% passing the shower shape and isolation cuts.
- π^0's and η are suppressed by a factor of 5 in central Pb+Pb collisions.

Based on these assumptions, 200k (10k) γ will be measured above 30 GeV (70 GeV) per LHC year with $S/B > 1$ ($S/B > 4$).

3.6 γ-jet correlations

Once the direct photons are cleanly identified, the away-side jet can be reconstructed and it is feasible to study the correlation between the γ and jet. A first attempt at measuring such a coincidence has been made. A set of PYTHIA γ-jet events was generated and embedded into the same set of HIJING events without quenching used for the jet performance study. Jet reconstruction was performed using the seeded cone algorithm with $R = 0.4$ and 5 GeV seed towers as described in Section 2.3. The photons were measured using the cuts outlined in Table 3.1.

Two different energy ranges for γ-jet correlations are shown in Figure 3.11. The left panel shows the $\Delta\phi$ correlation between isolated photons from 40–60 GeV with jets from 40–60 GeV. A clear jet signal peak around $\Delta\phi = \pi$ is visible above the low, flat background. The right panel shows a similar correlation for isolated photons and jets in 60–80 GeV range. The jet signal peak is more significant comparing to the low background. In the 40–60 GeV energy range, fake jets were removed by applying the same rejection cut on $\sigma_{j_T^{\rm Sum}}$, which was used in the jet performance study (see discussion in Section 2.3 and Figure 2.9). This was not applied for 60–80 GeV bin, therefore, this correlation shows the upper limit of the expected background. The γ-jet S/B as a function of the fake jet rejection cut is shown in Fig. 3.12. The cut used to remove fake jet was $\sigma_{j_T^{\rm Sum}} < -2.5$. These γ-jet correlations can be used to improve jet energy scale calibration, to reject background jets and to increasing the reconstruction efficiency by testing for a coincidence with isolated photons.

3.7 Unique ATLAS capabilities

ATLAS's large acceptance allows full jet reconstruction in 2π and up to 10 units in pseudo-rapidity ($|\eta| < 5$) with $> 50\%$ efficiency for jets above 50 GeV in central Pb+Pb collisions (see Fig.2.12). The results shown in this chapter show that ATLAS can reconstruct a highly-pure sample of direct photons above $E_T = 20$ GeV over nearly 5 units in pseudo-rapidity ($|\eta| < 2.4$) with a constant 60% efficiency even for central Pb+Pb collisions with $dN/d\eta = 2700$. Combined with the measurement of global properties of the collision (as discussed in Chapter 4), this should allow a detailed study

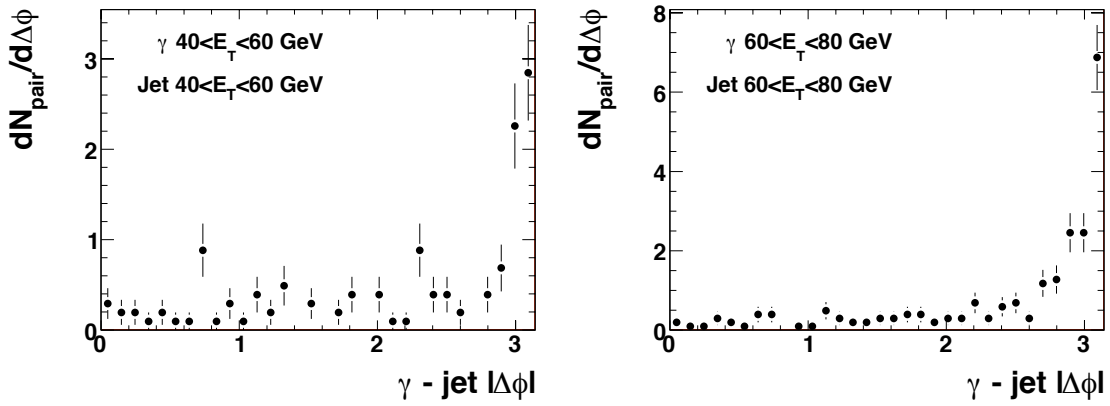

Figure 3.11: Correlations in $\Delta\phi$ for *gamma*-jet pairs where both the photon and the jet have 40-60 GeV (left) and 60-80 GeV (right) in E_T.

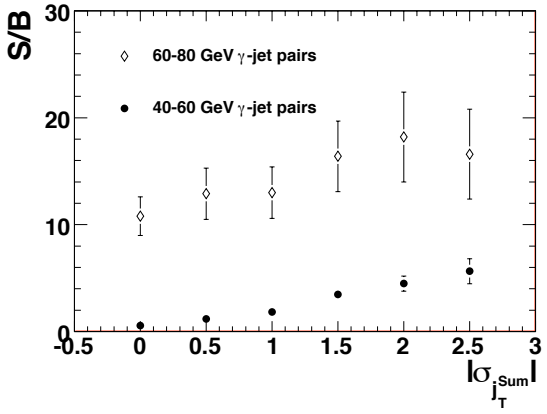

Figure 3.12: The resulting γ-jet signal-to-background in the peak region for both sets of E_T bins.

of γ-jet tomography as a function of centrality and angle relative to the reaction plane in a broad E_T and η range.

ATLAS's sophisticated calorimeter system provides γ and γ-jet capabilities which are competitive, and often superior, compared to ALICE and CMS. Compared to ALICE, the advantage of the ATLAS detector lies in its large detector acceptance (see Figure 10.1) coupled with its high rate triggering capability. Compared to CMS, which also has a large acceptance calorimeter and a similar trigger system, the advantage of the ATLAS design is its longitudinally segmented calorimeter, and especially the finely-segmented strips in the first layer. This will allow the discrimination between γ's and neutral hadrons independent of the isolation cuts. In the case of γ-jet, this should allow ATLAS to extend the measurements down to $E_T = 20$ GeV.

One area where the ATLAS calorimeter provides capabilities completely unmatched by the other LHC experiments is the measurement of medium induced photons over the full experimental acceptance. Recent theoretical calculation constrained by existing photon data have suggested

that direct photons coming from final-state sources — such as fragmentation, in-medium gluon conversion and medium-induced bremsstrahlung — can dominate the direct photon yield up to $p_T = 50$ GeV/c [103]. These are compelling phenomena to address since their production rate directly reflects the interaction of quarks and gluons as they propagate through the medium.

Fragmentation and medium-related photons are not straightforward to measure in general, as they are produced close to the primary jet, and thus can not be extracted using isolation cuts. Fortunately, the first layer of the ATLAS electromagnetic calorimeter, as discussed in section 3.2, has sufficiently fine segmentation in η that it can resolve fragmentation photons even within jets. Fig.3.4 suggests that even without isolation, a tight γ identification cut can provide a unbiased, centrality-independent relative rejection factor of 3 to 5 against the hadronic decay background with about 50% efficiency for the photons. Assuming the yield of medium-induced photons is roughly equal to that of prompt photons, as suggested by recent NLO calculations, a S/B of about 0.3 will be achieved at around $E_T = 50$ GeV/c in central Pb+Pb collisions. This will allow a statistical subtraction of the hadronic background and facilitate the first measurement of medium-induced photons in heavy ion collisions over a large acceptance, and thus down to very low x.

3.8 Summary

This chapter has presented the ATLAS performance for direct photon identification and γ-jet correlations.

- The first layer of the ATLAS EM calorimeter provides an unbiased relative rejection factor of either 1.5–3 (loose shower shape cuts) or 3–6 (tight shower shape cuts) for neutral hadrons.
- The loose γ identification cuts can be combined with isolation cuts which can provide an additional factor of about 10 relative rejection. This results in a total relative rejection of about 20 even in central Pb+Pb collisions.
- The photon efficiency is constant at 60% down to $E_T = 20$ GeV for central Pb+Pb allowing the study of medium modification for low-E_T jets.
- Identified direct photons can improve the reconstruction efficiency and S/B significantly for jets below 80 GeV/c, relative to the performance for jet reconstruction without tagging.
- The tight shower shape cuts alone provide sufficient rejection against hadron decays within jets to allow the study of fragmentation photons, in-medium gluon conversion and medium-induced bremsstrahlung. This is a unique capability of ATLAS.
- The expected luminosity per LHC Pb+Pb year will provide 200k photons above 30 GeV with $S/B > 1$, and 10k above 70 GeV per LHC year with $S/B > 4$.

Chapter 4

Global observables

This chapter will discuss the ATLAS capabilities for measuring several "global" observables, by which are meant: charged-particle multiplicities, transverse energy, and elliptic flow. Of course, a precise estimation of event centrality is an essential part of measuring any of these variables, and so will also be discussed. Global variables have the paradoxical role of being integrals of particle number and energy in the final state, but which appear to reflect dynamical quantities (e.g. entropy, transverse energy) established much earlier in the system evolution. Most importantly, they provide access to aspects of the system relevant to understanding the nature of the strongly coupled fluid. The particle multiplicities should be directly relevant to the initial state entropy. The elliptic flow reflects a combination of the equation of state (EOS) as well as the shear and bulk viscosities.

Global variables will certainly be the focus of Day-1 physics activities at the LHC, when heavy ion collisions are delivered to the experiments sometime in 2009 or 2010. Even with low to moderate luminosity, 50 Hz taken to tape will amount to 2 million Pb+Pb events per day, providing sufficient data within a few days to test extrapolations of RHIC data to LHC energies. As part of this process, the measurements of similar variables in proton-proton collisions (which will most likely be the first data published from the ATLAS detector) will be essential preparation for heavy ion data taking, trigger preparation, and analysis – and work on this is already underway.

4.1 Global physics at the LHC

While it is difficult to calculate features of soft particle production from first principles in the complicated environment of a heavy ion collision at high energies, it is found that global observables follow relatively simple patterns which may eventually give some insight into the bulk (and generally non-perturbative) sector of QCD. At the same time, measurements of inclusive charged particle density will be essential for an empirical understanding of particle production in these collisions, and will help constrain the gluon densities that will be needed for jet quenching calculations.

Various predictions for inclusive particle production at the LHC have been made, that test the applicability of different theoretical approaches already applied at RHIC. Three of these predictions for $\rho(s) = (dN_{ch}/d\eta)/(N_{part}/2)$ are shown in Fig. 4.1, overlaid on data from p+p and A+A. The first is the simple $\log(s)$ trend that is often invoked as a description of data from AGS to

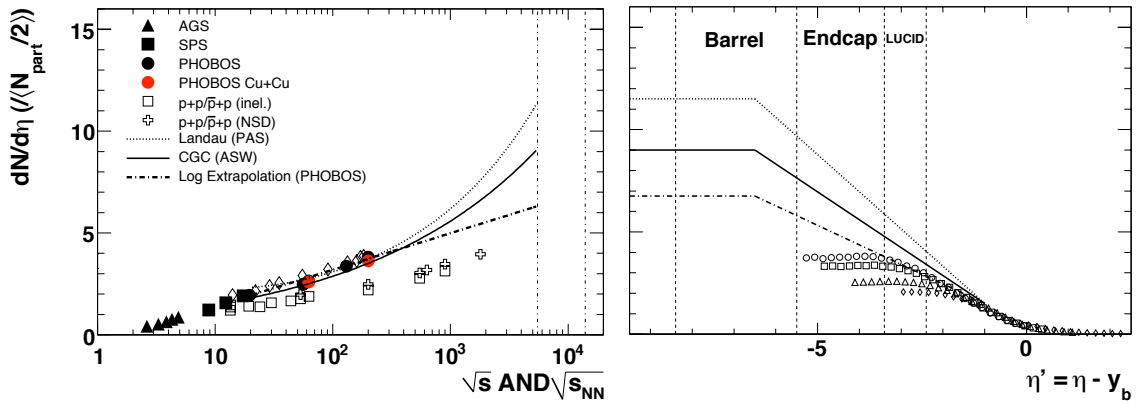

Figure 4.1: (left) Data for $dN_{ch}/d\eta(|\eta| < 1)$ vs $\sqrt{s}$ for A+A and p+p collisions, compared with three theoretical extrapolations[104, 105, 106]. (right) Capabilities of ATLAS detector, in the rest frame of one of the projectiles, compared with RHIC data. The lines show how extended longitudinal scaling behavior might appear, given the mid-rapidity predictions of the three models in the left panel.

RHIC energies, and thus may well be relevant at the LHC [107]. This extrapolates to a value of around 6.5 at $\sqrt{s_{NN}} = 5520$ GeV, which is the lowest value considered. The second is a functional form suggested by Color Glass Condensate-based models, $\rho(s) = N_0 s^{\lambda}$, with λ being extracted from scaling violations measured at HERA [104]. With parameters taken from Ref. [104], which misses the RHIC data by about 10%, one gets $\rho(s) \sim 9$, corresponding to $dN_{ch}/d\eta \sim 1600$. Finally, Carruthers' version of Landau's hydrodynamical model gives a functional form proportional to $s^{1/4}/\sqrt{\log(s)}$ with no free parameters[105]. Tuned to the RHIC data, as was done in Ref. [106], this function extrapolates to $\rho(s) \sim 11.5$. Clearly, within a few days of first LHC running, entire classes of models may be excluded, and new data will be added to this compilation. This example illustrates that essentially every measurement of global variables will contribute to our understanding of heavy ion collisions, a situation which is unique to the heavy ion program, even with p+p, and especially if the machine ramps up slowly, exploring different energies for short periods of time.

At RHIC there was a general expectation that particle production and transverse energy would arise from a combination of soft processes and semi-hard process, each with a distinct scaling with the nuclear geometry. Soft processes are thought to deal with long wavelength excitation processes and thus scale with the number of excited (or "wounded") participant nucleons. Semi-hard processes, or mini-jets, while at a lower energy scale than usually considered for isolated jets, are thought to scale with the number of binary collisions (which exceed the number of participant pairs $N_{part}/2$ by a factor of ~ 10). These assumptions are the basis for the "two-component" model for inclusive particle production:

$$\frac{dN}{d\eta} = n_{pp}\left[(1-x)\frac{N_{part}}{2} + xN_{coll}\right] \tag{4.1}$$

At the same time, RHIC data on ratios of $\rho(s)$ at different N_{part} and different $\sqrt{s}$, have shown that $\rho(s)$ "factorizes" as $f(s)g(N_{part})$ [108]. This is apparently at odds with the two-component

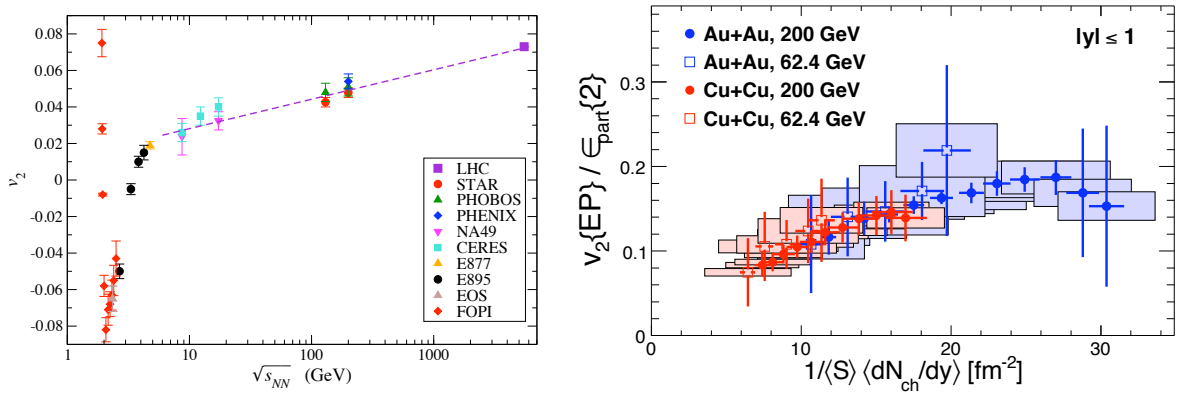

Figure 4.2: (left) Compilation of data on v_2 vs. $\sqrt{s}$ in heavy ion collisions, from Ref. [104]. (right) Data for v_2/ϵ vs. the areal density of charged particles, for two energies and two colliding systems, from Ref. [110].

model, even at RHIC, but the interpretation remains controversial. Thus, the LHC will provide the definitive test of the role of semi-hard processes in the entropy of the sQGP. The addition of E_T measurements as a function of centrality will provide additional insights into whether there is an increase in transverse activity due to the presence of minijets scaling with N_{coll}.

While the previous discussion involved the inclusive charged particle multiplicity near mid-rapidity, the large acceptance will also play a crucial role in the elucidation of global properties. One key observation away from mid-rapidity at RHIC was that of "extended longitudinal scaling" [109]. This phenomenon, shown in the right panel of Fig.4.1, characterized by the fact that the normalized inclusive yields are invariant with energy when viewed in the rest frame of one of the projectile, by plotting yields as a function of $\eta' = \eta - y_b$. It is also observed that while the phenomenon is observed at all centralities, the invariant yield vs. η' varies with centrality. The same figure also shows how the various ATLAS sub-detectors are situated in η' space, illustrating the dramatic extension to large negative η' as well as the overlap in the forward region. While the silicon and tracking detectors only extend to $\eta = 2.5$, the calorimeters provide measurements out to $\eta = 5$, and the LUCID detector (Cerenkov tubes) should provide multiplicity measurements of primaries out to $\eta = 6$, overlapping the RHIC data.

Elliptic flow, which is manifest as a significant anisotropy in the event-by-event azimuthal distribution of inclusive particles, is one of the more striking phenomena observed at RHIC. The azimuthal modulation is typically characterized by the second Fourier coefficient v_2

$$\frac{dN}{d\phi} \propto 1 + 2v_2 \cos\left(2\left[\phi - \Psi_R\right]\right) \tag{4.2}$$

where Ψ_R is the angle of the "reaction plane" (defined by the vector connecting the centers of the colliding nuclei). This quantity has been measured over a wide range of energies, collision systems, and centralities by all of the RHIC heavy ion experiments and several AGS and SPS experiments. A compilation of v_2 vs. $\sqrt{s}$ for minimum-bias heavy ion collisions, is shown in the left panel Fig. 4.2, from Ref. [104]. While there is a non-monotonic behavior observed below $\sqrt{s} = 4 - 5$ GeV, above this energy (including the AGS, SPS, and RHIC data) a logarithmic rise

is observed. The further energy dependence is difficult to predict from first principles, as it depends on the details of the initial state and on the EOS. It has been suggested by some authors that the logarithmic rise could continue to higher energies (reaching $v_2 \sim 0.7$ at LHC energies for minimum-bias samples), while others have suggested that the "hydro limit" may already have been reached at RHIC, implying no further rise in v_2. This hypothesis has been tested by correlating v_2/ϵ (where ϵ is a measure of the spatial eccentricity of the initial state) with $dN_{ch}/dy/S$ (where S is the area of the nuclear overlap region), shown in Fig. 4.2 from Ref. [110]. This plot seems to show a constant rise of elliptic flow as the areal density of charged particles increases, but some still see a flattening at large value of $dN_{ch}/dy/S$. Finally, some authors predict that elliptic flow at the LHC may even decrease [111]. As with the multiplicity predictions, only the LHC will provide enough of a lever arm to really test these hypotheses.

4.2 ATLAS capabilities

The ATLAS detector has unprecedented acceptance and hermeticity for the measurements of global variables. Whereas at RHIC, experiments have had to make serious choices optimizing acceptance vs. capability (e.g. choosing large aperture tracking and limited calorimetry, or vice versa), the ATLAS detector has a full 10 units of rapidity coverage for calorimeter, both electromagnetic (EM) and hadronic, and 5 units of rapidity for tracking. There is also substantial forward coverage beyond the central detector, with the LUCID counter being staged in from $5.3 < |\eta| < 6$ and especially the ZDC being built by the ATLAS Heavy Ion group, which detects neutral particles with $|\eta| > 8$[109]. The ZDC also has a position-sensitive front face that can be used to estimate directed flow (v_1), as discussed in Chapter 6.

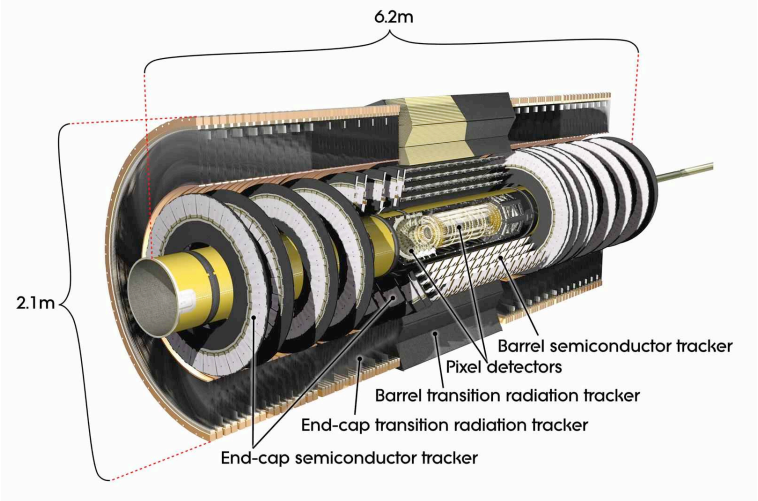

Figure 4.3: Layout of the ATLAS Inner Detector, with the Pixel detector, SCT detector, and TRT indicated.

The ATLAS Inner Detector (ID) has been designed to track charged particles in 5 units of pseudo-rapidity centered around mid-rapidity [112]. The detector combines three technologies,

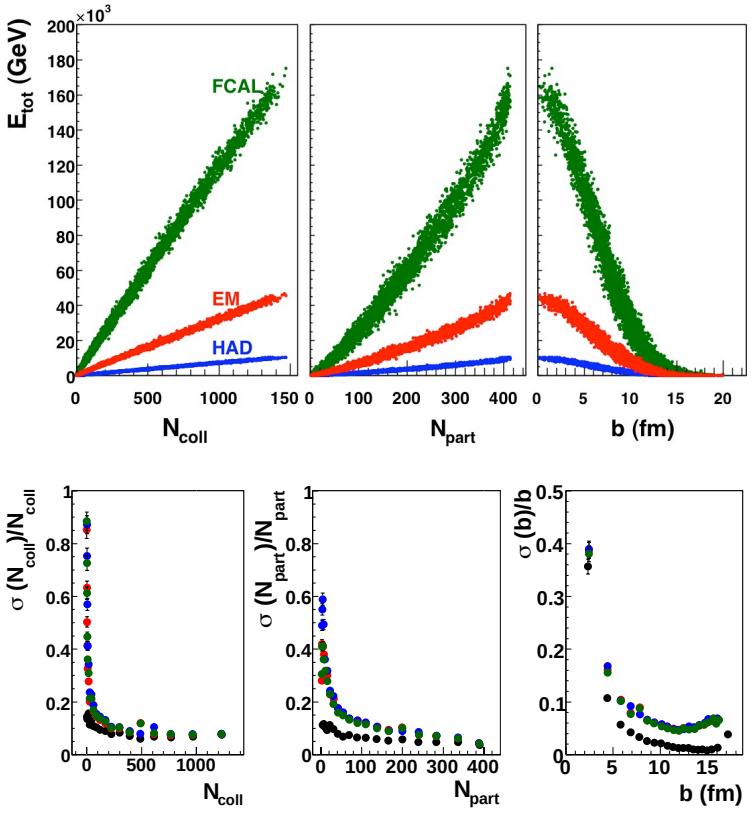

Figure 4.4: (above) Correlation of the total energy measured by the FCAL (top), EM calorimeter (middle), and Hadronic Calorimeter (bottom) correlated with N_{part}, N_{coll} and impact parameter (b). (below) Width of distributions of N_{part}, N_{coll} and b, corresponding to bins in E_{tot} for FCAL, EM, and HAD.

closest to the beam, tracking is done with silicon pixel detectors (Pixel) arrayed in a barrel with three layers (B-layer, Layer 1 and Layer 2) and 6 end-cap sections. The Pixel end-cap sections are mounted on disks perpendicular to the beam axis and placed on both sides of the nominal interaction point. The Pixel detector is followed by the Semiconductor Tracker (SCT) consisting of double-sided silicon strip detectors arranged in four layers in the barrel, and two sets of 9 end-cap disks located on both sides of the nominal interaction point. The third tracking detector is a Transition Radiation Tracker (TRT) based on drift tubes arranged in a barrel and 2 endcaps. The ID was designed with an high granularity to cope with the high luminosity expected in p+p collisions, which leads to multiple p+p collisions in each LHC bunch crossing. The granularity turns out to be essential for tracking charged particles produced in the high-multiplicity environment of heavy ion collisions in a wide pseudo-rapidity window.

4.3 Event centrality

The event-by-event characterization of centrality is a fundamental observable in heavy ion physics, since most global observables closely track the event geometry as controlled by the impact parameter (the distance b between the centers of the two colliding nuclei). A simple example is the charged particle multiplicity which predominantly scales proportionally to the number of participating nucleons (N_{part}), but has sub-dominant contributions that seem to scale proportionally to the number of binary collisions (N_{coll}). This simple fact implies that the total energy will correlate very tightly with any of the three standard event centrality observables (N_{part}, N_{coll} and b), something shown with HIJING simulations in the top panel of Fig. 4.4. The energy is particularly large in the FCAL due to the longitudinal boost of forward-going particles ($E \sim m_T \cosh(y)$).

The strong correlation implies that one can bin each of these variables into percentile bins (e.g. the most central 0-10% events, 10-20%, etc.) and relate these to similar percentages of the N_{part}, N_{coll} and b distributions. This is a standard technique used by all heavy ion experiments [113], which only requires the multiplicity to vary monotonically with the impact parameter. Ultimately the limiting factor in a precise estimation is the uncertainty in knowing what fraction of the total inelastic A+A cross section is sampled by the experimental trigger, something that is difficult for all LHC experiments. However, if one assumes this can be determined precisely, then one can bin the HIJING variables and extract the width of the centrality variable distributions in each bin, as shown in the bottom panel Fig.4.4.

The Zero Degree Calorimeter (ZDC), discussed in Chapter 6, will also be an important contribution to the characterization of event centrality. Most importantly, it will provide a high efficiency minimum bias event trigger for Pb+Pb collisions, which will be important for reducing the systematic errors on centrality observables. It will also provide the total spectator energy, which should anti-correlate with the energies in the other ATLAS calorimeters, thus verifying the assumption that the multiplicity varies monotonically with the impact parameter.

4.4 Charged particle multiplicity measurements

Despite the limited efficiency at low p_T, ATLAS provides several methods of estimating the total inclusive particle yield event-by-event. The limits of the tracking system to register particles at low values of transverse momentum (discussed below) require the use of different approaches, of varying redundancy.

The first method uses the three pixel layers as three separate sub-detectors, and corrects the event-by-event hit distribution as a function of η. The left panel of Fig. 4.5 shows the correction factor for the three pixel layers (from top to bottom: Layer 2, Layer 1 and the B Layer, which is the closest layer to the beam pipe). It also shows the corrections for three centrality bins (peripheral, mid-central, and central) illustrating the relative insensitivity of the detector to the large variations in particle multiplicity. These corrections are applied to single events in in the right panels of Fig. 4.5, the middle figure being for a high-multiplicity $b = 2$ fm event, and the rightmost figure for a $b = 10$ fm peripheral event. The histograms in each case show the HIJING truth charged particle density, while the circles show the reconstructed $dN_{ch}/d\eta$. While deviations are certainly observed, the quality is quite good considering the large corrections at large η.

Another method using the Pixel detector is the "tracklet" approach, most notably used in heavy ion collisions by the first PHOBOS paper. As shown in the left panel of Fig. 4.6, the idea is

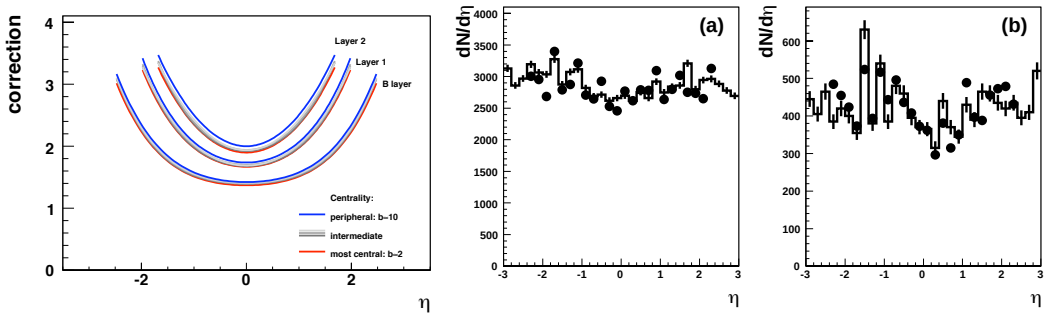

Figure 4.5: Multiplicity measurements in the pixel detector: (left) correction factors applied to the raw number of hits as a function of η, centrality, layer and (right) single peripheral and central events reconstructed.

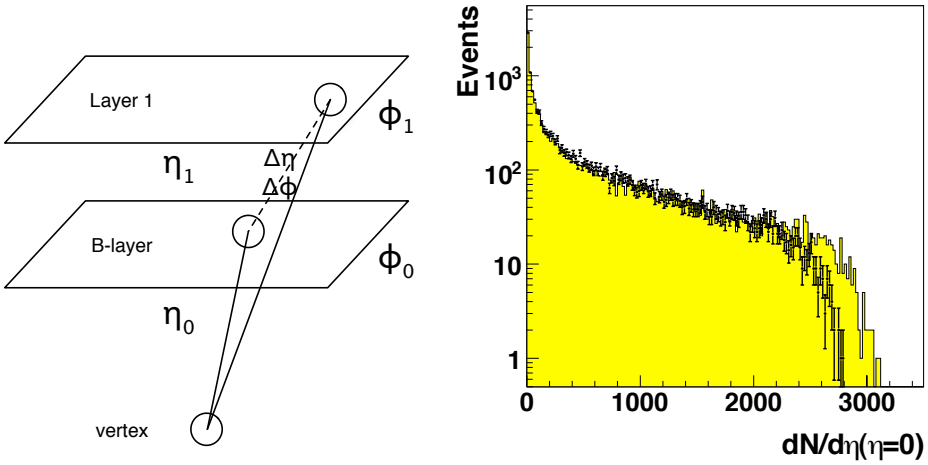

Figure 4.6: (left) Schematic diagram showing how tracklets are defined (right). Distribution of $dN_{ch}/d\eta$ from HIJING events (open histogram) and reconstructed using the tracklet method event-by-event, but without efficiency corrections (yellow histogram)

to use the event vertex (determined by whatever means are available, e.g. with higher p_T tracks), and use this to seed vectors based on correlated hits in the first two Pixel layers (B layer and Layer 1). A tracklet is thus a three point track characterized by the event vertex, the η and ϕ of the hit in the inner-most pixel layer, and residuals $\Delta\eta$ and $\Delta\phi$ between that hit and a hit in Layer 1. The residuals are used both to cut away non-correlated hits (in this case $\Delta\eta < 0.08$ and $\Delta\phi < 0.8$), as well as to estimate the track momentum in low-multiplicity events. The set of tracklets selected by this method can then be used to estimate the particle density, with very little background. A distribution of the uncorrected number of tracklets integrated over $|\eta| < 1$ compared with HIJING truth is shown in the right panel of Fig. 4.6. This shows that even without correction, the tracklet method gives a good estimate to the event-by-event multiplicity, allowing the study of

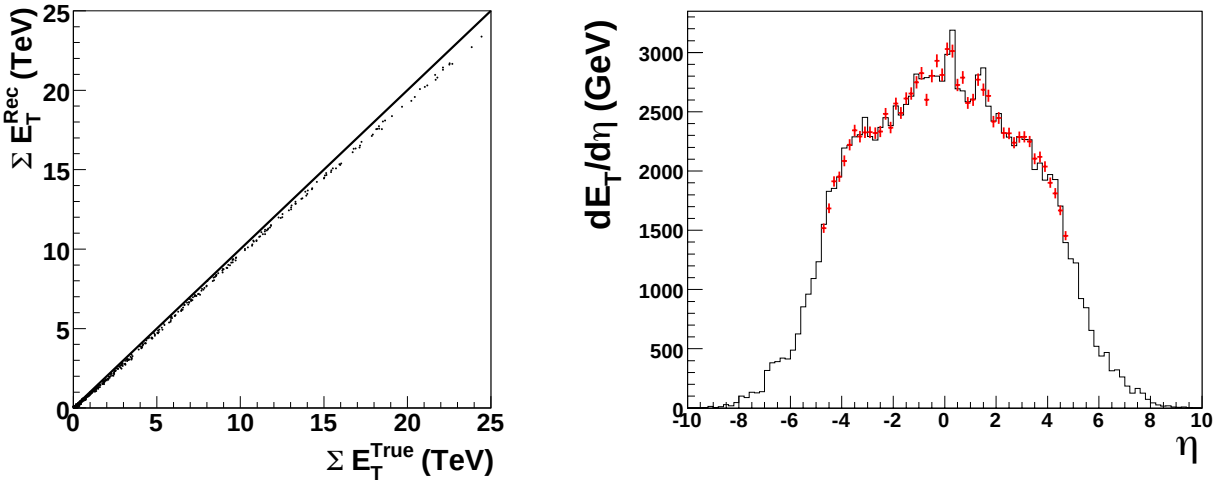

Figure 4.7: Transverse energy measurements performed using the method described in the text, both (left) integrated E_T compared with HIJING truth, and (right) differential $dE_T/d\eta$ for a single $b = 2.3$ fm event.

fluctuations as well as mean values.

4.5 Transverse energy measurements

The hermetic calorimetry of the ATLAS detector provides coverage for transverse momentum measurements out to $|\eta| = 5$, including both electromagnetic (EM) and hadronic (HAD) energy. Total E_T observables can be defined by summing the E_T in individual calorimeter cells, with η-dependent corrections $c(\eta) = E_T^{\text{reco}}(\eta)/E_T^{\text{truth}}(\eta)$ determined by Monte Carlo studies:

$$E_T^{tot} = \sum_i E_{T,i}^{cell}(\eta,\phi) \times c(\eta) \tag{4.3}$$

$$\frac{dE_T}{d\eta}(\eta) = \frac{1}{\Delta\eta}\sum_i E_{T,i}^{cell}(\eta,\phi) \times c(\eta) \tag{4.4}$$

Results from these variables are shown, without correction, in Fig. 4.7 for total E_T for a sample of HIJING events, and for $dE_T/d\eta$ for a single HIJING event with $b = 2.3$ fm. The tight correlation of the reconstructed and true E_T (for $|\eta| < 5$), shows the hermeticity of the calorimeter. The differential E_T measurement also shows sensitivity to the local details of the event. The studies done so far suggest that additional energy corrections will be minimal for these large regions of phase space.

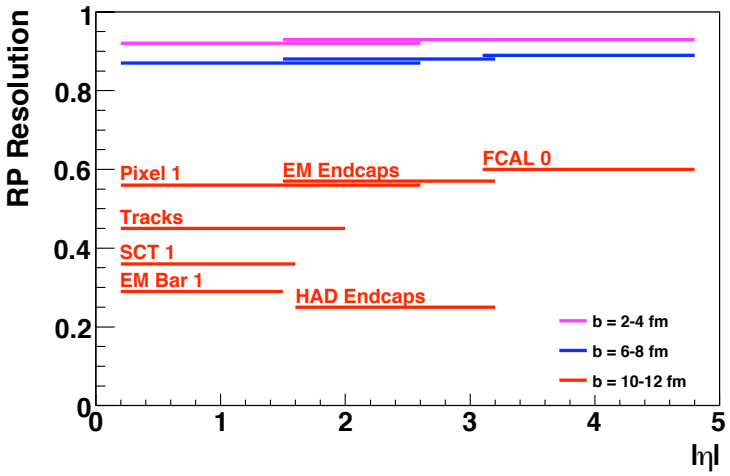

Figure 4.8: Reaction plane resolutions for different ATLAS sub-detectors shown as a function of $|\eta|$ and centrality.

4.6 Elliptic flow

Unlike many previous experiments, which have typically a single detector system with the broad coverage in η and ϕ needed for a proper estimation of the reaction plane, essentially every sub-detector system in ATLAS has full azimuthal coverage and a large pseudo-rapidity acceptance. The event plane, which is related to the proper reaction plane but is determined via the emitted secondaries, is measured via the formula derived in Ref. [114]

$$\Psi_n = \frac{1}{n}\tan^{-1}\left(\frac{\sum w_i \sin(n\phi_i)}{\sum w_i \cos(n\phi_i)}\right) \tag{4.5}$$

The resolution is quantified experimentally, with no reference to the true angle, by the correlation of separate sub-events at forward and backward rapidities via the formula [115]:

$$R \equiv \sqrt{\langle \cos\left(2\left[\Psi_2^1 - \Psi_2^2\right]\right)\rangle} \tag{4.6}$$

which typically scales as Nv_2^2. Figure 4.8 shows the results for R for seven different sub-detectors, each sensitive to different particles (charged vs. neutral) and different rapidity regions. In all cases $R > 0.3$ but in general is is above 0.6, indicating the favorable conditions for measuring v_2 at the LHC (both large v_2 and large multiplicities). The excellent event plane resolution should allow for fine binning in studies of correlations of hard processes with the collision geometry.

With the event plane determined above, v_2 is extracted via this formula calculating the second fourier coefficient relative to the event plane.

$$v_2 = \langle \cos(2[\phi - \Psi_2]) \rangle \tag{4.7}$$

(the "RP" method), or by fitting the angular distribution relative to the event plane.

Sub-system	η - coverage for sub-events	Resolution correction		
		$b = 10 - 12$ fm	$b = 6 - 8$ fm	$b = 2 - 4$ fm
EM Barrel Layer 1	$0.2 < \|\eta\| < 1.5$	0.29 ± 0.06	0.70 ± 0.02	0.81 ± 0.01
EM EndCaps	$1.5 < \|\eta\| < 3.2$	0.57 ± 0.03	0.88 ± 0.01	0.93 ± 0.01
HAD EndCaps	$1.6 < \|\eta\| < 3.2$	0.25 ± 0.07	0.59 ± 0.03	0.74 ± 0.02
FCAL Layer 0	$3.1 < \|\eta\| < 4.8$	0.60 ± 0.03	0.89 ± 0.01	0.93 ± 0.01
Pixel, 1st layer	$0.2 < \|\eta\| < 2.6$	0.56 ± 0.03	0.87 ± 0.01	0.92 ± 0.01
SCT, 1st layer	$0.2 < \|\eta\| < 1.6$	0.36 ± 0.05	0.71 ± 0.01	0.76 ± 0.01
Reconstructed tracks	$0.2 < \|\eta\| < 2.0$	0.45 ± 0.04	0.85 ± 0.01	0.92 ± 0.01

Table 4.1: Resolution corrections calculated for different sub-systems for the simulated events with different centralities and with the constant flow of 5%.

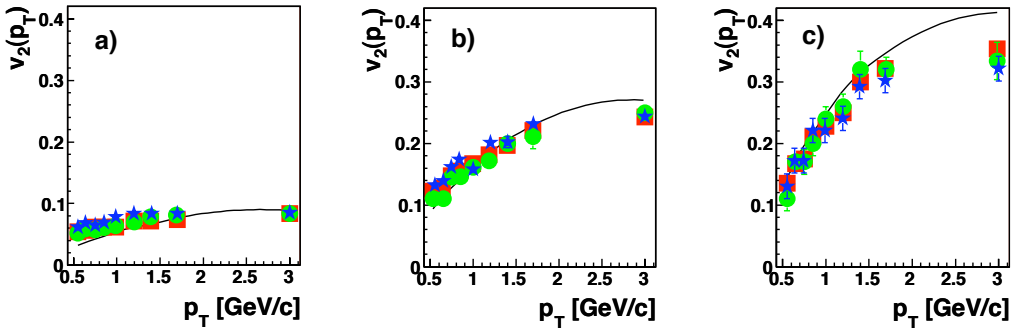

Figure 4.9: Reconstructed $v_2(p_T)$ using the RP method (red squares) as a function of p_T for three different centralities – a) 2.3 fm, b) 7.0 fm and c) 10.7 fm – compared to truth (black line), the two-particle correlation method (blue stars) and Lee-Yang Zeros (green circles).

Fig. 4.9 shows a study of reconstructing a p_T-dependent v_2 signal, incorporated into HIJING events with $v_2(p_T)$ based on parameterizations of RHIC data. Even in these early studies, the reconstruction quality using the RP method [115] (comparing red squares to the black line indicating the input flow) is quite good over the full p_T range, except perhaps in the highest p_T bins. The RP method is also compared to a method based on two-particle correlation functions, where a track at a given p_T is correlated with the other tracks or hits in the event [15]. The two-particle correlation method does a similarly good job for the bulk of particle production. A third method is also shown, based on the Lee-Yang Zeroes (LYZ) method of Ref.[116], which has somewhat better performance at low p_T than the correlation method.

4.7 Inclusive charged particle spectra

The ATLAS inner detector can be used to estimate the momentum spectrum of inclusive charged particles, which can contribute to measurements of charged particle multiplicity, transverse en-

ergy (via the mean p_T), and elliptic flow. This section describes the application of a standard ATLAS tracking algorithm to heavy ion events. A first reconstruction of particle spectra is performed.

The ATLAS tracking algorithm uses the Kalman filter method [117] (called "xKalman") to do a simultaneous pattern recognition and track fitting in its three detector sections. Track candidates are formed from combinations of hits in the Pixel detector. These tracklets are then propagated outward taking into account the value of the magnetic field and the effect of multiple scattering due to the material traversed. Once the outer edge of the inner detector is reached, the process can be repeated backwards to improve the quality of the track fit. In order to define the tracking efficiency, a set of quality cuts is applied to all reconstructed tracks. This particular set of cuts may well evolve once actual data is available; however, at this moment they are the following:

- A track has to be formed with at least 10 hits (from a total of 11 and 12 active layers in the Pixel and SCT barrel and end-cap sections, respectively).
- Poor quality tracks are rejected by imposing a momentum-dependent cut that rejects the upper 5% of the χ^2/NDF distribution in each momentum bin.
- The normalized distance from the perigee of the track to the event vertex is defined as

  $$R_{vtx} = \sqrt{((d_0 - d_{vtx})/\sigma_{d_0})^2 + ((z_0 - z_{vtx})/\sigma_{z_0})^2}$$

  where d_0 is the distance of closest approach to the z axis in the $R\phi$ plane, z_0 the z coordinate of the track perigee, and σ_{d_0} and σ_{z_0} are the errors associated to these track parameters. All tracks have to satisfy a cut of $R_{vtx} < 3$.
- All tracks are extrapolated to the calorimeter, and have to match a tower with signal above a pre-determined threshold.
- The difference in θ and ϕ at the perigee of all track pairs is used to eliminate all but one copy from the sets of tracks that can be generated from signal deposited by a single generated particle; for each pair with $\Delta\theta < 0.005$ and $\Delta\phi < 0.01$ one track is rejected randomly.

The reconstructed tracks that satisfy the above conditions are then matched to the generated particles. The matching can be done by using two methods. The first one makes use of the difference between the pseudorapidity and the azimuthal angle at the perigee of reconstructed tracks and generated particles: a reconstructed track is compared to all generated particles and a match is declared for the pair that has the smallest value of $R = \sqrt{(\Delta\eta)^2 + (\Delta\phi)^2}$ which in turn is required to be smaller than a pre-defined value, i.e. $R < R_{cut}$. A second method matches reconstructed tracks to generated particles using the fraction of hits in the reconstructed track that are common to the generated particle. Each particle generates a set of hits and one hit can have contributions from several particles. The correspondence of a track to a generated particle is made when the track shares 50% of its hits with the particle. This method is used by the developers of the tracking algorithm and is typically used as the standard approach throughout ATLAS. Accordingly, this method provides the working definition of the tracking efficiency used here. Tracks that can not be matched to any of the generated particles, e.g. nearly straight tracks formed from random hit patterns, are then declared as fakes.

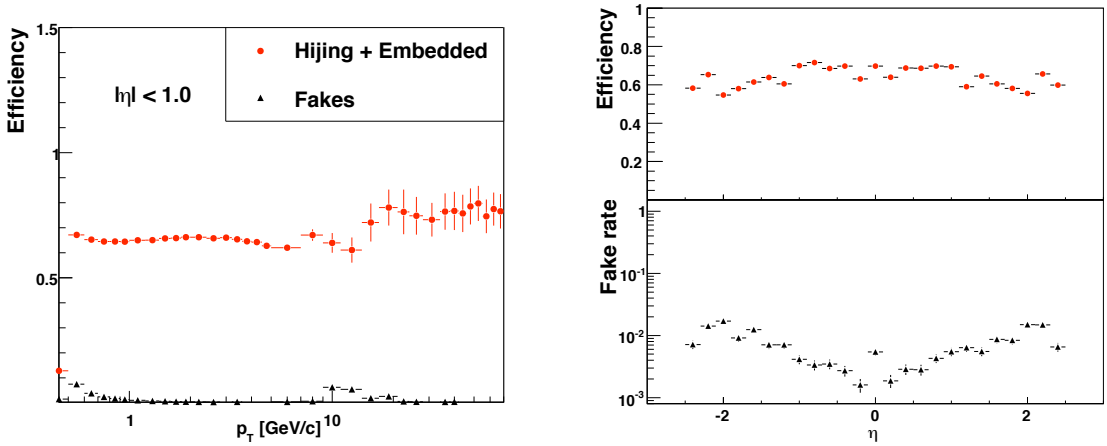

Figure 4.10: (left) Efficiency and fake rate in $|\eta| < 1$ extracted from a sample of central (b=2. fm) HIJING events without quenching in the ATLAS tracking system (right, top) Tracking efficiency as function of pseudorapidity for tracks with $3 \leq p_T \leq 8$ GeV/c extracted from the same events. (right, bottom) Fake rate as function of pseudorapidity for tracks with the same p_T as the top panel.

Within a window in pseudorapidity, the p_T-dependent tracking efficiency is defined as the ratio of the number of matched reconstructed tracks that satisfy all quality cuts divided by the number of generated charged primary particles in the same p_T bin. Primary particles are selected as those with the same z coordinate as the main event vertex. It is also required that the particles do not decay in the detector volume. Note that these studies have been done with a lower limit in the transverse momentum of the generated particles set at 400 MeV/c, since the tracking code has not yet been optimized for lower momenta in heavy ion collisions.

The filled circles in the left panel of Fig. 4.10 show the tracking efficiency in the pseudorapidity window $|\eta| < 1$ extracted from a sample of central Pb+Pb collisions simulated with HIJING without quenching (with $dN_{ch}/d\eta = 2700$). The tracking efficiency for particles with $p_T > 10$ GeV/c was extracted from a special sample of events where ten negative pions, selected from flat distributions in η and p_T, were merged with central HIJING events. The matching of reconstructed tracks with generated particles from this sample of embedded pions was done using the first matching method mentioned above, based on differences in η and ϕ. The filled triangles in the bottom panel of Fig. 4.10 show the rate of fake tracks found in the central sample. The impact of the matching of calorimeter tower information to tracks is most pronounced for tracks with p_T above 15 GeV/$c$where the fake rate falls well below the value of 5%. The tracking efficiency has a weak dependence in pseudorapidity within the full coverage of the inner detector ($|\eta| < 2.5$). The top panel of the right side of Fig. 4.10 shows that the efficiency is 70% near midrapidity, and drops to about 55% at $\eta \sim 2$. The bottom panel of that figure shows the fake rate as function of pseudorapidity for tracks with $3 \leq p_T \leq 8$ GeV/c. The growth of the fake rate with pseudorapidity is present at all values of p_T but it only reaches values that exceed 10% for $p_T \leq 1$ GeV/c.

The spatial resolution of each tracking station is high (16 μm in the SCT), and the detector was designed to have low mass and minimize multiple scattering. The overall momentum res-

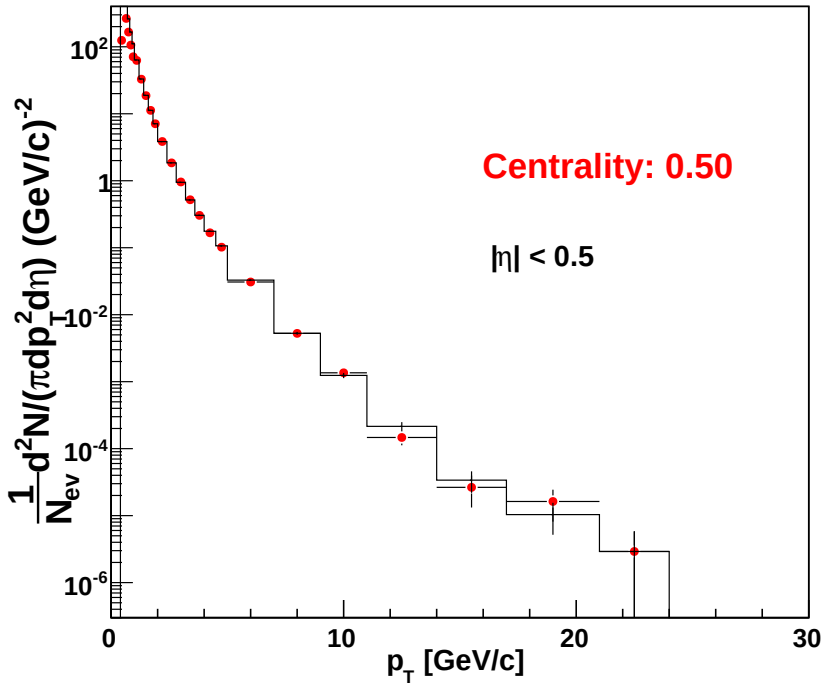

Figure 4.11: Invariant yield for a sample of central HIJING events without quenching ($dN_{ch}/d\eta = 2700$) in $|\eta| < 0.5$.

olution (defined as $\Delta p_T/p_T = |p_T^{rec} - p_T^{gen}|/p_T^{gen}$) has values as low as 2.5% around mid-rapidity for transverse momenta up to 10 GeV/c. This resolution deteriorates slightly at high η where it reaches values of 4% for intermediate $p_T \sim 3$ GeV/c. At high momentum, the design momentum resolution is 30% for 500 GeV/$c$tracks.

The spectrum shown in Fig. 4.11 has been extracted with tracks reconstructed with the Pixel and SCT sub-detectors within a narrow pseudorapidity window ($|\eta| < 0.5$). The same quality cuts used in the definition of the tracking efficiency were imposed on the tracks used to generate this distribution. The yields were then corrected for tracking efficiency to calculate the final spectrum. There is no correction for fake tracks, but their contribution to the measured cross section has been estimated to be on the order of a few percent below 5 GeV/c and can be kept below 10% at 10 GeV/$c$and 1% at 30 GeV/c.

It should be noted that while most of the tracking studies performed for heavy ions so far are for particles with $p_T > 400$ MeV/c, this is not due to limitations of the ATLAS detector itself. The tracker is sufficiently large compared to the bending power of the main 2 T dipole field such that particles below $p_T < 400$ MeV/c leave full tracks in the silicon, as shown in Fig. 4.12. The main limitation in reconstructing the low p_T tracks, at present, is the implementation of the tracking code, which is currently too memory-intensive to handle the high occupancies of heavy ion events. However, this is a situation that is rapidly improving, especially with all of the work taking place

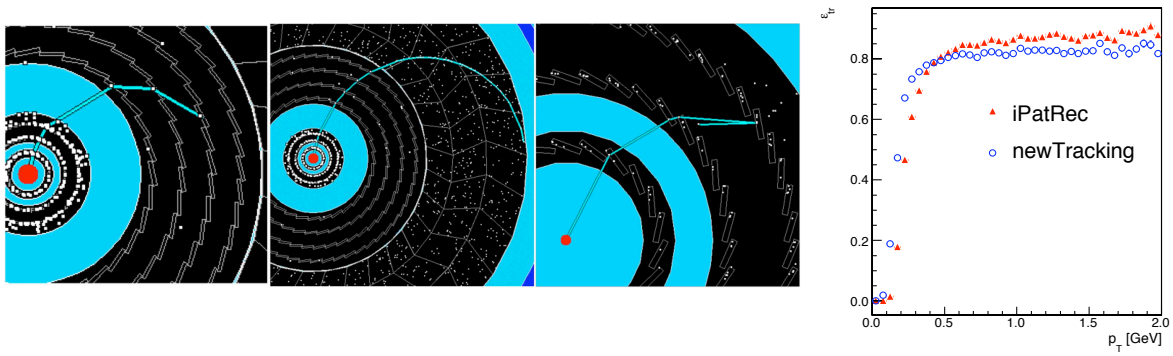

Figure 4.12: (left) Tracks of $p_T = 50, 150$ and 400 MeV/c in the ATLAS spectrometer. (right) Efficiency for particles reconstructed by two standard tracking algorithms in p+p collisions vs p_T, showing reasonable efficiency down to 100 MeV/c.

for the p+p data-taking preparations. The right panel of Fig. 4.12 shows the track finding efficiency for two other ATLAS tracking algorithms (newTracking and iPatRec) run on p+p events[118]. It is observed that reasonable efficiency is found even for tracks down to 100 MeV/c. Development to extend this work to heavy ion collisions is ongoing.

4.8 Summary

- This section has described the ATLAS capabilities for measuring global variables in heavy ion collisions at the LHC.
- These observables are expected to be the very first measured in Pb+Pb (and p+p) collisions and will establish the working environment for the high p_T observables described in earlier sections.
- The large acceptance tracking and calorimeter systems will allow high precision estimations of charged particle and energy density event-by-event.
- They will also provide various ways both to estimate the reaction plane, as well as to measure the elliptic flow signal.
- Combining these measurements, we will quickly establish the bulk properties of the medium produced at the LHC.

Chapter 5

Quarkonia physics

This chapter discusses quarkonia measurements that will be made by ATLAS with a focus on Upsilon measurements that will provide a new tool for studying Debye screening and deconfinement in the quark gluon plasma. The chapter outlines the physics motivation for the measurements, describes the muon detectors, and discusses ATLAS performance, particularly the mass resolution, acceptance, and detection efficiency for measurement of Υ, Υ', Υ'', and (briefly) J/ψ production.

5.1 Physics Motivation

The measurement of quarkonia production in heavy ion collisions provides a powerful tool for studying the properties of hot and dense matter created in such collisions. If this matter is deconfined, color screening prevents various quarkonia states from being formed when the color screening length becomes smaller than the quarkonium size [119]. Since the color screening length is related to the temperature of the matter created in heavy ion collisions, one can use the observation of suppression of different quarkonia states as a thermometer. Thus, it is important to measure simultaneously different quarkonia states, since they are predicted to dissociate at different temperatures [120, 121, 57]. Ref. [57] in particular makes predictions for six separate states based on a potential model fit to lattice data, as shown in Table 5.1:

State	χ_c	ψ'	J/ψ	Υ'	χ_b	Υ
T_{dis}	$\leq T_c$	$\leq T_c$	$1.2T_c$	$1.2T_c$	$1.3T_c$	$2T_c$

Table 5.1: Predictions for quarkonia dissociation temperatures, from Ref. [57]

The suppression of quarkonia due to Debye screening was expected to be the platinum signature of the production of a quark-gluon plasma in relativistic heavy ion collisions. However, the quantitative agreement between J/ψ suppression measured by the NA50 experiment at CERN [122, 123], and the PHENIX collaboration at RHIC [124] cannot currently be understood simply by Debye screening. Recent results from the PHENIX experiment are shown in Fig. 5.1, along with NA50 and NA60 data from SPS. The exact interpretation of both results is still being debated, and information about other quarkonia states is necessary in order to clarify the situation.

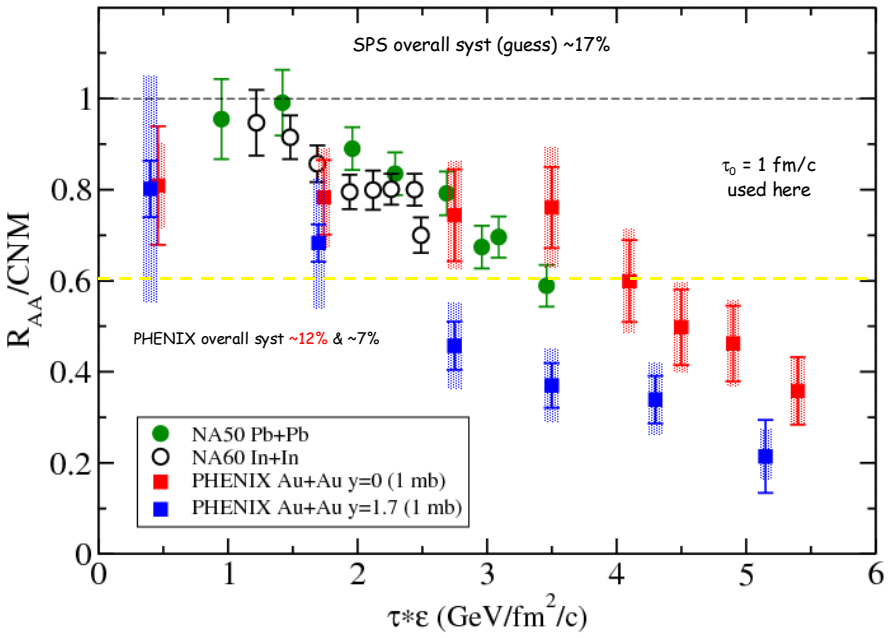

Figure 5.1: J/ψ R_{AA}/CNM vs. $\tau\varepsilon$ in A+A collisions, where CNM is the cold nuclear matter suppression. PHENIX Au+Au measurements for mid (forward) rapidity data are shown with red (blue) squares [124]. NA50 Pb+Pb [125] and NA60 In+In results [126] are shown by green and open black circles, respectively.

At the LHC, the higher collision energy and luminosity will allow the study of the Y family in addition to charmonium. As a result, it will be possible to measure a much wider variety of bottom (b) and charm (c) quarkonia states with different binding energies and thus different expected dissociation temperatures.

The possibility to measure the Y and J/ψ quarkonia families via di-muon decays in heavy ion collisions with the ATLAS experiment has been explored. The simulation results for expected acceptance, reconstruction efficiency, mass resolution, rates and background estimates for Y and J/ψ states in Pb+Pb collisions at LHC will be shown in this section. The present study was done by merging single simulated Y's from flat distributions in transverse momentum (p_T) and pseudo-rapidity (η) with central (impact parameter $b = 2$ fm) Pb+Pb HIJING events. The full reconstruction chain [101] was then run on those merged events, just as for real data. The final histograms were then filled using p_T and η weights taken from minimum bias PYTHIA events.

5.2 ATLAS muon spectrometer

The muon spectrometer forms the outer shell of the ATLAS detector and occupies by far the largest part of its total volume. It is located on the outside of the calorimeter modules and covers the space between approximately 4.5 m and 11 m in radius and up to 7 m in z for the barrel, and 7 m and 23 m in z on both sides of the interaction point for the endcaps, as shown in Fig. 5.2. Muon

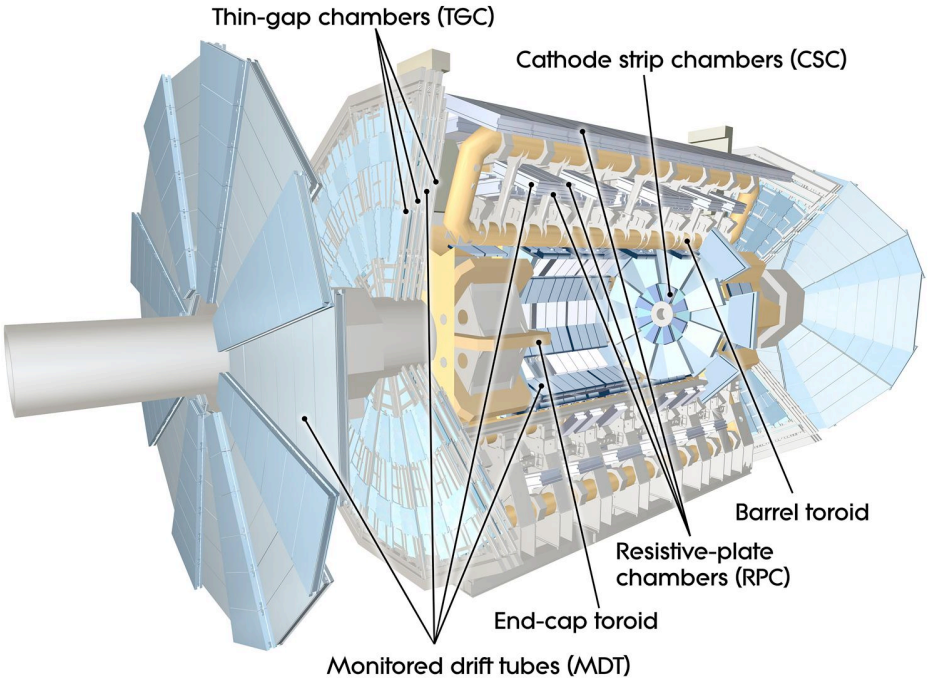

Figure 5.2: 3-D view of the Muon Spectrometer, indicating where the different chamber technologies are used.

momentum measurements are based on the magnetic deflection of muon tracks in a system of three large superconducting air-core toroid magnet arrays.

In the pseudo-rapidity range $|\eta| < 1.0$, magnetic bending is provided by a large barrel toroid magnet (BT), constructed from eight coils surrounding the hadron calorimeter. The magnet creates a toroidal field in air with field values of typically $0.5 - 2$ T. For $1.4 \leq |\eta| \leq 2.7$, muon tracks are bent in two smaller end-cap toroid magnets (ECT), inserted into both ends of the barrel toroid. The BT and ECT coils are rotated in the azimuthal direction by 22.5° with respect to each other. In the interval $1.0 \leq |\eta| \leq 1.4$ referred to as transition region, magnetic deflection is provided by a combination of barrel and end-cap fields. This magnet configuration provides a field that is mostly orthogonal to the muon trajectories, while minimizing the degradation of resolution due to multiple scattering.

Precision track measurements in the Muon Spectrometer is provided by Monitored Drift Tube (MDT) chambers for 99.5% of the solid angle, and Cathode Strip Chambers (CSC) in the forward direction where the particle flux is highest. Triggering is done by Resistive Plate Chambers (RPC) in the barrel region and Thin Gap Chambers (TGC) for the end-caps which together overlap the spectrometer acceptance up to $|\eta| = 2.4$. In the barrel, the muon chambers are arranged in three concentric cylindrical layers ("stations") around the beam axis. The end-cap chambers form four disks on each side of the interaction point, also concentric around the beam axis.

5.3 Υ mass resolution

The di-muon mass resolution is the main parameter to optimize in order to separate the first three Y states which are predicted to dissociate at different temperatures. Since the ATLAS muon spectrometer alone does not provide sufficient mass resolution to separate various Y states (as it is estimated to be $\approx$ 500 MeV), tracks in the muon spectrometer were matched to those in the Inner Detector (using the combined muon reconstruction algorithm). The resulting combined mass resolution is determined mostly by the Inner Detector tracking performance at low p_T, and multiple scattering in the tracker material.

In order to study the Y mass resolution, 50,000 single Y's were generated, simulated, and reconstructed. A sub-sample of these constituting 5,000 Y's were then merged into simulated central ($b = 2$ fm) Pb+Pb HIJING events in order to study how the Y mass resolution ($\Gamma(\Upsilon)$) is affected by the high multiplicity environment of heavy ion collisions. The Y mass resolution in Pb+Pb collisions as a function of Y η and p_T is shown in Fig. 5.3 and Fig. 5.4, respectively. For comparison, on the same plot, we show the mass resolution for single Y's. As one can see, there is no significant deterioration of mass resolution in central Pb+Pb collisions compared to single Y's. The best mass resolution is achieved in the barrel region ($|\eta| < 1$), and is approximately 120 MeV. Figure 5.4 shows that there is essentially no dependence of $\Gamma(\Upsilon)$ on p_T, which can be expected on kinematic grounds, due to the large Y mass.

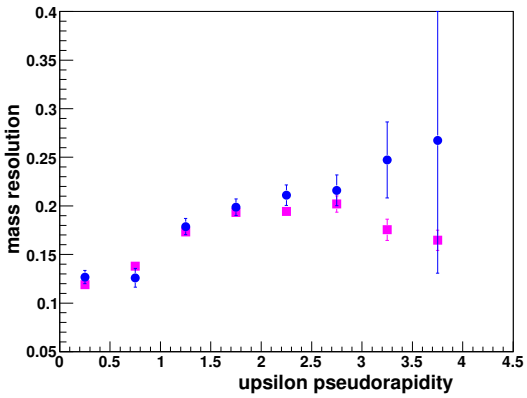

Figure 5.3: Y mass resolution in central Pb+Pb collisions as a function of η (blue circles). For comparison, mass resolution for single Y is shown by magenta squares. Error bars show statistical errors only.

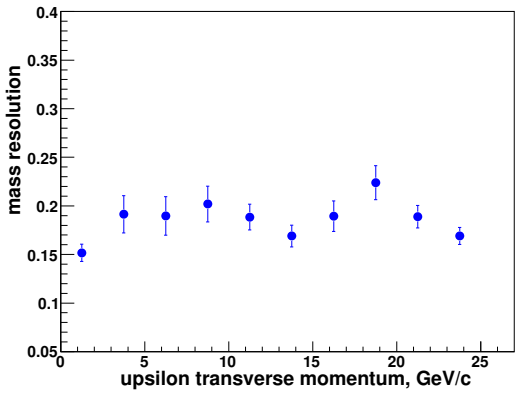

Figure 5.4: Y mass resolution in central Pb+Pb collisions as a function of Y p_T. Error bars show statistical errors only.

The Y mass resolution can be improved by restricting the η acceptance of decay muons, at the cost of reducing the integrated measured Y yield. The Y mass resolution in Pb+Pb collisions is shown in Fig. 5.5 as a function a of cut on the maximum muon η. This plot was made for single Y's to improve statistical accuracy. The best mass resolution for Y's in Pb+Pb minimum-bias collisions using this cut is $\approx$ 110 MeV. The fraction of Y's that satisfy the maximum muon η cut is shown in Fig. 5.6. As one can see, if the muon measurement is limited to the barrel region ($|\eta| < 1$), about 18% off all Y's will satisfy this requirement. Further improvement of the mass resolution is

possible by tightening reconstruction cuts, primarily the χ^2 of the fit between Inner Detector and Muon Spectrometer tracks. However, this will result in a loss of statistics. Depending on what is being optimized, statistics or mass resolution, it is possible to adjust the reconstruction strategy appropriately.

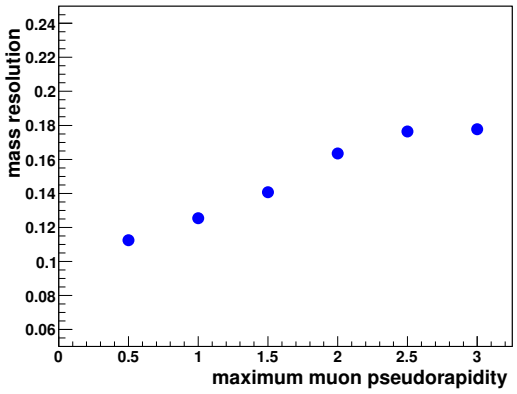

Figure 5.5: Υ mass resolution in Pb+Pb collisions as a function of a cut on the maximum muon η. Error bars show statistical errors only.

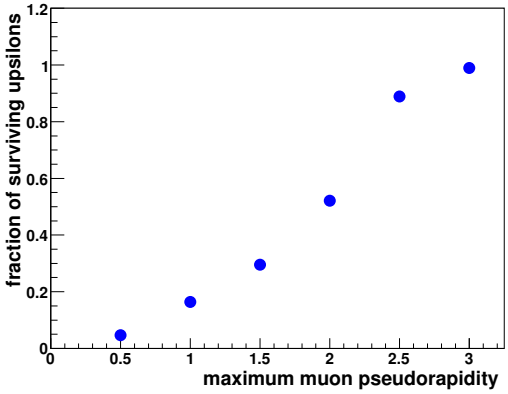

Figure 5.6: Fraction of Υ's that satisfy cut on maximum muon η vs the cut value. Error bars show statistical errors only.

5.4 Υ reconstruction efficiency

Since the reconstruction efficiency for single muons is close to 100% above ≈ 2.5 GeV, the fraction of reconstructed single Υ depends mostly on the geometrical acceptance and the momentum distribution of decay muons. In Pb+Pb collisions this reconstruction efficiency can be degraded by the high multiplicity environment. In order to study the latter effect single Υ's were merged with 5000 central ($b = 2$ fm) and 3000 mid-central ($b = 6$ fm) Pb+Pb HIJING events. 6000 single Υ's merged with PYTHIA p+p events were used as a baseline for this study.

The product of acceptance and reconstruction efficiency, $A\varepsilon$, in central ($b = 2$ fm) Pb+Pb collisions is shown in Figs. 5.7 and 5.8 as a function of η and p_T, respectively. The value of $A\epsilon$ integrated over p_T and η for these events is $10.5\% \pm 0.1\%$. For comparison, $A\epsilon$ integrated over p_T and η in p+p collisions is $12.3\% \pm 0.1\%$. Thus, the efficiency in central Pb+Pb relative to p+p collisions is $\approx 85\%$. In mid-central ($b = 6$ fm) Pb+Pb collisions the integrated $A\varepsilon$ is $10.8\% \pm 0.1\%$.

Figure 5.7 shows that, due to their large mass, Υ's can be reconstructed out to $\eta = 3$. even if this is outside of the nominal spectrometer acceptance of $|\eta| < 2.7$. However, for $\eta > 2$ the Υ acceptance drops quickly, falling below 1% for $\eta > 3.5$. Figure 5.8 shows that there is relatively weak dependence of $A\varepsilon$ on the Υ transverse momentum.

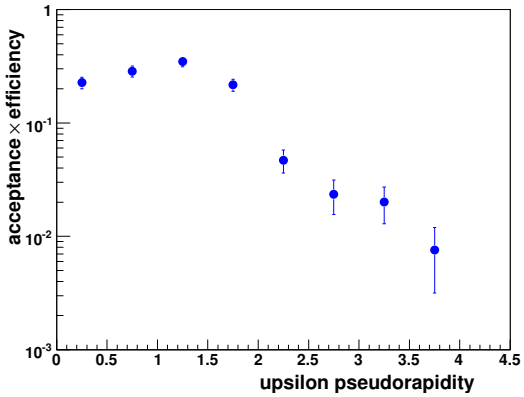

Figure 5.7: Υ acceptance times efficiency as a function of η for central (b=2 fm) Pb+Pb collisions. Error bars show statistical errors only.

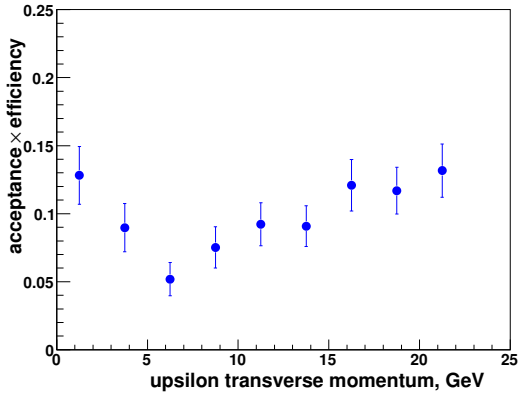

Figure 5.8: Υ acceptance times efficiency as a function of p_T for central (b=2fm) Pb+Pb collisions. Error bars show statistical errors only.

5.5 Expected Υ rates and backgrounds

Backgrounds and expected Υ yields were estimated using PYTHIA. In order to make predictions for Pb+Pb collisions, it is assumed that the number of both high p_T muons and Υ's scales with the number of binary collisions N_{coll}, while the backgrounds are assumed to scale as the square root of the signal yield. The number of binary collisions (N_{coll}) was taken from a Glauber calculation [127]. For minimum bias collisions the predicted value of N_{coll} is 400, while for the 10% most central collisions $N_{coll} = 1670$.

Various sources of background muons include: 1) muons from open charm and beauty decays, 2) muons from hadron in-flight decays before absorption in the calorimeter, and 3) punch-through hadrons which can be reconstructed as muons. The main source of 2) and 3) are pions and kaons.

In order to estimate contributions from heavy quark decays, PYTHIA predictions of decay muon spectral shapes were used, with cross-sections calculated in the CERN Yellow Report on Hard Probes [64]. In order to estimate the contribution from charged light meson decays and punch-through hadrons, single pions and kaons were propagated through the full generation, simulation, and reconstruction chain in Athena. Reconstructed muons from these single π and K events were then used to calculate p_T and η spectra shapes for background muons coming from hadron decays and punch-through hadrons, with multiplicities normalized using cross-sections listed in the Yellow Report. To imitate background in Pb+Pb collisions, all multiplicities were scaled with the number of binary collisions, and then combined with appropriately-scaled Υ's, and run together through the full simulation chain.

The expected di-muon invariant mass distribution as obtained from this Monte-Carlo study is shown in Fig. 5.9. The statistical errors correspond to a conservative 0.25 nb^{-1} integrated Pb+Pb luminosity and a 100% efficient muon trigger. It is observed that the signal-to-background ratio is close to 1. This plot includes acceptance and efficiency corrections and was plotted with muons the barrel region only ($|\eta| < 1$). The average Υ mass resolution in this region is 120 MeV, and $\approx 3k$ Υ are expected to be reconstructed. Total number of reconstructed Υ in the full ATLAS acceptance

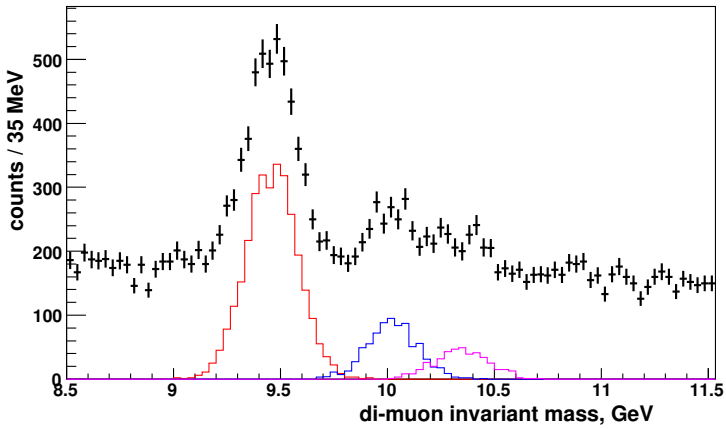

Figure 5.9: Di-muon invariant mass distribution as expected for 0.25 nb^{-1} integrated Pb+Pb luminosity; corrected for acceptance and efficiency; for decay muons in the barrel region only ($|\eta| < 1$). Error bars show statistical errors only. Solid color histograms represent expected yields from the three Y states, and black crosses show the sum of signal and background.

is expected to be $\approx 15k$. As one can see, the Y and Y′ states can be clearly separated. However, the extraction of a separate Y″ yield is more challenging. This is less important from a physics standpoint than separating the Y from Y′ since the Y′ and Y″ are expected to dissociate at similar temperatures.

5.6 Charmonium measurements

In addition to the Y family, it is important to measure charmonium states, in particular the J/ψ and ψ'. This measurement will give us additional valuable information about quarkonia color screening, and will provide a direct connection to lower energy RHIC and SPS data.

The studies of J/ψ acceptance, mass resolution, and background were performed using a previous implementation of the ATLAS offline analysis and GEANT3 and cross-checked with GEANT4 (see [128] for more details). The main problem one faces when measuring J/ψ with the ATLAS detector is the low J/ψ acceptance at low p_T. In order to improve the J/ψ acceptance, two alternative methods of muon reconstruction were considered. The first (standard) method requires a muon to fully traverse the Muon Spectrometer (all 3 muon stations), and only such muon tracks are then associated with the tracks from the Inner Detector. The second method, called the "tagging" method, requires a muon to pass only through the first muon station. If there are still unassociated muon track segments in the first two muon stations after reconstructing all possible muons, the tagging method tries to associate them with the tracks in the Inner Detector. The tagging method degrades slightly the momentum resolution for muons and introduces more background, but it allows the reconstruction of J/ψ down to $p_T \approx 0$ and increases $A\epsilon$ for J/ψ by a factor of 2.9.

The results of an ATLAS study of charmonium measurement are shown in Fig. 5.10 and Fig. 5.11. Figure 5.10 shows the p_T distributions of originally generated ψ's, and the ψ's recon-

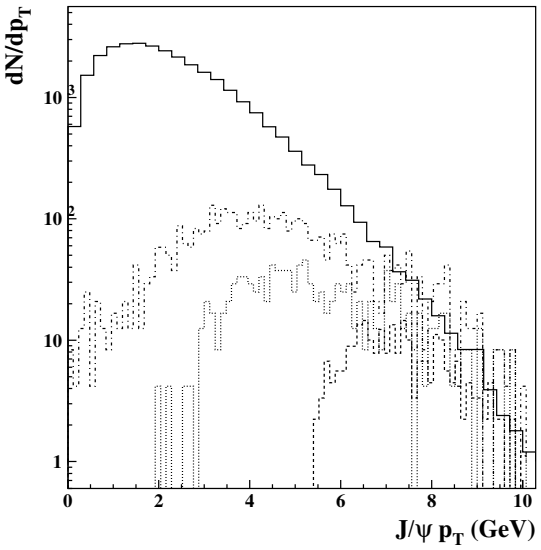

Figure 5.10: J/ψ p_T distribution. Solid line: originally generated distribution; dashed line: full reconstruction with muon $p_T >$ 3GeV ($\times$25); dotted line: full reconstruction with muon $p_T >$ 1.5GeV; dashed-dotted line: "tagging method" reconstruction.

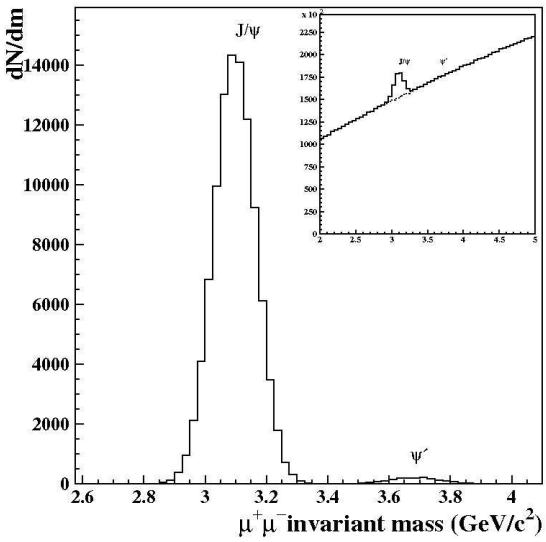

Figure 5.11: J/ψ mass resolution obtained using the "tagging method"; and expected di-muon invariant mass distribution for a single LHC Pb+Pb run (insert).

structed by different methods. Fig. 5.11 shows the expected reconstructed di-muon invariant mass distribution after approximately one month of beam time. The signal-to-background ratio for ψ's is expected to be close to $S/B \approx 0.2$.

5.7 Summary

- Quarkonia dissociation in heavy ion collisions can be studied with the ATLAS detector at LHC for both the charmonium and bottonium family in the di-muon channel. The J/ψ measurement can be done using a specially developed "tagging method", while Y reconstruction can be achieved by the standard (combined) muon reconstruction method.
- The Y reconstruction efficiency in heavy ion collisions is not affected by the high multiplicity environment, and it is the same as that for single Y's even in the most central Pb+Pb collisions.
- The Y mass resolution is good enough to separate Y and Y′ states, at least in the barrel region ($|\eta| < 1$). Separation for Y″ states is less clear, but also possible.
- Backgrounds for both charmonium and bottonium measurements are estimated to be at reasonable levels. The signal-to-background ratio for the Y measurement is expected to be close to 1, and for the J/ψ measurement close to 0.2. It should be possible to observe Y and a J/ψ

peaks after a few weeks of beam time, assuming nominal LHC luminosity for Pb+Pb collisions. It is expected to have $\approx$ 15k Y's and $\approx$ 100kJ/ψ's (using the "tagging method") reconstructed in one month of running in full ATLAS acceptance. Number of Y's reconstructed using barrel region only is expected to be $\approx$ 15k.

Chapter 6

ATLAS Zero Degree Calorimeters

The Zero Degree Calorimeters (ZDCs) have played a crucial role in the heavy ion physics program at RHIC, and we expect the same to be true for the LHC program. The ATLAS Zero Degree Calorimeters are the sole hardware contribution to the ATLAS detector by the US ATLAS Heavy Ion program. At this time, May 2008, the two ATLAS ZDCs, one in each beam direction, have been mechanically assembled and installed in the LHC tunnel. This chapter summarizes the physics role of the ZDCs and provides a brief description of their design and implementation. Further details on the ATLAS ZDC, its design and physics simulation may be found in the original Expression of Interest [129].

6.1 Physics Motivation

The primary motivation for building the ZDCs for the ATLAS Heavy Ion program is to serve both as a high-efficiency, low-background trigger for Pb+Pb events, and as a means to characterize the centrality. The collision centrality reflects the event-by-event change in the impact parameter between the colliding nuclei. As illustrated in the left panel of Fig. 6.1, at a given impact parameter, the participating nucleons reside in the overlap region, while the rest of the nucleons continue forward as "spectators." Central events, with the smallest impact parameters, have the largest number of participants, but yield the fewest spectator neutrons in the far forward region. Peripheral events with large impact parameter yield a far larger number of spectators. This phenomenon is illustrated in the right panel of Fig. 6.1, which shows the strong anti correlation between the ZDC neutron multiplicity and energy observed in the forward hadron calorimeter, from a fast simulation.

The spectator neutrons are also sensitive to the direction of the reaction plane, defined as the plane transverse to the beam direction with the X axis oriented along the impact parameter. This is an important method used alongside the other methods discussed in Chapter 4, but which is in principle independent of other observables[130], and thus minimizes contamination by non-flow. Coordinate readout has been implemented in the PHENIX and STAR ZDCs at RHIC by means of a shower-max detector mounted on its front face. Data from these detectors at RHIC (see e.g. Ref. [131]) has shown that event-by-event energy flow of forward neutrons exhibits "directed flow", or a $\cos(\phi)$ dependence relative to the reaction plane measured by produced particles. It is expected to have similar or better performance at ATLAS since the ZDC has been designed from

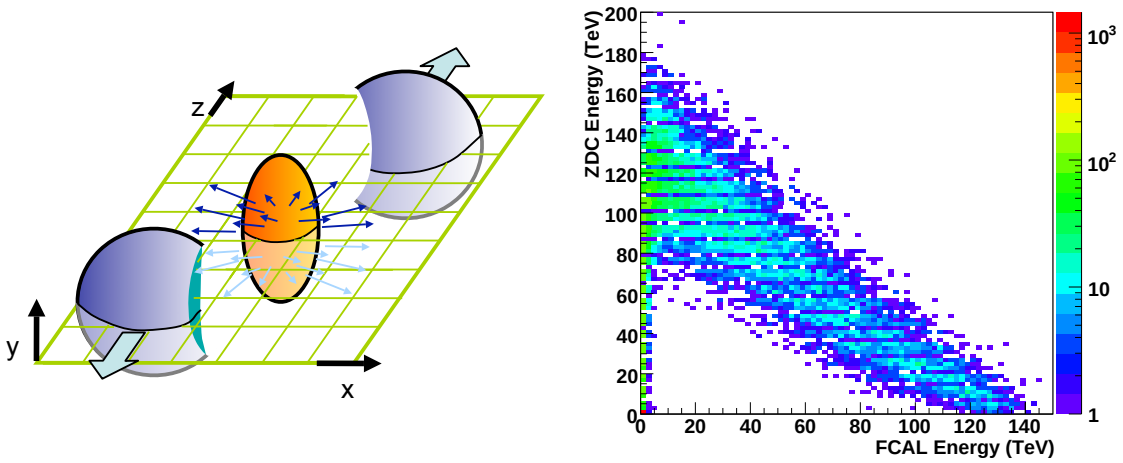

Figure 6.1: (left) Schematic of a nuclear collision, showing the participants in the overlap region and the spectator matter on the sides. The reaction plane is defined as the vector joining the nuclei centers. (right) Correlation of simulated ZDC response with the forward energy emitted into the ATLAS Forward Calorimeters.

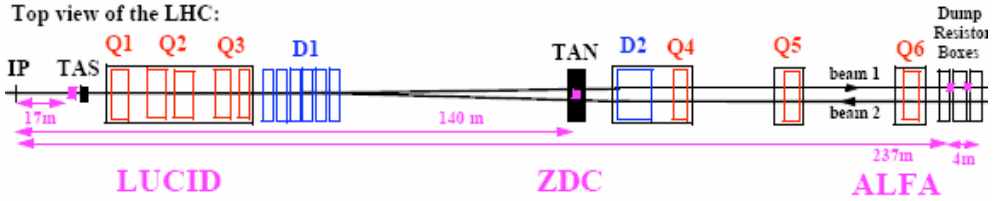

Figure 6.2: Schematic of the ATLAS beam line, showing the position of the ZDC in the far forward region.

the ground-up to provide position sensitivity.

Ultra-peripheral Collisions (UPC), large impact parameter ($b = 25 - 30$ fm) events where the very strong EM fields of the Lorentz-contracted nuclei dissociate one or both of the nuclei, provide an intriguing way to probe the low-x structure of nuclei with real photons, complementary to traditional DIS techniques. The detection of large numbers of forward neutrons in one direction with the ZDC, in tandem with non-detection of the nuclei that emit the high energy photon, is the only known way to trigger on these kind of events. In this way, the ZDC in ATLAS opens up entirely new tools for studying the partonic structure of nuclei.

6.2 ZDC design

In order to only be sensitive to spectator neutrons, the ZDCs are located in the TAN absorbers, 140m in both directions from the nominal interaction point, as shown in Fig. 6.2. The size of the TAN dictates the dimensions of the calorimeter, and thus the detector acceptance, which effectively covers $\eta > 8$.

The ZDC module and detector design is shown in Fig.6.3. The modules consist primarily of a sandwich of tungsten radiator and quartz rods that are used to collect Cherenkov light generated by the electromagnetic and hadronic showers. Each ZDC detector consists of four modules, all of which are similar and have the same intrinsic energy resolution but several have particular capabilities. The three module types are

- **EM X-Y Module** This is the first module which has been provided with X-Y coordinate readout by means of quartz rods which also penetrate the tungsten plates longitudinally allowing the position location of EM showers in an 8x8 grid.
- **Hadronic X-Y Module** This is similar to the EM X-Y Module, but has 24 channels, since the showers will be much wider in this module.
- **Hadronic Standard Module** This module is comprised of quartz rods sandwiched between the tungsten plates. There is no position sensitivity in these modules, which are the rear two modules in each arm, and thus give a single energy measurement per module.

While the energy measurement is essential for event triggering and centrality selection, the position sensitivity of the front two modules provide two additional functions that are well motivated by physics issues in Pb+Pb p+Pb and p+p :

- **Directed Flow:** In heavy ion collisions the transverse coordinate measures the net p_T of the particles hitting the front face of the ZDC. This net p_T is directly related to the directed flow and the reaction plane angle.
- **Neutral Meson Reconstruction:** In p+p and p+Pb interactions, where the detector occupancy is low, the first ZDC module has impressive capability for reconstructing neutral particles which decay electromagnetically near the interaction point (IP)

6.3 Triggering in Pb+Pb

The two main triggers expected for heavy ion running are:

- **Minimum-bias Trigger:** the ZDC minimum-bias trigger is straightforward, requiring a coincidence of energy $E > 0.1 \times E_{beam}/A$ in both arms. The purpose of the trigger is to indicate an inelastic nuclear collision, either via strong or electromagnetic interactions. Similar triggers have been successfully implemented at RHIC, with high efficiency and low fake rate.
- **UPC quarkonia production:** This trigger is based on detecting a J/Ψ or Υ produced in coincidence with a ZDC signal above threshold. In PHENIX, one electron candidate in the central detector was required (corresponding to one J/Ψ decay) in coincidence with one or more ZDC clusters. A similar strategy should be appropriate for ATLAS.

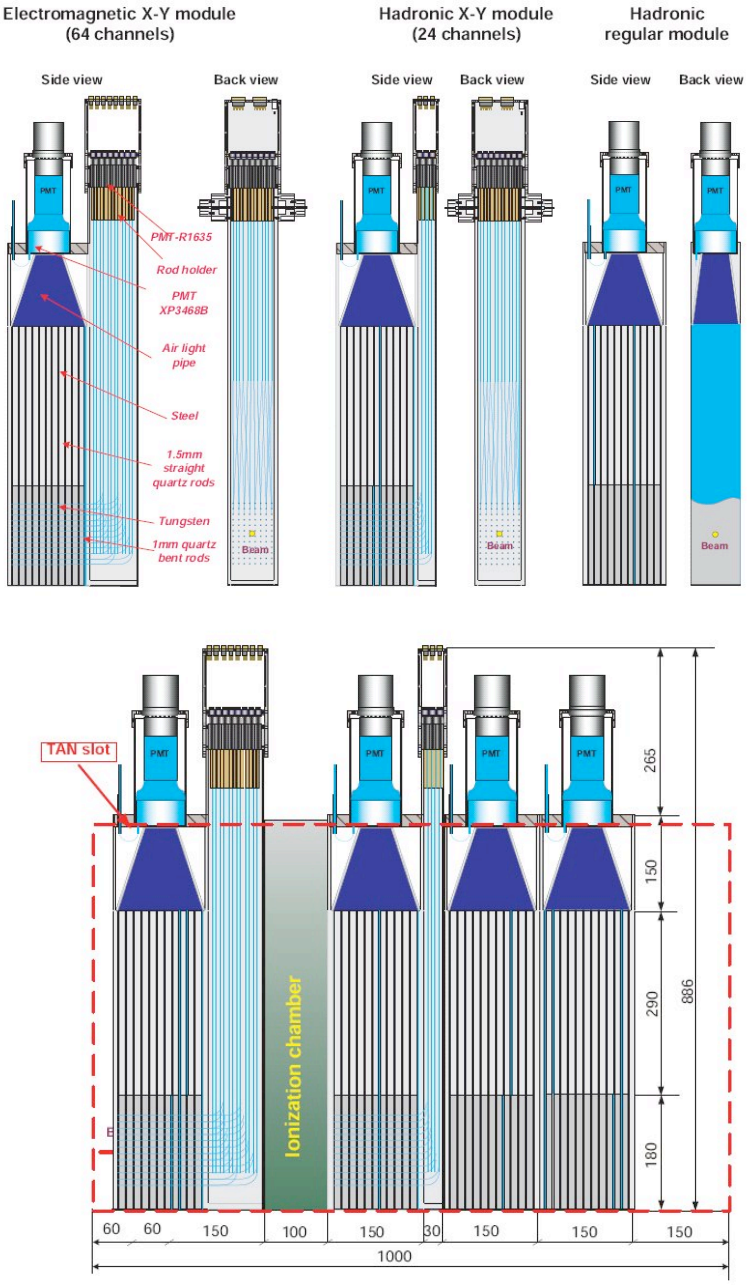

Figure 6.3: (top) ZDC module types and their designs (bottom) ZDC configuration planned for standard running the TAN absorber, from Ref. [129].

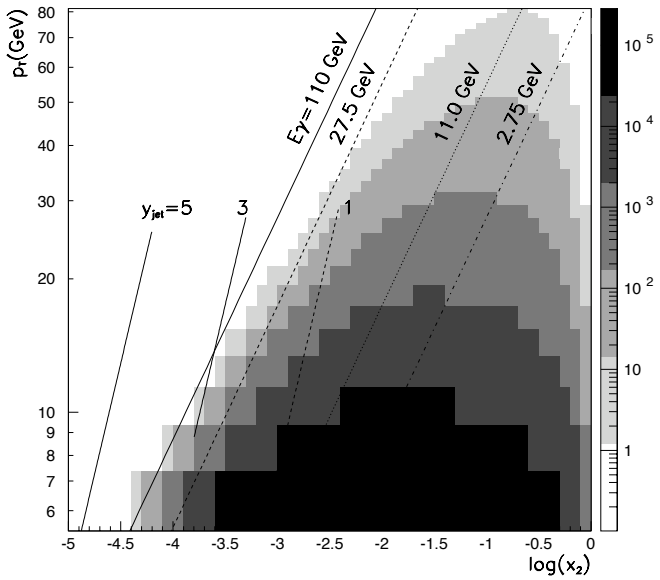

Figure 6.4: Rates of dijet production in ultra-peripheral collisions at the LHC, from Ref. [132].

Of course, trigger development and commissioning is highly contingent on experimental and physics working conditions, and it might be found that the final running conditions to be somewhat different than RHIC. Thus, it is crucial to have the flexible ATLAS multi-level trigger system which can allow the integration of ZDC triggers with other ATLAS triggers.

6.4 Low-x physics in Pb+Pb and p+Pb with UPC

As discussed in Section 6.1 the collision of Pb ions at LHC energies will provide a large sample of ultra-peripheral (UPC) interactions, which are similar to DIS events, but with real photons. These present an opportunity to make measurements of nuclear (in Pb+Pb) and even nucleon (in p+Pb) PDFs at very small x (down to $x = 10^{-6}$), as well as to study diffractive dissociation of nuclei by photons[PS - huh?] This has been discussed in detail in Ref. [132]. Aside from providing important insights into the initial conditions of heavy ion collisions by testing models of the nuclear wave function, e.g. based on the Color Glass Condensate, these measurements are of interest in their own right. Similarly, in p+Pb collisions, the density distribution of partons inside the proton can be measured in a kinematic regime similar to HERA. Ref.[132] includes specific calculations including realistic p+Pb luminosities. An example of this is shown in Fig. 6.4 where rate of jet production in UPC collisions as a function of x and photon p_T for a nominal one month Pb+Pb run.

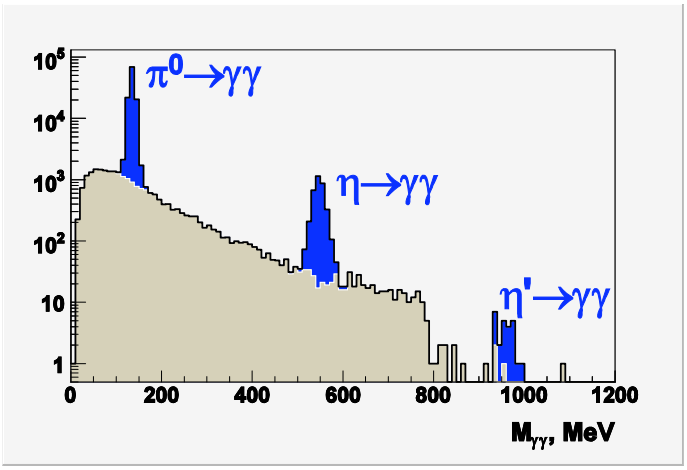

Figure 6.5: Reconstructed neutral meson decays in the ZDC acceptance for p+p collisions at full LHC energy.

6.5 Connections to cosmic ray physics

While the ZDC will of be great use in the p+p program as a luminosity monitor, there are also useful measurements that can be made in minimum bias p+p collisions that are of great interest to the cosmic ray community.

- The forward distribution of neutrons in p+p interactions reflects the event-by-event inelasticity. This is of great importance for Cosmic Ray physicists trying to calibrate HiRes, Agasa and Pierre Auger data for showers above 10^{16} eV using hadronic models. While some data exists on the x_F distribution of neutrons between $0.2 < x_F < 1.0$ at the IRS, and preliminary results are in preparation from PHENIX, this would be a very important measurement at the LHC.
- The x_T and p_T distribution of π^0 and η mesons in the far forward direction also of great interest for model builders of high energy cascades primarily interested in interpreting cosmic ray data. The ATLAS ZDC has a large acceptance in these parameters as shown in Ref. [129] and therefore should provide useful empirical information needed to constrain model parameters. As an example, Fig. 6.5 shows the mass distribution of di-gammas from a sample of 1M PYTHIA events and using a simulation of the full ZDC response.

Considering that the p+p program will get underway in Summer 2008, and possibly several years ahead of the heavy ion program, these topics will be the first major application of the ZDC in ATLAS, and thus essential preparation for the heavy ion program.

6.6 Operations issues

The ZDC is an extremely radiation-hard calorimeter. It has been tested up to $\sim$ 5 GRad absorbed dose and will have an essentially infinite lifetime during the Pb+Pb operation of the LHC. Un-

fortunately the detector is not expected to survive more than a few months of operation at LHC p+p design luminosity. The light attenuation in the optical systems will become significant in the visible wavelengths and as a result the resolution of the device will deteriorate. This is a possible way to operate the ZDC but it will substantially limit the usefulness for a long term heavy ion program. Therefore, once the p+p luminosity of the LHC reaches 10^{33} cm^{-2}s^{-1} the ATLAS ZDC will be removed for high luminosity runs and replaced for heavy ions or for special low luminosity p+p runs. In order to minimize occupational dose to those replacing the ZDCs during these transitions, a remote handling scheme is being designed to eliminate radiation exposure. During high-luminosity stores the ZDCs will be relocated to a shielding enclosure and will be replaced by copper absorber bars in the TAN.

During the first period of 43 bunch operation, the ATLAS ZDC will have its first module replaced by a module from the LHCf detector ($\sim$ 30 cm long). This allows the LHCf experiment to carry out its program during the first few weeks of operation of the machine. When their program is completed, the corresponding ATLAS ZDC module will then be re-inserted and the full program of measurements will continue.

6.7 Summary

The Zero Degree Calorimeters (ZDCs) will play a crucial role in the heavy ion physics program at the LHC.

- The ATLAS Zero Degree Calorimeters (ZDCs) are the main hardware contribution to the ATLAS detector from Brookhaven National Laboratory and the US ATLAS Heavy Ion program.
- The ZDC will provide an event trigger, centrality characterization, reaction plane determination, and UPC capabilities in Pb+Pb collisions
- It also provides unique capabilities for forward neutron and hadron production in p+p collisions, of great interest to cosmic ray physics
- The two ATLAS ZDCs, one in each beam direction, have been mechanically assembled and installed in the LHC tunnel.
- Operations issues are known and being addressed in collaboration with ATLAS management.

Chapter 7

Data acquisition and triggering

The ATLAS data acquisition system is well suited to carrying out the measurements described in this proposal both in terms of readout capability and triggering. This chapter briefly summarizes the design of the ATLAS data acquisition system (DAQ), discusses the conditions under which the DAQ system will operate during Pb+Pb running, and describes the strategy for minimum-bias and rare process triggering during heavy ion data-taking.

7.1 ATLAS data acquisition system

ATLAS has implemented a traditional collider data acquisition system [133] (see diagram in Fig. 7.1) utilizing a three-level trigger system that can, in principle, sample every bunch crossing at 40 MHz while reducing the rate of recorded events to a few hundred Hz, limited by an aggregate data rate of 300 MByte/sec (a number that will be relevant for heavy ion estimates in Chapter 8). Data from all detector channels are sampled and stored in either analog or digital form at the bunch crossing frequency.

The ATLAS Level-1 trigger [134] uses data from the electromagnetic and hadronic calorimeters, the Muon trigger chambers, trigger scintillators, and (for Pb+Pb operation) the ZDC to make a decision to keep or reject data from a bunch crossing within 2.5 μs of crossing. Data from events selected by the Level-1 trigger – up to a maximum rate of 75 kHz – are partially read out and processed by the Level-2 trigger processor farm. Events selected by the Level-2 trigger up to a maximum rate of 1 kHz are completely read out and then subjected to offline style analysis in the ATLAS "Event Filter" farm. Events selected by Event Filter algorithms are transmitted to the ATLAS Tier 0 system for recording and immediate analysis.

During high luminosity (10^{34} cm^{-2}s^{-1}) p+p operation of the LHC there will be ~ 20 minimum-bias p+p collisions per bunch crossing. Under these conditions the total data volume read out from a single crossing is expected to be ~ 1 MByte. The ATLAS DAQ system is designed to have sufficient throughput to read high-luminosity events out to the Event Filter farm at the maximum 1 kHz rate. These performance specifications will be used below to evaluate the DAQ performance under Pb+Pb conditions. The data from the ATLAS calorimeters provides the bulk of the estimated p+p events size as no zero suppression is applied in the calorimeter readout.

The ATLAS Level-2 and Event Filter systems – together referred to as the "High Level Trigger" (HLT) – were designed to find jets, photons, muons, and other desired signatures of interesting

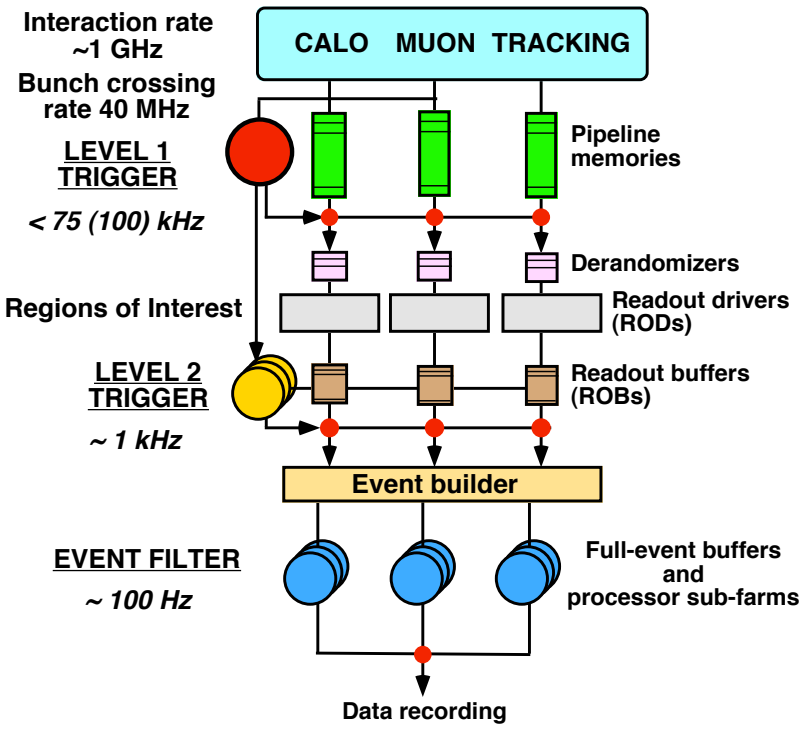

Figure 7.1: Schematic of the ATLAS data acquisition system.

physics in "Regions of Interest" (ROIs) identified by the Level-1 trigger. Each jet, photon, and/or muon candidate satisfying a Level-1 trigger criterion has a corresponding geometrical region that guides subsequent Level-2 and Event Filter analysis that refines the Level-1 trigger decision and ultimately determines whether data from a given crossing are transmitted to the Tier 0 system for archiving. The combination of Level-1 trigger/ROI, Level-2 trigger algorithm, and Event Filter algorithm that select a specific physics pattern are collectively referred to as a "trigger slice."

7.2 Pb+Pb conditions

Based on the maximum anticipated Pb+Pb luminosity of 1×10^{27} cm^{-2}s^{-1} [135] and assuming a Pb+Pb total cross-section of 7.7 b [127], we expect a maximum Pb+Pb hadronic collision rate of 7.7 kHz. This rate is a factor of 10 below the maximum Level-1 trigger rate so the full minimum-bias Pb+Pb rate can be sampled by the Level-2 trigger. Nonetheless, the Level-1 trigger will be used as described below to find jets, photons, and muons at Level-1 to provide regions of interest for Level-2 and Event Filter processing.

We have estimated an average minimum-bias event size of 5 MByte for Pb+Pb collisions using HIJING followed by complete GEANT4 simulations of the detector response (see Chapter 8 for more thorough discussion of event size). The modest increase in event size from p+p to Pb+Pb collisions is largely due to the fact that the calorimeter readout has no zero suppression. The increased event size will reduce the maximum rate at which events can be transferred to the Event

DAQ Stage	Input Rate (Hz)	Max. Output Rate (Hz)	Max. Rejection
Level-1	$< 8 \times 10^3$	75×10^3	none
Level-2	$< 8 \times 10^3$	900	9
Event Filter	900	50	16

Table 7.1:]
Estimated maximum minimum-bias Pb+Pb event rates through different components of the ATLAS DAQ system and resulting upper limits of rejection required in each stage of trigger system

Filter farm. The specification for the ATLAS Event Builder which performs the complete readout of all events selected by the Level-2 trigger is that it should be able to read a aggregate data rate of 4.5 GBytes/s. Based on the above heavy ion event size we estimate a maximum sustained rate of Level-2 accepts of 0.9 kHz during Pb+Pb operation. The specification for the maximum archiving bandwidth from ATLAS is 300 MByte/s. Based on the estimated event size, this gives an archiving rate of approximately 60 events/s.These numbers are summarized in Table 7.1.

7.3 Pb+Pb minimum bias triggers

A well-understood minimum bias trigger is essential to the success of the heavy ion program. The uncertainty in the fraction of total inelastic cross section sampled by this trigger translates directly into an uncertainty on centrality variables (e.g. N_{part}, N_{coll}, or b) which gets significantly worse in more peripheral events. The RHIC program showed clearly that a variety of triggering schemes should be used, with careful offline cuts and various extrapolation techniques, to reduce this uncertainty. Doing this, all of the RHIC experiments kept uncertainties down to a few percent, even with triggers having less than 90% efficiency.

Multiple triggers are available for use as Pb+Pb minimum-bias triggers. The ZDC, described in the previous chapter, will provide a trigger whose efficiency is expected to be better than 90%. The ATLAS Minimum Bias Trigger Scintillators (MBTS) were designed to increase the efficiency for triggering on minimum-bias collisions in p+p collisions. Located at $2.4 < |\eta| < 3.8$, the MBTS has similar coverage as multiplicity/trigger detectors used in RHIC experiments and will provide a Pb+Pb minimum-bias trigger with $\approx 100\%$ efficiency in Pb+Pb collisions. However, the MBTS is not expected to survive beyond early low luminosity runs due to radiation damage. The ATLAS Level-1 trigger has implemented a sum of the total transverse energy, ΣE_T, in the electromagnetic, hadronic, and forward calorimeters. A detailed study of the performance of the ΣE_T trigger including calorimeter suggests that the ΣE_T trigger would have an efficiency of 85% for a noise trigger rate $< 10\%$ of the true Pb+Pb minimum-bias trigger rate.

Beam-gas and halo events and other backgrounds will be removed in the HLT, which has more than sufficient capacity given that it is designed for 75 kHz input rate and the maximum heavy ion rate will be only about 10% of that. Various algorithms involving silicon spacepoints and tracks are being optimized for early p+p running, and we expect to be able to adapt these for heavy ion running. While the large occupancy will challenge these algorithms for more central events, these events are highly unlikely to ever arise from backgrounds, and so a simple threshold on the MBTS total energy should be sufficient to tag them as good events. Conversely, the lower

multiplicities will have a larger background contamination but in these the p+p algorithms should work properly.

7.4 Rare signal triggers

As noted in Section 7.2, no Level-1 trigger rejection is required during Pb+Pb running. However, the Level-2 and Event Filter trigger processing is designed to take advantage of ROIs generated by the Level-1 trigger, so we will use the Level-1 trigger so find jet, photon, and muon ROIs that will provide the starting point for later trigger processing. Because we do not need rejection at Level-1, we can set the relevant thresholds such that there are a up to a few ROIs per event compatible with the typical ROI rate for Level-1 selected p+p events. The rare triggers of interest in Pb+Pb collisions include: jets, high-p_T photons/electrons, single/di-muons and Z's. Each of these triggers depends either on a calorimeter based trigger (jets, photons, electrons) and/or a muon trigger. We describe the Level-1 trigger strategy for each of these separately. Our studies of the performance of Level-2 and Event Filter algorithms on Pb+Pb events are not yet complete, but we expect the efficiency and resolution of the combined Level-2/Event Filter algorithms to be similar to the results presented in Chapters 2-5 as the algorithms are similar to the offline algorithms used in the presented physics studies.

7.5 Pb+Pb jet and photon triggers

7.5.1 Level-1

The ATLAS Level-1 trigger is designed to trigger on jets using an overlapping tiling of trigger towers of size $\Delta\eta \times \Delta\phi = 0.2 \times 0.2$ whose energies are calculated in the calorimeter readout electronics using a combination of analog and digital sums. The Level-1 jet sums are generated for tiles that cover $\Delta\eta \times \Delta\phi$ regions of 0.4×0.4, 0.6×0.6 and 0.8×0.8. The ATLAS jet trigger allows for 8 possible threshold on each of the different tile sizes. Tiles that provide a local maximum E_T and pass at least one of the jet trigger E_T thresholds are candidate Jet ROIs. The ROIs are tagged according to which threshold they satisfy and the list of generated ROIs is available for readout by the Level-2 trigger.

Because of the large backgrounds in heavy ion events, only the 0.4×0.4 tiles will be useful. As noted above, the primary role of the jet Level-1 trigger for heavy ion operation is to provide the ROIs for use in in the HLT. The specification for the Level-2 readout of Level-1 jet trigger ROIs allows a maximum sustained rate of 24 jet ROIs to be read out per event. The lower Pb+Pb Level-1 trigger rate would allow, in principle, a larger number of ROIs per event, but our goal will be to keep the number of ROIs much lower – comparable to the number of expected ROIs per event in p+p collisions – while preserving maximum efficiency for finding ROIs for lower energy jets. We initially set a target of 5 ROIs per event accounting for contributions only from the underlying event; but as will be shown below, this criterion yields thresholds that are unnecessarily low.

The left panel of Figure 7.2 shows the distribution of transverse energy in the the 0.4×0.4 ROIs, $E_T^{4\times4}$, due to the "underlying event" in Pb+Pb collisions for four different centrality bins. Because of the baseline shift in the $E_T^{4\times4}$ energies resulting from the Pb+Pb underlying event, the distribution shifts to larger energies for more central collisions. The right panel of Figure 7.2 shows

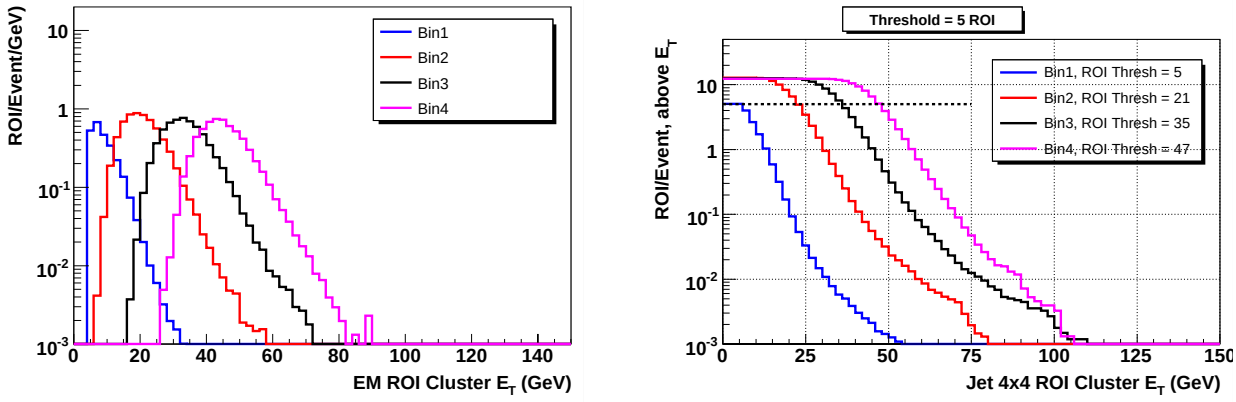

Figure 7.2: Level-1 jet 0.4×0.4 ROI E_T distributions in HIJING simulated Pb+Pb events for four centrality bins, 75-100%, 50-75%, 25-50%, 0-25% indicated as bins 1-4, respectively. *left* - differential ROI E_T distribution, *right* - Integral distribution giving # of ROIs per above a given E_T. The thresholds corresponding to a requirement of no more than 5 ROIs per event are indicated in the legend.

the integral distribution corresponding to Fig. 7.2 expressed in terms of the number of ROIs per events satisfying a given $E_T^{4\times4}$ threshold. A single threshold of 50 GeV would yield no more than a few ROIs per event for all collision centralities. However, such a single threshold would not be ideal because it would produce an inefficiency for jets with $E_T < 50$ GeV in non-central collisions. We indicate in the right panel of Fig. 7.2 $E_T^{4\times4}$ values which give 5 ROIs per event for the four chosen centrality bins. Since the distributions in Figure 7.2 represent only the contribution from the underlying event, real jets will add to the energy in the ROIs. Thus, for events in the 50-75% centrality bin (e.g.) a threshold of 21 GeV will satisfy to requirement of 5 ROIs per event, but that places the threshold only marginally above the most probable value of 20 GeV and only ~ 10 GeV above the low edge of the $E_T^{4\times4}$ distribution in that centrality bin. Thus, such a threshold would nominally correspond to a jet threshold of 10 GeV for ROIs with underlying event E_T on the low side of the $E_T^{4\times4}$ distribution, and essentially zero threshold for ROIs on the high side of the $E_T^{4\times4}$ distribution. Clearly, these numbers are too low to be practical, so in reality we would likely choose thresholds larger by at least 10 GeV which would reduce the number of ROIs per event produced purely by the underlying event) by a factor of 10. This analysis demonstrates that we can choose a set of thresholds that produce an acceptably small number of ROIs per event while also providing the ability to set the effective jet E_T thresholds as low as 10-20 GeV. In practice, we would likely implement eight (8) evenly spaced thresholds varying from 20 GeV to 50 GeV (e.g.) that would allow finer gradations in the association of jet thresholds with centrality.

In addition to the jet regions of interest described above, the ATLAS Level-1 trigger also provides the ability to trigger on photons and τ's using information from the calorimeter. The diagram in Figure 7.3 illustrates the function of the photon trigger. The photon trigger starts with electromagnetic towers of size $\Delta\eta \times \Delta\phi = 0.1 \times 0.1$. The largest energy tower pair within a 0.2×0.2 region with E_T greater than one of eight thresholds, satisfying a cut on the electromagnetic energy in a surrounding "isolation" ring and cut on the total hadronic energy in a 4×4 region including the 2×2 region and the surrounding isolation ring becomes an electromagnetic ROI (EM ROI).

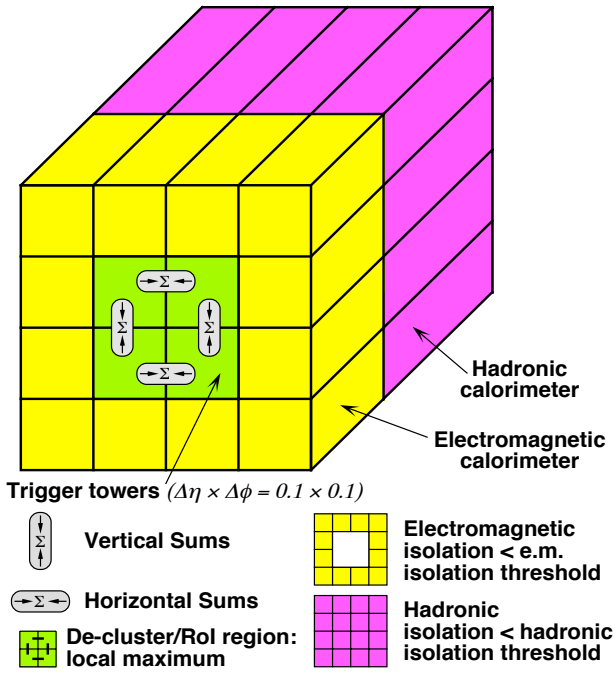

Figure 7.3: Diagram illustrating the Level-1 electromagnetic ROI algorithm

The distribution of EM ROI E_T, E_T^{EM}, values is shown in Fig. 7.4 together with the corresponding integral distribution. Because the EMROIs cover a much smaller $\Delta\eta \times \Delta\phi$ region, the baseline shift is much smaller in the E_T^{EM} distributions compared to the $E_T^{4\times4}$ distributions. A single E_T^{EM} threshold at 20 GeV would be sufficient to trigger on 20 GeV photons (e.g.) over the entire centrality range and would generate < 0.01 EMROI per event.

In fact, we obtain sufficient rejection simply with a cut on E_T^{EM} that we would not need to use the isolation cut at Level-1. By avoiding the isolation cut at Level-1 we avoid having to accommodate the effect of the underlying event in the isolation ring, *and* we can use the Level-1 EM trigger to reduce an inefficiency in the Level-1 jet trigger. Extreme downward fluctuations in the underlying event for a given ROI in a given centrality bin may cause a jet to not satisfy the ROI threshold expected for the given centrality. However, a significant fraction of such jets will have a neutral hadron with sufficient energy that it could be selected by the EM trigger – which is much less sensitive to the fluctuations in the underlying event. The Level-1 calorimeter trigger also implements a "tau" region of interest similar to the EMROI but including the hadronic layers. The ROIs also can be used to improve Level-1 trigger efficiency for jets at low E_T. A first evaluation of the combined performance of the jet 0.4×0.4, EM and Tau ROIs for finding jets in 0-25% Pb+Pb collisions gives an efficiency $> 90\%$ for jet $E_T > 30$ GeV.

Alternatively, if we apply a similar analysis as used for the jet ROIs above with a more restrictive requirement of no more than 3 ROIs per event, we obtain a set of centrality dependent thresholds that are all < 10 GeV and vary by 2 GeV between centrality bins except for the most peripheral bin. For the most central bin where the baseline shift is the largest, the E_T^{EM} value giving 3 ROIs per event is only 3 GeV larger than the most probable E_T^{EM} and is 5 GeV above the low

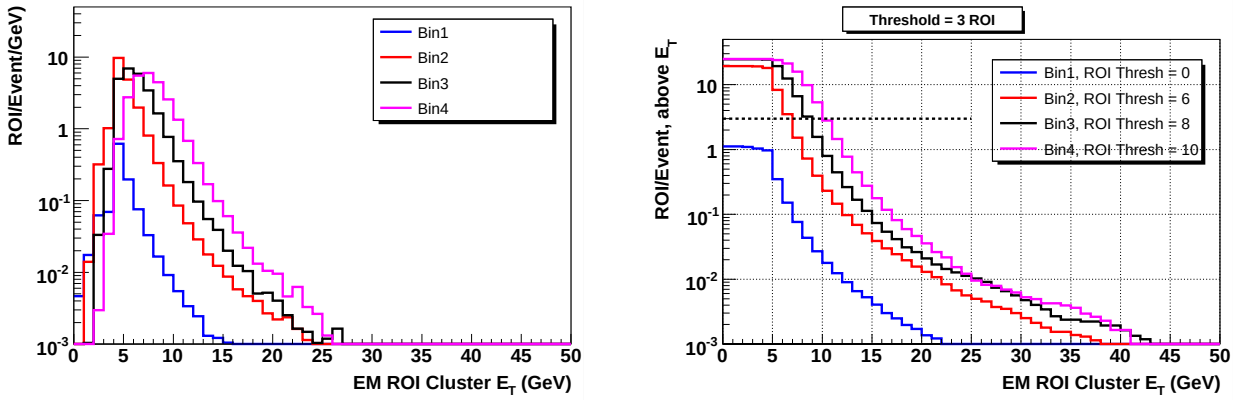

Figure 7.4: Level-1 Electromagnetic ROI E_T distributions in HIJING simulated Pb+Pb events for four centrality bins, 75-100%, 50-75%, 25-50%, 0-25% indicated as bins 1-4, respectively. *left* - differential ROI E_T distribution, *right* - Integral distribution giving # of ROIs per above a given E_T. The thresholds corresponding to a requirement of no more than 3 ROIs per event are indicated in the legend.

edge of the E_T^{EM} distribution. Thus, even for the central events with the most background fluctuations, we could set an effective photon threshold as low as 5 GeV. While we would likely never try to trigger at such a low energy, the ability to push the Level-1 threshold so low means that the Level-1 ROI finding has minimal impact on the final trigger efficiency.

7.5.2 Level-2 and event filter

The Level-2 trigger will provide the first real rejection during Pb+Pb data-taking. The Level-2 trigger has access to all of the data generated by the Level-1 trigger including jet and photon ROIs and the ΣE_T from the calorimeters (see Section 7.3, which allows characterization of Pb+Pb collision centrality. This ΣE_T value will be used to select the jet and photon ROI by evaluating (e.g. with a look-up table) the appropriate thresholds corresponding to the event centrality measured by ΣE_T. Data from the calorimeter corresponding to these regions of interest will be fetched by the Level-2 trigger and used to perform jet and photon reconstruction.

For Pb+Pb collisions, the cone jet reconstruction algorithm will perform a background subtraction based on the ΣE_T value while the k_T algorithm will be used as implemented in the offline analysis (see Section 2.3.2). Since the p+p implementation of the Level-2 trigger uses the full set of calorimeter cells for performing the jet finding, the only additional time spent in the Level-2 jet algorithm for Pb+Pb collisions will be the step of subtracting the estimated background value from the calorimeter cells (for the cone algorithm) and evaluating discriminant quantities to remove false jets. Events selected as satisfying a jet Level-2 trigger will be re-analyzed in the Event Filter using more complete calibrations and corrections and using the same background subtraction procedure as used in the offline analysis. We, therefore, expect the performance of the Event Filter algorithm to be identical to the results shown in Section 2.4.2.

The thresholds that will be applied at Level-2 and in the Event Filter will depend on the actual jet production rates including the effects of shadowing and quenching.and properties of the Pb+Pb

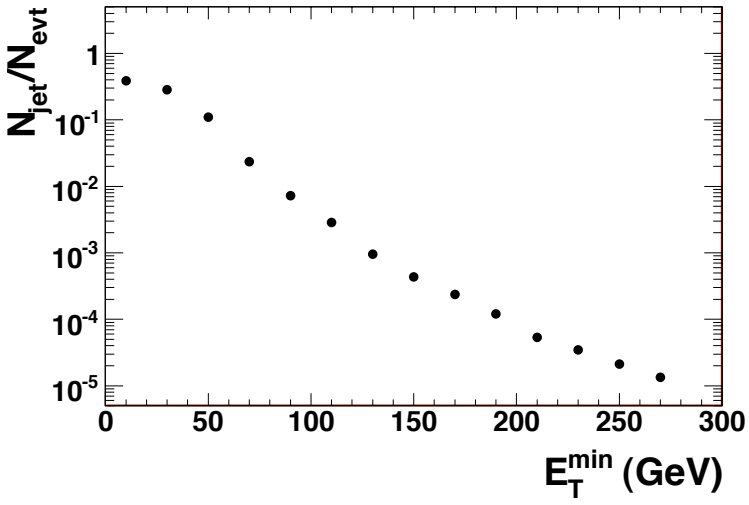

Figure 7.5: Estimated number of jets per event in the ATLAS acceptance above a given E_T in minimum-bias Pb+Pb collisions.(see text for details).

underlying event and also will depend on the fraction of the 50 event/s recording rate allocated to jet triggers. Figure 7.5 shows a plot of the estimated number of jets per event produced in the ATLAS acceptance above a given E_T as a function of E_T assuming no quenching and neglecting shadowing. This result was obtained from the Pythia cross-sections used in Section 2.4.1 scaled by T_{AB}, and integrated over $|\eta| < 5$ and presented as the number of jets per minimum-bias Pb+Pb collision above a given E_T. These numbers are uncertain to at least a factor of two due because of NLO contributions not accounted for by the *k*-factor in PYTHIA, shadowing of nuclear PDFs not included in Pythia, unknown effects of jet quenching (see Fig. 2.6), and other effects. However, Fig. 7.5 shows clearly that the jet rates in Pb+Pb collisions at the LHC will be high, with more than one $E_T > 100$ GeV jet in a thousand Pb+Pb events. If we suppose that 20% of the recording bandwidth is dedicated to jet triggers, at full luminosity a jet E_T threshold of > 100 GeV would be required to reduce the 7.7 kHz minimum-bias rate to 10 Hz. However, at lower luminosities – either during a first LHC Pb+Pb run or later in stores – a trigger as low as 50 GeV could be utilized. In fact, a mixture of jet thresholds will be used with scale downs to collect statistics over the entire E_T range. Nonetheless, all the the practically useful triggers will be well above the low jet ROI thresholds discussed above.

7.5.3 Pb+Pb muon triggers

Muon triggering is provided by Resistive Plate Chambers (RPC) in the barrel region and Thin Gap Chambers (TGC) in the end-caps. The ATLAS Level-1 Muon trigger system is designed to sselect events with single muons passing one or more p_T threshold or events containing two muons passing one or more of the thresholds. In the current off-line implementation of muon trigger emulation, di-muon triggers do not have invariant mass cut; the only requirement is that an event has two muons with p_T above the applied threshold.

The Level-1 muon trigger efficiency was studied using PYTHIA simulated p+p events containing Y's that were merged with minimum bias Pb+Pb HIJING events. The default p+p trigger

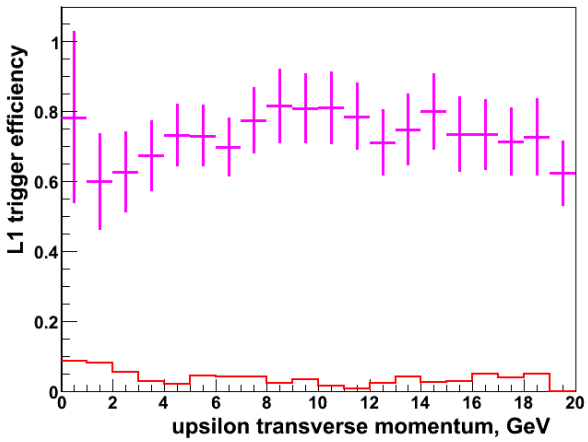

Figure 7.6: Level-1 Υ trigger efficiency as a function of Υ p_T obtained using PYTHIA p+p events with forced Υ production merged into minimum bias Pb+Pb HIJING and using default p+p muon trigger thresholds. Magenta points show single muon trigger efficiency (any Level-1 single muon trigger fired), while red histogram shows di-muon trigger efficiency (two muons passing trigger thresholds). Error bars show statistical errors only.

thresholds were used with the lowest threshold corresponding to $p_T \approx 6$ GeV/c. The trigger efficiency was defined as the number of events in which an Υ was reconstructed and trigger fired, divided by the number of events in which an Υ was reconstructed. The results for the Level-1 efficiency are shown in Fig. 7.6 as a function of Υ p_T. As shown in the figure, the trigger efficiency is rather low, especially if the Υs are required to pass a Level-1 di-muon trigger. However, this low efficiency results primarily from the default muon p_T threshold of 6 GeV/c. Due to the Υ decay kinematics the probability to have both muons with $p_T > 6$ GeV/c is very low.

Since rejection is not needed at Level-1, we will use multiple strategies to achieve higher Υ trigger efficiency. First we can lower the p_T cut on the muons down to a minimum of 3.5 GeV/c. By reducing the cut we will improve the likelihood that both muons are found by the Level-1 trigger allowing a real invariant mass cut on be applied at Level-2. Second, we will accept some rate (yet to be determined) of single muon triggers through to the Event Filter where the full offline muon reconstruction can be performed. Assuming that the rejection provided by the single muon trigger at 6 GeV/c is sufficient to allow all selected events through to the Event Filter, the resulting Υ efficiency would be approximately that of the single muon curve shown in Fig. 7.6. Ultimately, a combination of single and di-muon triggers with a variety of p_T thresholds will be used at Level-1 to seed Level-2 and Event Filter algorithms – similar to the jet and photon trigger schemes described above. The combined performance of the resulting muon trigger slices is underway. We note that the single muons found at Level-1 can also be correlated with jets at Level-2 and in the Event Filter to select heavy flavor jets for archiving.

7.6 Summary

The ATLAS data acquisition and trigger system is well suited to carry out the Pb+Pb measurements described in this proposal. During Pb+Pb operation ATLAS will record roughly 50 Pb+Pb events per second. Multiple triggers can, and will, be used as Pb+Pb minimum-bias triggers, including a ZDC coincidence trigger, a scintillator-based coincidence trigger (MBTS), and a calorimeter ΣE_T threshold trigger. The combination of these triggers is expected to provide a minimum-bias Pb+Pb efficiency $> 95\%$. For rare signals no rejection is needed at Level-1 for all expected Pb+Pb luminosities, but the Level-1 trigger will be used to find "Regions of Interest" that will be used in Level-2 trigger and the Event Filter to select jets, photons, and muons and a fraction of minimum-bias Pb+Pb events for recording. The threshold for the jet and electromagnetic regions of interest can be set low enough to have little or no impact on the trigger efficiency for jets and photons. The Level-2 trigger will use fast versions of offline algorithms to reconstruct jets with background subtraction and find electromagnetic clusters. The Event Filter will run full offline analysis on the regions of interest found by Level-1 and surviving Level-2 cuts. The resulting performance for jet and photon finding in the combined Level-2 and Event Filter systems will be similar to the results presented in Chapters 2 and 3. For Y measurements, the default p+p Level-1 di-muon trigger is found to be inefficient in selecting Ys at Level-1. However, since rejection is not needed at Level-1, a combination of single muon and di-muon triggers with lowered p_T thresholds at Level-1 will seed Level-2 and Event Filter algorithms that can select Ys based on invariant mass cuts and with better efficiency. The Level-1 single muon triggers will also provide the ability to select heavy flavor jets at Level-2 and in the Event Filter.

Chapter 8

Computing needs

This chapter outlines the computing request for the US ATLAS-HI effort, based on a bottom-up estimation of resource needs. These include both computing for reconstruction and analysis of real data, as well as Monte Carlo computing, which is an essential component of the analysis. The overall scale of the yearly costs is a few percent of the expected RCF budget.

8.1 Heavy Ions in the ATLAS Computing Model

According to the ATLAS computing model, Pb+Pb data will be treated the same as all other data used for measurements by the other physics working groups in the collaboration (e.g. top, B-physics, Higgs, etc.). According to this policy, resources are implicitly allocated for Pb+Pb analysis in proportion to data volume, and the computing model estimated that the Pb+Pb data would comprise approximately 10-15% of the total ATLAS data volume. However, in 2007 US ATLAS removed the 10-15% contribution for computing resources that would be applied to heavy ion analysis from the US ATLAS grid. This de-allocation of resources from US ATLAS computing made it necessary that the US ATLAS-HI program find the means to replace the removed processing power and storage in order that the US be an equal contributor to Pb+Pb data analysis, consistent with the role of the US ATLAS-HI participation in the heavy ion physics program.

In several ways, heavy ion events are qualitatively different than p+p events. They are:

- Denser, in that they can require CPU resources that scale non-linearly with particle density if various algorithms are non-linear (e.g. the tracking)
- MC-dependent, in that we need large samples of simulated data, which is itself quite CPU intensive
- Global, in that even rare probes are typically correlated with the "bulk" particle production, thus necessitating relatively few analysis streams

The primary resource for heavy ion running and analysis is the ATLAS grid. However, it is clear from the above considerations that the heavy ion part of the computing requires extra resources to make up for the planned shortfall. Based on a consideration of various options, the most cost effective way to achieve the goals outlined here is to host US ATLAS-HI computing resources at the RHIC Computing Facility (RCF). This section covers ground-up estimates for

Raw size	5	MB	Sim Raw size	70	MB
ESD size	3	MB	Sim ESD size	6	MB
AOD size	1	MB	Sim AOD size	1	MB
TAG size	0.001	MB	Sim TAG size	0.001	MB
DPD size	0.2	MB	Sim DPD size	0.5	MB
			Sim Raw time	12000	kSI2k-sec
Rec time	120	kSI2k-sec	SIM Reco time	300	kSI2k-sec
AOD time	0	kSI2k-sec	SIM AOD time	0	kSI2k-sec
TAG time	0	kSI2k-sec	SIM Tag time	0	kSI2k-sec
Analysis time	10	kSI2k-sec	SIM Analysis time	1	kSI2k-sec

Table 8.1: Assumptions about data size and processing times for real and simulated ATLAS data

computing needs for the US contribution, and what will be needed to support it through FY12. The US ATLAS-HI needs will be compared with RCF plans for growth during FY2008-2011, as outlined in Ref. [136].

8.2 ATLAS file types and resource expectations

In the ATLAS computing model, reconstruction proceeds via several stages, each resulting in a more compact representation of the data:

- RAW - data directly from the detector, stored at Tier 0 (CERN) with a full set copied world-wide to the Tier 1 facilities
- ESD (Event Summary Data) - a "first pass" reconstruction, first generated at Tier 0 and then re-passed twice per year by the Tier 1 cloud
- AOD (Analysis Object Data) - Physics objects for physics analysis, produced with ESD's at Tier 0, but then regenerated later from ESD's, typically at Tier 2
- DPD (Derived Physics Data) - A compact representation of AODs, ideally in ROOT TTree format, to be analyzed at Tier 3 or on personal laptops. This format is currently under development.

Physics analysis is expected to take place using AODs and DPDs, with large scale production done at Tier 2, with some back navigation to ESDs, where more detailed information will be available. The analysis will presumably be run multiple times, potentially in streams, and will generally require on-disk access to ESD and AOD to be run efficiently. These analyses will be large-scale and centrally organized by interaction between the working group and the ATLAS production teams. There will also be on-demand analysis, small scale productions done on DPDs at Tier 3, which might require reprocessing of ESD/AOD to improve calibrations and will also then require substantial on-disk access to ESD/AOD and DPDs.

Table 8.1 is a table of the assumptions we have used for calculations of resource needs. Raw files have been estimated for the ATLAS Computing Model to be 5 MB/event (only a factor of 5

	Units	FY2009	FY2010	FY2011	FY2012
Data taking	Days	5	14	21	21
	ksecs	172	484	726	726
Event Rate	Hz	50	50	50	80
Events	M	8.6	24.1	36.3	58.1
Raw Data	TB	43.2	120.1	181.4	290.3
Nodes	16k/box	13	35	52	83
Fraction of RCF	%	1.6	2.6	3	N/A
ESD/AOD on tape	TB	103	290	435	696

Table 8.2: Assumptions for yearly data taking capabilities, computing needs, and storage resources.

	Units	FY2009	FY2010	FY2011	FY2012
CPU for 20% RAW/ESD/AOD	kSI2k	40	110	165	265
Fraction of RCF total	%	0.3	0.5	0.6	N/A
20% Raw Tape @ RCF	TB	9	24	36	58
20& ESD/AOD Tape	TB	21	58	87	139
Total Tape @ ACF	TB	30	82	123	197
Disk @ ACF	TB	39	109	163	261

Table 8.3: Proposal for US ATLAS-HI contribution to ACF computing based on 20% of total needed resources

larger than estimates for p+p events – mainly since the calorimeter data volume is of essentially fixed size). The combined ESD/AOD size is roughly the same, a total of 4 MB/event. In general, the reconstruction time per heavy ion event is not extremely large, since most of the events have low multiplicities. However, the most central events have tens of thousands of particles simulated, and many secondaries, dramatically increasing the time up to a day per event. Simulated raw files ("Digitized") are much larger both in file size and processing time, both by about a factor of ten, since they carry a substantial amount of truth information about the primary event and those truth particles must be propagated through the detector.

Table 8.2 shows our assumptions for LHC uptime and ATLAS data-taking capabilities, resulting in an increasing amount of data year-over-year, starting with 9M events in 2009 and reaching 60M events by 2012. With the file sizes estimated above, this results in 50TB of data in the first year and 300TB in 2012 – not a large data volume on the scale of the LHC in general, mainly due to the short expected heavy ion runs.

Given the processing estimates, we have found that the total CPU power needed to handle the data would only require a small fraction of the total RCF computing power available that year (1.5-3%), giving a sense of the scale of our data set relative to the rapidly-growing RCF installation.

	Units	FY2009	FY2010	FY2011	FY2012
Events	M	8.2	23	34	56
# Streams	#	2	4	4	4
# Passes	#	3	3	3	3
CPU	kSI2k	26	14	219	350
Disk	TB	9.3	36	66	102

Table 8.4: Assumptions for resources needed for physics analysis.

	Units	FY2009	FY2010	FY2011	FY2012
CPU	kSI2k	65	256	384	231
Disk	TB	48	144	229	363
Tape	TB	29	82	123	197

Table 8.5: Combined CPU, disk and tape needs for reconstruction and physics analysis.

8.3 Proposed US contribution to ATLAS Heavy Ion computing

Based on three considerations:

- The estimates given above for data volume and processing needed
- The US descoping of purchasing by about 10% to remove the Heavy Ion contribution
- BNL handles about 20% of the total ATLAS computing,

We propose that BNL host 20% of the actual needs for heavy ion data processing (as opposed to 20% of the p+p requirements, which turn out to be much larger). This proposal is outlined in Table 8.3.

In addition to reconstruction, it is also important to budget computing resources for physics analysis. Based on the model above, we are assuming a certain number of "streams" with a certain number of passes per stream, with analysis times specified above in Table 8.1. The total needed CPU and disk resources for physics analysis are given in Table 8.4. It is noted that the resource needs are comparable to those requested for the US contribution to reconstruction. The total resource request for heavy ion analysis at RACF for heavy ion reconstruction and physics analysis are shown in Table 8.5.

8.4 Monte Carlo strategy

Heavy ion physics in ATLAS requires substantial statistics to reduce uncertainties on various detector and physics corrections. Even so, it is not necessary to simulate a fixed fraction of the the total data to make progress. Rather, if a substantial sample of simulated events is available, sufficient to hold down statistical errors in the correction factors, no further simulation would be needed. That said, this will require substantial production yearly to deal with the evolving understanding of the detector as well as the simulations themselves.

This suggests a rapid build-up of computing resources in the years leading up to heavy ion data at the LHC, and then a plateau in purchasing. This should allow a steady state production of 750k events per year (which is 1.5% of the expected data), with continual retirement of disk/CPU as for the normal computing farm, with replacements being purchased to maintain overall capacity. However, additional tape will be needed yearly to keep the new simulations, since it is expected to archive all output, especially when it is associated with particular publications.

Estimates for heavy ion computing resources are shown in Table 8.6, assuming a steady ramping-up of MC production starting immediately and reaching 750k events per year in the steady state, and accounting for both new events and reprocessing existing simulations. We have also included resources for the reconstruction of the simulated heavy ion events, which are minor compared with simulation.

Table 8.7 shows the total MC resource needs, summing all of the contributions in the previous table. It should be noted that the long simulation time per event relative to that needed for reconstruction and analysis leads to MC computing requiring substantial CPU power, which is the primary reason that additional computing will be needed for heavy ion physics. Table 8.8 shows the grand total computing resource needs for ATLAS heavy ion work in the US per year. We find that we need around 400 kSI2k for computing in the steady state, which stops increasing by FY10. However, the amount of disk and tape needed per year does increase, due to the increasing total amount of data, and the faster rate of taking it each year. It should be noted that the growth of heavy ion needs are well matched to the growth of RCF resources. In each FY, the total CPU needed is 4-5% of the planned RCF growth for that year. Disk needs are somewhat larger, on the order of 10% of RCF, while tape needs are substantially smaller at about 1-2% of RCF.

8.5 Hosting ATLAS Heavy Ion computing at RCF

In this section we outline a plan for hosting the US share of the heavy ion computing at Brookhaven, at the RHIC computing facility (RCF). The idea is to utilize the extensive infrastructure being built up for the RHIC II programs for STAR and PHENIX, which happen to exist in the same facility as the ATLAS computing facility (ACF) and share a common management structure.

Table 8.9 shows a complete account of the costs for capital purchases and operation CPU, disk and tape at RACF. This includes all overheads and personnel costs known as of late 2007 [137]. These are the numbers assumed in the following estimates, which are shown in detail in Appendix A, but summarized here. Table A.1 shows the yearly costs for CPU, disk and tape for analysis and reconstruction computing according to the capital and operating costs outlined above. It is expected that CPU will be retired regularly, allowing for a smaller number of machines to handle the needed capacity. It is found that the ratio of total costs to capital costs increases monotonically through FY12, reflecting the larger fraction of costs to go into operating and maintenance, relative to purchasing new equipment. At the same time the final costs increase over time, but not dramatically. Table A.2 shows the yearly costs for CPU, disk and tape for Monte Carlo computing according to the capital and operating costs outlined above. In contrast with the reconstruction and analysis computing, the total costs generally decrease in the later years, since it is not expected to substantially grow the computing year after year, but to reach a steady state capacity.

When all of the yearly costs for analysis/reconstruction and Monte Carlo computing are added up, we find the results shown in Table 8.10. Only by FY12 does the yearly cost exceed $250k/year

		Units	FY2007	FY2008	FY2009	FY2010	FY2011	FY2012
	Events	k	50	250	500	750	750	750
Digitized	Size	TB	3.5	17.5	35	52.5	52.5	52.5
	CPU	kSI2k	24	144	288	432	432	432
	% of RCF		1	2	2.4	2	1.6	N/A
Reconstruction	Size	TB	0.3	1.5	3.0	4.5	4.5	4.5
	CPU	kSI2k	0.5	2.4	4.8	7.1	7.1	7.1
	Passes	#	3	3	2	2	2	2
	Size	TB	0.9	4.5	6.0	9.0	9.0	9.0
	CPU	kSI2k	1.43	10.8	14.4	21.6	21.6	21.6
AOD	Size	TB		0.25	0.5	0.75	0.75	0.75

Table 8.6: Estimates for resource needs for Monte Carlo computing for heavy ion events.

	Units	FY2008	FY2009	FY2010	FY2011	FY2012
CPU	kSI2k	155	303	454	454	454
Data volume	TB	22	41	61	61	61
New Data + 50%	TB	22	52	93	113	123
Tape @ T1	TB	22	41	62	62	62

Table 8.7: Yearly request for MC simulation and processing per year

	Units	FY2008	FY2009	FY2010	FY2011	FY2012
Reco CPU	kSI2k		65	256	384	230
Reco Disk	TB		48	144	229	364
Reco Tape	TB		29	82	123	197
MC CPU	kSI2k	155	148	151	0	155
MC Disk	TB	22	30	41	20	10
MC Tape	TB	22	41	62	62	62
Total CPU	kSI2k	155	213	408	384	386
Total Disk	TB	22	78	186	249	374
Total Tape	TB	22	71	145	186	260

Table 8.8: Yearly request for US ATLAS-HI reconstruction/analysis and Monte Carlo computing

Capital Costs	Units	FY2008	FY2009	FY2010	FY2011	FY2012
CPU	$/kSi2k	240	170	110	85	55
Disk	$/TB	700	540	360	270	180
Tape	$/TB	102	102	102	72	72
Operations						
CPU	k$/box	3.0	2.6	3.1	2.9	3.0
Disk	$/TB	280	221	134	93	78
Tape	$/TB	235	235	235	211	211
Capacity/box	kSI2k	16	24	32	48	72

Table 8.9: Cost assumptions by year for RACF, from Ref. [137]

	Units	FY2008	FY2009	FY2010	FY2011	FY2012
Reconstruction/analysis	k$		62	159	214	246
Monte Carlo	k$	68	70	71	42	50
Total	k$	68	132	230	256	296

Table 8.10: Final resource costs per year for US ATLAS-HI

comparable to one of the small RHIC experiments (e.g. PHOBOS). Even in this case, the full request for the heavy ion program, including capital and operations costs, amounts to approximately 4% of the total RCF yearly budget including manpower, a number on the scale of one of the small RHIC experiments during the years before 2006. At the level of capital equipment, the total footprint is typically 4-5% of RCF CPU, 1-2% tape, and 10% disk (the latter being intended to facilitate rapid data analysis). Overall, it is clear that the enormous physics potential of the ATLAS heavy ion program is a great benefit, relative to the modest cost of supporting its computing operations at RCF.

8.6 Summary

- While the ATLAS Computing Model accommodates heavy ion data taking, reconstruction, and analysis, US ATLAS-HI requests additional funds for computing resources to account for the additional reconstruction and MC computing which are expected to be needed for Pb+Pb data.
- Estimates are given for file sizes and processing times, for both actual data and simulated data.
- US ATLAS-HI proposes that BNL provides and hosts 20% of the ATLAS heavy ion data archiving and reconstruction computing estimated in this proposal
- The total cost of US ATLAS-HI computing, including reconstruction, analysis, Monte Carlo, and all manpower and support costs, amounts to approximately 4% (e.g. in FY10) of the yearly RCF budget, including manpower.

Chapter 9

Operations, costs, and management

This chapter describes the management of the US ATLAS-HI program, provides a model for carrying out US ATLAS-HI operations at CERN, and describes the costs associated with the operation of the program. The last part of chapter describes the interaction of the US ATLAS-HI groups with the full ATLAS Heavy Ion working group.

9.1 Management

The management of the US ATLAS-HI program necessarily has to fit within the overall management structure of the ATLAS experiment shown in Fig. 9.1. The ATLAS Heavy Ion working group provides the primary mechanism for participants in the ATLAS heavy ion program to interact with the rest of the ATLAS experiment and with ATLAS management on issues relating to physics, publication, and conference speakers. The conveners of the Heavy Ion working group communicate with and report to the physics coordinators. The physics coordinators subsequently report the physics interests of the heavy ion program to ATLAS management. The ATLAS Heavy Ion Working Group currently has two conveners, B. Wosiek (Krakow) and Cole, the latter being from the US. It is likely that ATLAS will continue to have one of its conveners from the US in the future. Management of data-taking operations in ATLAS falls within the purview of the Run Coordinator. During Pb+Pb operations, members of the heavy ion working group will interact closely with the ATLAS Trigger and Run Coordinator and there will likely be a specific heavy ion liaison to the Run Coordinator who will oversee heavy ion specific aspects of Pb+Pb operations. The institutions participating in the US ATLAS-HI program all have high-energy groups participating in ATLAS and those institutions interact with ATLAS via the Collaboration Board. Ultimately, all ATLAS participants at a given institution, including US ATLAS-HI participants, are represented within ATLAS by the Institutional Representative to the ATLAS collaboration board. Participants in the US ATLAS-HI heavy ion program are, or will be, ATLAS authors and will be subject to the same authorship guidelines as all other ATLAS collaborators. These include a minimum commitment of 50% of a participant's research efforts to ATLAS and a 30% FTE contribution to ATLAS operational support.

High energy groups in the US are organized under the US ATLAS project managed by Columbia University and Brookhaven National Laboratory. For the US ATLAS project, Michael Tuts from Columbia is the Operations Manager and Howard Gordon is the Project Manager through the

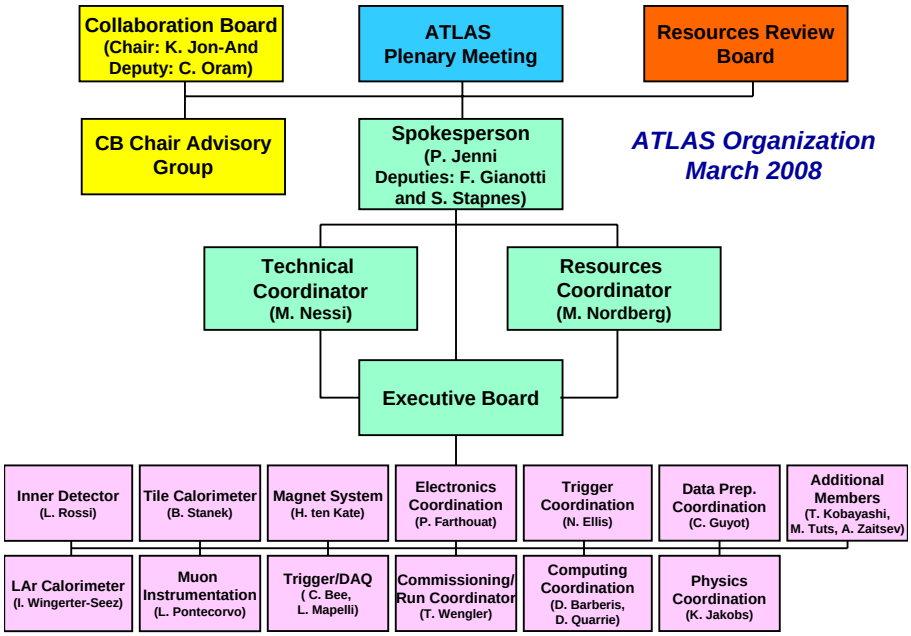

Figure 9.1: ATLAS organizational chart (with names as of March 2008).

completion of the ATLAS construction project and deputy Operations Manager thereafter. A US ATLAS-HI effort would naturally be incorporated into US ATLAS as parallel but closely integrated effort with a separate Operations Manager (Cole) that would report on a regular basis to the Nuclear Science office of the DOE. The US ATLAS-HI operations manager would be responsible for managing the budget for common expenses for the participating institutions, keeping track of US ATLAS-HI participants (especially ensuring that they meet ATLAS authorship requirements), and report to the DOE regarding the expenditures of the US ATLAS-HI program as well as the progress of the program towards achieving its scientific goals. The US ATLAS-HI program manager will work closely with the ATLAS Heavy Ion working group conveners to ensure that the physics goals of the US ATLAS-HI program are appropriately coordinated with non-US groups. Currently, Cole is serving in dual role of US ATLAS-HI Program Manager and ATLAS Heavy Ion working group convener. His convener term will be completed in October 2008.

9.2 Level of effort

Table 9.1 shows the level of effort planned by the participating institutions for the ATLAS heavy ion program. The numbers shown in Table 9.1 are determined both by guidelines from the DOE Nuclear Science Office that an ATLAS heavy ion program must be carried out with re-directed effort, and by the obligations of the participating institutions to the ongoing RHIC program. We repeat here that ATLAS requires authors to devote a minimum of 50% of their research time to

Institution	FY08			FY09			FY10			FY11		
	Phys	Stud	FTEs	Phys	Stud	FTEs	Phys	Stud	FTEs	Phys	Stud	FTEs
Brookhaven	4	0	2.5	4	0	2.5	4	0	2.5	4	0	2.5
Columbia	4	1	2	4	1	2.5	5	2	3	5	2	3.5
Iowa State	2	0	0.7	3	1	1.4	3	1	1.9	3	1	2.0
RBRC	1	0	0.5	1	0	0.5	1	0	0.5	1	0	0.5
Stony Brook	2	0	1	4	1	2.5	4	1	2.5	4	1	2.5
Total	13	1	6.7	16	3	9.4	17	4	10.4	17	4	10.9

Table 9.1: Planned effort on the ATLAS heavy ion program for the current fiscal year (FY08) and for FY09-FY12 for the institutions participating in the ATLAS heavy ion program. "Phys" is the total number of physicists, "Stud" is the total number of Ph.D. students (also included in physicist count), and "FTEs" is the total number of FTEs

Institution	Physics Interests	Hardware	Technical expertise	Other
Brookhaven	Global, photons, jets	ZDC	Simulations, tracking global analysis, photon recon.	pp min. bias
Columbia	Jets, jet frag, photons	ZDC	Simulations, trigger Jet recon.	
Iowa State	Quarkonia, muon tagged jets		Simulations, muon recon.	
RBRC	Jets, photons		Photon analysis	
Stony Brook	Global, Photons, jets		Photon analysis	

Table 9.2: Physics interests, technical expertise, hardware involvement, and other ATLAS contributions of the participating institutions

ATLAS and to contribute 30% of an FTE to ATLAS operations and support. Table 9.2 lists the physics interests, hardware involvement, technical expertise, and other contributions to ATLAS of the participating groups.

9.3 Operations model

Participants in the ATLAS heavy ion program will have to satisfy the ATLAS requirements of 30% of an FTE in support of ATLAS operations. An undetermined fraction of that obligation will be satisfied by support of the ZDC during p+p and Pb+Pb running. While ATLAS has developed formal guidelines for staffing detector operations, monitoring, calibration, and data production shifts, plans are not yet sufficiently specific to determine how the US ATLAS-HI group will participate in ATLAS operations during p+p running. In general, the goal is for the US ATLAS-HI group to contribute to data-taking operations, trigger operations, and monitoring and calibration of the detectors that will be essential for carrying out the heavy ion measurements. As an example, we may contribute to support of the LAr calorimeter since much of the LAr effort is based at Brookhaven, and because it will contribute heavily to ATLAS jet and photon measurements. Additional contributions to data production support at the ATLAS Tier-1 facility at Brookhaven will allow us to take advantage of the geographical proximity of the groups to Brookhaven and to make use of our experience with the Tier-1 facility and especially with the ATLAS software chain.

Following guidance from the US ATLAS project office, we plan to account for half of the ATLAS support obligations (0.15 FTE per collaborator) through work carried out at Brookhaven or at collaborators' home institutions. This work would include remote monitoring of ATLAS operations, calibration and data-production shifts and local detector support. Each ATLAS author from the US ATLAS-HI groups would then need to contribute 0.15 FTE in support for p+p operations at CERN. Using the level of effort described in Table 9.1 this number translates to a continual, rotating presence of two US ATLAS-HI members at CERN.

While a specific schedule for heavy ion running has not yet been established, it is expected that a heavy ion run will typically consist of approximately 2-3 weeks of setup and 3 weeks of Pb+Pb operations. It is thus planned to have a larger CERN presence, at the level of 4-5 physicists from the US ATLAS-HI groups, for a three month period surrounding a Pb+Pb run. The additional time beyond the $\sim 5-6$ weeks of Pb+Pb operations will be spent on preparations for heavy ion running, trigger setup and commissioning, calibrations, and initial Pb+Pb data analysis on output from the Tier-0 reconstruction, which is performed in real time with the data taking.

9.4 Costs

The costs for the US ATLAS-HI program fall into four categories: 1) ZDC construction, 2) computing, 3) travel, and 4) M&O costs. The Zero Degree Calorimeter is the only hardware being contributed to ATLAS specifically for the heavy ion program, although it also has been designed to have applications for the p+p program. The total cost to complete, expenditures prior to FY08, expenditures in FY08, and expenditures anticipated in FY09 for ZDC construction are listed in Table 9.3. These costs are being paid by Brookhaven National Laboratory out of the baseline Nuclear Physics budget.

Category	Cost (k$)
Total construction cost	422
Funds committed	270
Cost to complete	152
Expected FY09 funds	76
Expected FY10 funds	76

Table 9.3: ZDC construction costs and funding profile.

Category	Cost (k$)
2 Bedroom Apartment	50
Airfare (900$ RT)	48
COLA (750$/month)	29
Hostel	21
Transportation	15
Total	164
Total w 25% burden	205

Table 9.4: Breakdown of Travel expenditures for the US ATLAS-HI program based on the assumptions of the operations model in Section 9.3 estimated for FY09.

9.4.1 Travel costs

Estimated costs for travel of US participants to CERN for participation in the ATLAS heavy ion program in FY09 are listed in Table 9.4. These estimates are based on the operations model described above with a rotating, full-time presence of two US ATLAS-HI participants at CERN, 5 participants present at CERN for three months for a yearly heavy ion run starting in FY09, and an additional presence of three US ATLAS-HI participants at 5 ATLAS weeks throughout the year. We assume that the US ATLAS-HI participants would share a two or three bedroom apartment near Geneva and that participants traveling to CERN for p+p operations support and/or Pb+Pb runs would be paid a monthly Cost of Living Allowance (COLA) instead of *Per Diem* at the average level of $750/participant. We anticipate that the US ATLAS-HI group will collectively lease one car from the CERN auto pool primarily to provide transportation for participants living in the apartment. The travel costs for the US ATLAS-HI program can be divided into common costs shared among the participants and institution-specific costs. The common costs would include shared housing and transportation costs and we expect these would be paid via Brookhaven or Columbia. Institution specific costs including airfare, COLA, non-shared housing, and additional insurance for students would be paid directly from the participating institutions grants or contracts.

9.4.2 Computing costs

Chapter 8 provides a complete analysis of the computing needs of the US ATLAS-HI program. Following guidelines from the DOE Nuclear Science Office that no new money would be provided for LHC heavy ion computing, we have developed a plan for meeting the US ATLAS-HI

computing needs via the RHIC computing facility at Brookhaven. Thus, the US ATLAS-HI needs including the replacement of the Brookhaven resources for heavy ion data storage and analysis can be met without new expenditures from the DOE.

If this proposal is supported by the DOE, we expect to be able to augment that computing with additional resources at Columbia University that would add to a Tier-3 system being created by E. Hughes. That system will be supported through a combination of professional staff and physicists. The Columbia US ATLAS-HI participants will contribute to the support of the Columbia Tier-3 system commensurate with the fraction of that system devoted to heavy ion computing. While the Columbia contribution to US ATLAS-HI computing resources is not required, it will provide additional resources for end-stage analysis for all US ATLAS-HI participants and reduce the demand on RCF resources.

9.4.3 M&O costs

In 2007 ATLAS changed its formula for calculating Category A and category B participation costs and implemented a scheme where different countries would be charged different participation costs. According to this formula, the category A and B costs are levied on a per-head basis for all Ph.D. authors in ATLAS. In calendar year 2008 the combined category A&B costs assessed by ATLAS amounted to 15.6 kCHF. We have assumed a 15% growth in the assessed M&O costs per year for future calendar years. Recent variations in currency valuations make the translation of costs in CHF to US$ uncertain. An average of the CHF/$ conversion rate from the period April 1, 2007 to April 1, 2008 [138] gives a value of 1.15 CHF/$. However, the lowest value obtained during that time was 0.96. We have estimated the future conversion rate to be 1.1 CHF/$ and have accounted for future reductions in the value of the dollar in the contingency estimate. The ATLAS Resources Board has suggested that US ATLAS-HI participants can pay M&O costs for a given calendar year at the start of the following fiscal year. This would mean that US ATLAS-HI participants could be ATLAS authors for CY 2009 while paying M&O costs at the start of FY10. We have adopted this model and show in Table 9.5 estimated M&O costs to be paid in fiscal years 2010-2012. We have added a 25% contingency to the M&O estimates to account for uncertainties in the CHF/$ rate and in the growth in assessed M&O costs per year.

9.4.4 Combined costs

Table 9.6 lists the total costs of the US ATLAS-HI program for fiscal years 2009 through 2012 including ZDC construction, computing, travel, and M&O. The funds for ZDC construction and computing will be provided out of existing resources at Brookhaven. The additional expenditures needed to cover travel and M&O costs are shown in the bottom line of the table. These costs are determined by the level of effort described in Section 9.2, the operational model described in Section 9.3, and travel and M&O costs described in Sections 9.4.1 and Section 9.4.3, respectively. The travel and M&O costs include contingency for currency variations and yearly increases to account for growth in ATLAS operational expenses and/or inflation.

FY	M&O/Ph.D (kCHF)	Est. CHF/$	M&O/Ph.D (k$)	# Ph.D Auth.	M&O (k$)	Conting. (k$)	M&O Total (k$)
2010	17.3	0.9	15.6	13	202	50	252
2011	19.9	0.9	17.9	13	233	58	291
2012	22.9	0.9	20.6	13	307	77	385

Table 9.5: M&O costs for US ATLAS-HI program for FY2010-FY2012, under the model described in the text which allows for US ATLAS-HI participants to be authors starting in CY2009.

Category	FY09	FY10	FY11	FY12
M&O	0	252	291	385
Travel	205	220	236	254
Computing	62	159	214	246
ZDC construction	76	76	0	0
Total	348	707	741	885
new expenditures	**205**	**472**	**527**	**639**

Table 9.6: Total estimated costs in k$ for the US ATLAS-HI program for fiscal years FY09 through FY12 based on information provided in other sections of this chapter. Also shown in the "new expenditures" row are new expeditures required from the DOE.

Institution	City	Country	Physics interests
Charles University	Prague	Czech Republic	Jets
University of Geneva	Geneva	Switzerland	Quarkonia
JINR	Dubna	Russia	Z production, Z-jet, Ultra-peripheral collisions
IFJ PAN	Krakow	Poland	Global observables, elliptic flow
MePHI	Moscow	Russia	Ultra-peripheral collision, quarkonia
Pontifica Universidad Catolica	Santiago	Chile	Quarkonia
Santa Maria University	Valparaiso	Chile	Jets, heavy flavor
Weizmann Institute	Rehovot	Israel	Global observables

Table 9.7: Non-US institutions participating in the ATLAS heavy ion with expressed physics interests of participants.

9.5 Non-US ATLAS Heavy Ion institutions

Table 9.7 lists institutions from outside the United States participating in the ATLAS heavy ion program, along with their physics interests. Prior to CY2008. the total effort contributed by non-US institutions to the ATLAS heavy ion effort was comparable to the US effort. However, the non-US effort is growing as the start of LHC operation approaches. As a demonstration of this fact, within the last 6 months, three new institutions: the Weizmann Institute, Santa Maria University, and the University of Sao Paolo have joined the ATLAS heavy ion program.

Chapter 10

Summary

This chapter summarizes the physics case for a US ATLAS-HI program based on the material presented in the remainder of this proposal. It starts with a re-statement of the physics goals of the program and outlines the unique contributions ATLAS will make to the measurement of jets and prompt photons. It then summarizes the physics performance results presented in previous chapters and shows some specific examples of the impact of these performance results on proposed measurements. The chapter concludes with a summary of programmatic and practical reasons for the proposing institutions to participate in an ATLAS Heavy Ion program.

10.1 Goals and plan

The primary physics goals of the US ATLAS-HI program outlined in the introduction and described in this proposal are

- Carry out "day-1" measurements of global observables such as $dN_{ch}/d\eta$, $dE_T/d\eta$, $v_2(p_T, \eta)$ as a function of centrality.
- Carry out quantitative, tomographic measurements of the properties of QGP created in heavy ion collisions at the LHC using complete jets, measurements of jet fragmentation observables, photon-jet pairs, and tagged heavy quarks.
- Probe the response of the medium to the passage of energetic jets with large-acceptance studies of $d^2E_T/d\eta\, d\Delta\phi$ and $d^3N/d\eta\, dp_T\, d\Delta\phi$ in events containing high-energy jets.
- Probe Debye screening in the QGP via measurements of Y decays to di-muons.
- Use a future p+A program to study semi-hard and hard processes at low-x to constrain nuclear shadowing and test models of parton saturation.

This program focuses on the use of hard probes to study the properties of the QGP created in heavy ion collisions at the LHC. It necessarily includes the global measurements that will be essential for constraining theoretical interpretations of the jet and quarkonia measurements. The proposed program also takes full advantage of the strengths of the ATLAS detector, namely:

- Large acceptance, electromagnetic and hadronic calorimeters.

- Fine transverse segmentation and three-fold longitudinal segmentation of electromagnetic calorimeters.
- Large-acceptance silicon tracking with 3 pixel layers and 8-9 silicon strip measurements.
- Large-acceptance muon spectrometers.

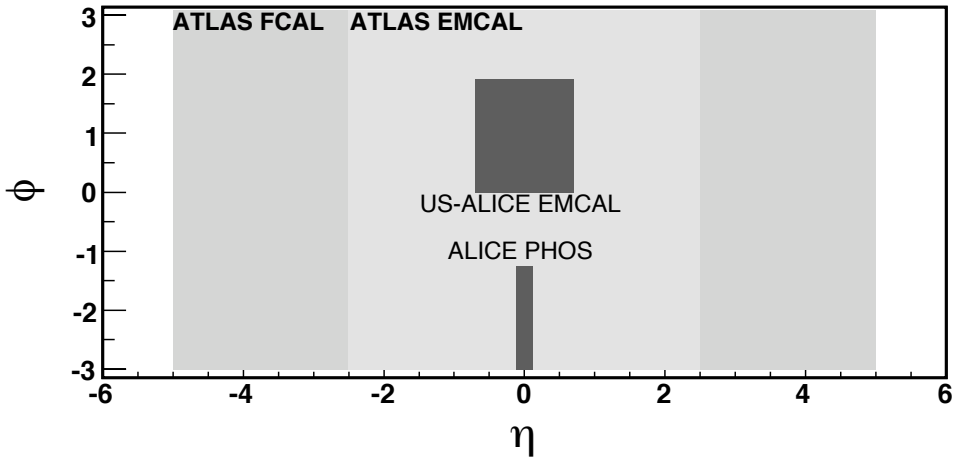

Figure 10.1: Comparison of acceptance for γ-jet physics between ATLAS and ALICE; CMS acceptance is comparable to ATLAS.

The benefits of the extensive ATLAS calorimetry are demonstrated in Fig. 10.1 comparing the ATLAS calorimeter acceptance to the acceptance of ALICE calorimetry. The jet measurements benefit from the ten units of pseudo-rapidity coverage and from the longitudinal and transverse segmentation of the electromagnetic (EM) calorimeter. The ATLAS calorimeters are not compensating calorimeters (which is the case for all calorimetry at the LHC), but the longitudinal segmentation of the ATLAS EM calorimeter and the ability to cleanly identify electromagnetic showers in the first sampling layer of the EM calorimeter improves the offline compensation and gives ATLAS the best p+p jet energy resolution at the LHC The longitudinal segmentation and the fine granularity of the first sampling layer of the ATLAS EM calorimeter also provide valuable systematic control over the jet energy scale when subtracting energy from the underlying event in Pb+Pb collisions.

The value of the ATLAS EM calorimeter system is most evident in photon measurements where the first sampling layer provides significant rejection against neutral hadron decays without the use of isolation. Chapter 3 shows that with tight cuts on shower shape and detection of second peaks in the first EM sampling layer, we can obtain a factor of 3–5 relative [1] rejection against hadrons over the statistically accessible E_T range. Thus, even without the use of isolation we can perform a precision statistical analysis of inclusive photon production and photon-jet

[1] hadron rejection times photon efficiency

correlations with a high-statistics measurement of the decay photon spectrum (see below) and decay photon-jet correlations. The ability to reject hadron decays will also allow measurement of fragmentation/bremsstrahlung photons in jets. The importance of this measurement can not be overstated – it would provide the first direct observation of the radiation from medium-induced bremsstrahlung processes. The transverse (to the jet) momentum spectrum of those photons will provide direct sensitivity to the interaction of the parent quark or gluon in the QGP.

10.2 Summary of performance studies

We have shown in Chapters 2-5 results of physics studies that demonstrate the capabilities of the ATLAS experiment to carry out these measurements. The studies of jets, photons, and quarkonia were carried out with full HIJING simulations through GEANT4 with no limitation on hard processes in the underlying HIJING event. Thus, the performance results shown include the degradation that will result from fluctuations in the underlying event due to mini-jets, true hard jets, charm and bottom production, and hadronic resonances. These fluctuations will likely be overestimated since HIJING was run without quenching and because the two-component (soft and hard) model in HIJING is thought to over-estimate the rate of semi-hard processes. The rates for jet production in Pb+Pb collisions is sufficiently high that the overlap of jets will contribute to a degradation of the jet reconstruction. These effects have typically not been included in previous studies of heavy ion jet reconstruction at the LHC [139].

The studies shown in Chapter 2 demonstrate that ATLAS has the ability to reconstruct full jets with at least two different algorithms over a wide range of transverse energies, with a reconstruction efficiency above 50 GeV that is centrality independent. We show that the reconstructed jet energy spectrum well reproduces the shape of the input spectrum above 80 GeV for all collision centralities prior to correction for jet efficiency and resolution. Figure 10.2 shows the ratio of the uncorrected, reconstructed jet spectrum to input spectrum for $b = 2, 6, 10$ fm Pb+Pb collisions repeated from Chapter 2. The ratio is approximately constant at high p_T at a value determined primarily by the jet energy resolution. This figure shows that, even without correcting for reconstruction efficiency and resolution, we can measure jet R_{AA} with a systematic error of 15% in a background that consists of the full underlying jet and mini-jet spectrum from HIJING. This worst-case systematic error should be compared with the prediction by Lokhtin *et al.* [67] of a factor of two ($R_{AA} = 0.5$) suppression of the jet spectrum in central Pb+Pb collisions, primarily due to collisional energy loss [68]. With even imperfect corrections for jet energy resolution and reconstruction efficiency we expect to be able to reduce the uncertainty on jet R_{AA} to better than 5% above 80 GeV. We have shown (see Fig. 10.3 repeated here) that even before correcting for jet energy resolution we can accurately reproduce jet charged particle fragmentation functions and j_T distributions which provide direct sensitivity to radiative energy loss. ATLAS will measure di-jet pairs with good acceptance$\times$efficiency. The di-jet $\Delta\phi$ distribution should provide direct sensitivity to medium-induced jet angular broadening – a crucial independent probe of parton interactions in the medium that has not, yet, been observed at RHIC.

We demonstrated in Section 2.7 that ATLAS can tag heavy flavor jets with semi-leptonic decay muons. This analysis requires correction for in-flight decays of light hadrons and punch-through hadrons identified as muons in the muon spectrometer. However, those corrections are modest ($\sim$ 33%) and can be reduced with cuts on the muon p_T and angle. Separate tagging of jets with

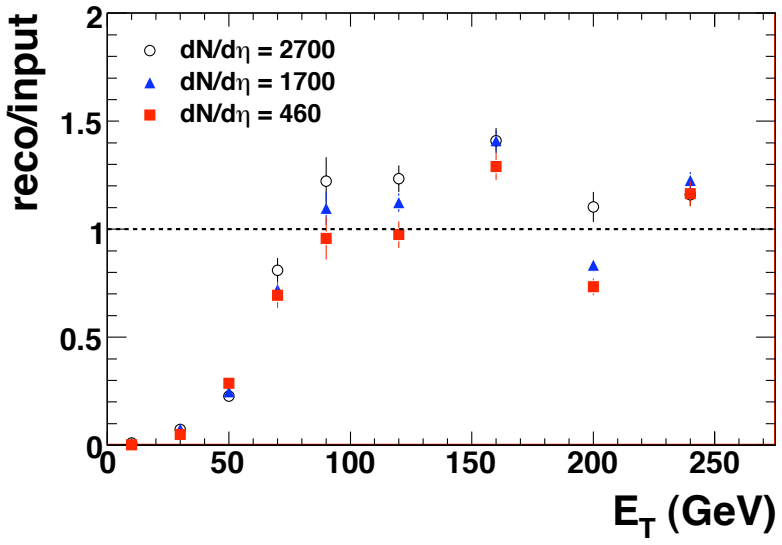

Figure 10.2: Ratio of reconstructed to input jet spectrum for three different collision centralities without efficiency and resolution corrections to the reconstructed spectra.

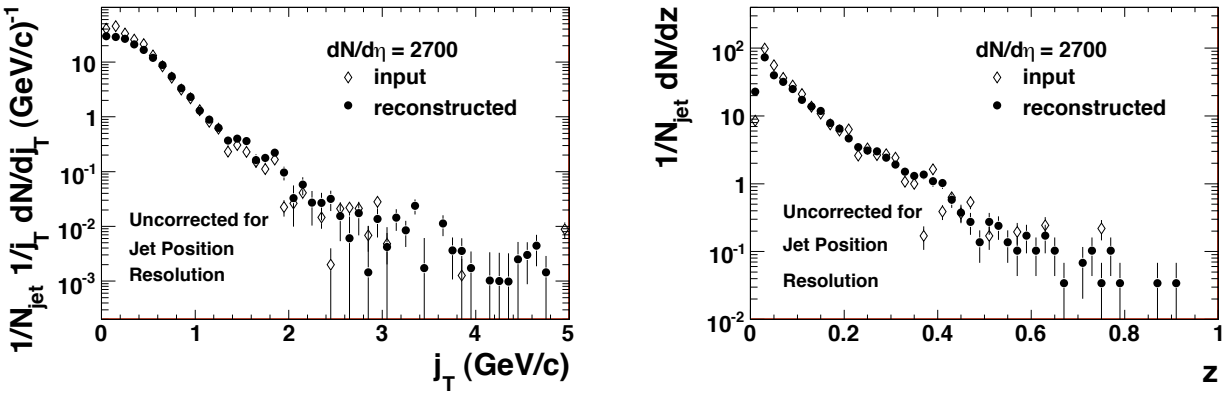

Figure 10.3: Comparison of PYTHIA simulated and reconstructed fragmentation functions and j_T distributions for di-jet events embedded into central ($dN_{ch}/d\eta = 2700$) HIJING Pb+Pb events. The reconstructed distributions have not been corrected for efficiency and resolution, in order to show the maximal distortion of the distributions.

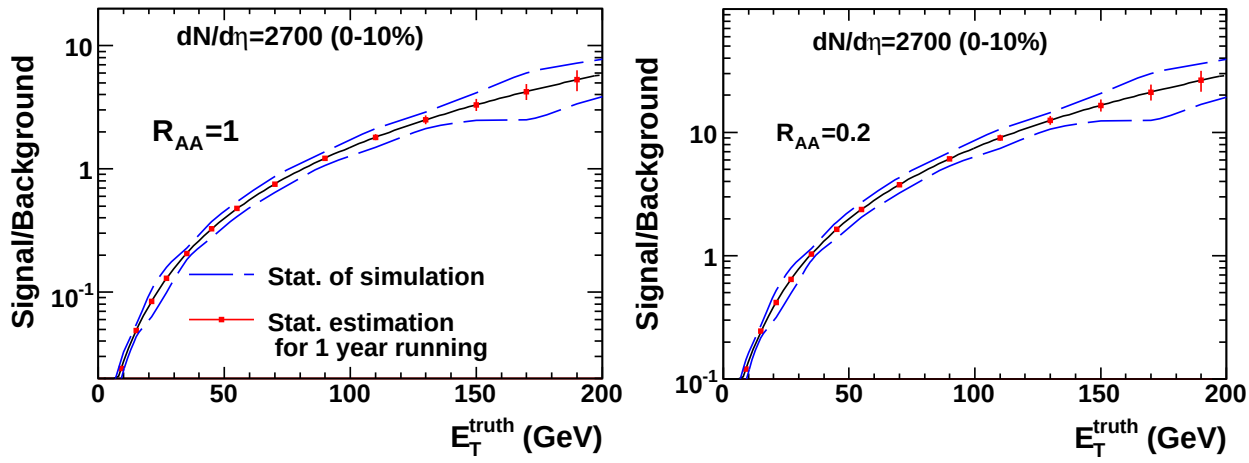

Figure 10.4: Prompt photon signal to background (S/B) vs. E_T for neutral hadron $R_{AA} = 1.0$ (left) and 0.2 (right) for 0–10% central Pb+Pb collisions. The background was obtained from $b = 2$ fm HIJING events with $dN_{ch}/d\eta = 2700$ while the photon yield was estimated for a 0-10% centrality bin using $N_{\rm coll}$ from Ref. [127]. The error bars indicate the expected statistical error *including errors in the background measurement and subtraction* calculated for one year nominal run (0.5 nb^{-1}); the dashed lines indicate the size of the statistical errors in our current simulation.

displaced vertices will allow a statistical separation of c and b jets. This will allow all of the jet measurements described in this proposal to be carried out separately for c, b quarks and light quarks/gluons.

The studies shown in Chapter 3 demonstrate the capabilities of ATLAS in measuring prompt photon production in photon-jet processes over the range $|\eta| < 2.4$ using a combination of photon/neutral hadron separation and jet isolation. The results indicate that ATLAS can measure prompt photons with signal to background better than one for E_T above 40–50 GeV for all centralities (for realistic $R_{AA} = 0.2$) and can reasonably carry out measurements for photon p_T as low as 20-30 GeV/c. Figure 10.4 summarizes the results presented in Chapter 3 for the prompt photon signal to background in central (HIJING) Pb+Pb collisions for two different values of R_{AA}. The figure also indicates the statistical precision with which the signal and background can be measured. The background was obtained from $b = 2$ fm HIJING events with the indicated $dN_{ch}/d\eta$ but the photon yields correspond to a 0-10% centrality bin with $N_{\rm coll}$ taken from Ref. [127] . With the ability to measure and reject background neutral hadrons, ATLAS will be able to carry out unprecedented measurements of direct photon spectra as demonstrated in Fig. 10.5. This figure shows what ATLAS would measure for direct photon spectra in a nominal one year (0.5 nb^{-1}) run p_T for several Pb+Pb centrality bins for the pessimistic assumption of no suppression of neutral hadrons (R_{AA} of 1.0). The backgrounds in Fig. 10.5 were obtained from HIJING events with the quoted $dN_{ch}/d\eta$ values, but the photon yields correpsond to the quoted centrality bins using N_{coll} from [127]. The statistical errors reflect the errors in the measurement and subtraction of the neutral hadron background. Precision measurements of prompt photons production, fragmentation photons, γ-jet pairs will provide essential information on hard scattering rates and jet quenching in Pb+Pb collisions at the LHC.

Chapter 5 demonstrated the ATLAS performance for Y and J/ψ measurements showing the

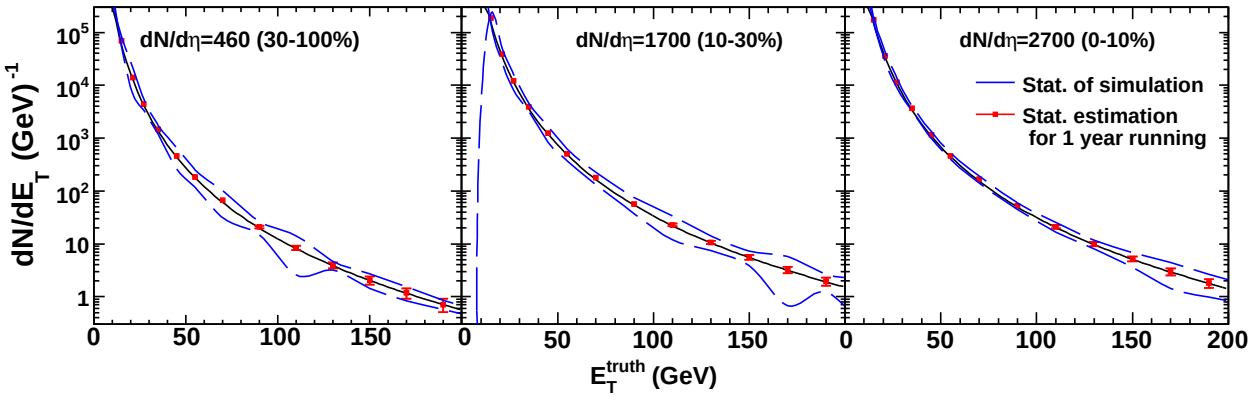

Figure 10.5: Summary of prompt photon spectra vs. E_T for a variety of centrality bins in Pb+Pb collisions for the case where there is no neutral hadron suppression. The backgrounds were obtained from HIJING events with the quoted $dN_{ch}/d\eta$ while the photon yields were obtained for the quoted centrality bins using N_{coll} from Ref. [127]. The error bars indicate the expected statistical error *including errors in the background measurement and subtraction* calculated for one year nominal run (0.5 nb^{-1}). The dashed lines indicate the size of the statistical errors in our current simulation.

large acceptance of ATLAS for Y measurements and the good signal/background obtained using the ATLAS external muon spectrometers. The results in that chapter demonstrated that ATLAS can separate the three Y states when restricting the pseudo-rapidity range of the measurement. Using the full η range ATLAS will have sufficient resolution to separate the Y and Y′ but not the Y″. The demonstrated performance will allow ATLAS to make competitive measurements of the production and suppression of bottom quarkonia. Measured prompt photon spectra (e.g.) will provide a valuable benchmark for the measurement of Y suppression as a function of Pb+Pb collision centrality until a 5.5 TeV p+p run takes place at the LHC.

10.3 Justification for ATLAS Heavy Ion program

10.3.1 Physics justification

We list in Table 10.1 the important measurements that ATLAS will contribute to the LHC heavy ion program and our assessment of the significance of each measurement compared to the other LHC heavy ion experiments. Based on the technical capabilities of the ATLAS detectors, particularly the calorimeters,ATLAS has the potential to use full jet and photon-jet correlations to lead the study of jet quenching and parton-medium interactions at the LHC. The expertise of the US ATLAS-HI participants in this physics will be crucial in allowing ATLAS to realize this potential.

10.3.2 Programmatic justification

As discussed in the introduction, the institutions proposing to participate in a ATLAS heavy ion program will also maintain their participation in the RHIC program. We see the RHIC and LHC efforts as complementary parts of an overall heavy ion program where results from RHIC and

Significance	Measurement	Physics importance
Unique	Prompt photons, γ-ID only	Hard scattering rates, jet conversion photons
	Jet fragmentation photons	medium-induced photon emission
Best	γ-jet	Jet quenching, modified fragmentation functions
	Full jets, di/multi-jets	Jet suppression, angular broadening, medium response
	Tagged heavy flavor jets	Heavy quark quenching
Competitive	Global observables	Properties of initial state, development of collective motion.
	Jet fragmentation	Medium-modified fragmentation functions, medium-induced j_T broadening
	Y, Y′, and Y″	Debye screening

Table 10.1: Summary of physics measurements that ATLAS will make with physics consequences and our assessment of the significance of the measurements relative to other experiments.

the LHC will cross-fertilize each facility's scientific programs and, together, ultimately provide a single understanding of the properties of the QGP at temperatures a few times greater than T_c. In particular, we expect that jet quenching measurements at the LHC will dramatically improve the utility of jet quenching as a tomographic probe of the QGP both at RHIC and the LHC. The Y measurements at the LHC should finally provide clear insight on Debye screening of vector meson states in the QGP. Global measurements at the LHC will test our understanding of RHIC results in the context of a strongly coupled QGP. Thus, we see the LHC effort as providing important support for our RHIC efforts and will use our participation in both efforts to synthesize results from the two facilities.

We have described in the rest of this proposal and in the immediately preceeding material the strengths of the ATLAS detector and the places where ATLAS can either improve measurements at the LHC or contribute unique measurements. The LHC heavy ion program will be the last frontier in the field of experimental QGP physics for the foreseeable future. We believe that every tool available should be used to optimally extract the physics from the LHC. Since the properties of the created matter and the resulting Pb+Pb final state at the LHC is not known *a priori*, we don't know what problems the underlying event will create for jet measurements at the LHC or what new modifications of the final state might result from the passage of a very high energy jet. The difference in the calorimeter technologies and readout used in ATLAS and CMS (as a particular example) will provide the ability to control systematic errors in full jet measurements at the LHC. The unique photon measurements from ATLAS will provide the first comprehensive realization of the proposal that use $\gamma - jet$ measurements be used to improve the understanding of jet quenching. The unique ability of ATLAS to perform photon measurements in jets will direct measurements of medium-induced photon radiation. These measurements will be essential to establish jet quenching as a true tomographic probe of the quark gluon plasma.

10.3.3 Pragmatic justification

The institutions writing this proposal have pragmatic reasons to participate in a ATLAS heavy ion program, as each institution has a strong high energy ATLAS group. The synergy between the p+p and heavy ion groups has already paid dividends in facilitating rapid progress on physics performance studies in the last year. Since the institutions are already members of ATLAS, there is no bureaucratic impediment to having new ATLAS members working on the ATLAS Heavy Ion program whereas participation in another experiment at the LHC would entail substantial bureaucratic overhead and costs and reduce the ability of the institutions to leverage existing expertise. With the physics advantages provided by ATLAS in the measurement of jets and prompt photons and the competitive measurements in global observables and quarkonia, we see the ATLASheavy ion program as the optimal way to carry out a scientific program at the LHC. Based on the modest costs described in Section 9.4 for the US ATLAS-HI program, we are convinced that the US ATLAS-HI program provides the most cost-effective way for our institutions to pursue one of the primary physics goals of the US Nuclear Physics community in elucidating the properties of the quark-gluon plasma created in heavy ion collisions at the LHC.

Acknowledgements

The work presented in this proposal includes substantial contributions from non-US participants in the ATLAS heavy ion program that we wish to acknowledge here. Martin Spousta and Jiri Dolejsi from Charles University in Prague contributed to many aspects of the jet analysis. Barbara Wosiek, Andrzej Olszewski, Barbara Toczek, Adam Trzupek, and Krzysztof Woźniak from IFJ PAN, Kraków provided many of the results on global variables shown in Chapter 4. Laurent Rosselet from the University of Geneva carried out the early studies of Υ and J/ψ measurements that initiated the work presented in this proposal, and provided the studies of J/Ψ capabilities shown in this proposal. Helio Takai from Brookhaven National Laboraory and Laurent Rosselet initiated much of the effort that led to the development of the ATLAS heavy ion program. Fabiola Gianotti in her prior role as ATLAS Physics Coordinator strongly supported the early development of the ATLAS heavy ion program and the writing of the Heavy Ion Letter of Intent. We would like to thank the current ATLAS project management: the spokesperson, Peter Jenni, deputy spokespersons, Fabiola Gianotti and Steiner Stapnes, and Physics Coordinators, Karl Jacobs and Dave Charleton for their support of the ATLAS heavy ion program. We also thank Sam Aronson, Peter Bond, Thomas Ludlam, and Steve Vigdor for support from Brookhaven National Laboratory.

Appendix A

Detailed computing plan

These tables outline a full costing of computing resoures, fully burdened, between FY2009 and FY2012. All labor, maintenance, and replacement costs are included, as discussed in Chapter 8

Capital Costs (k$)	FY09	FY10	FY11	FY12
CPU	11.13	28.18	32.67	12.68
Disk	26.06	52.02	61.82	65.47
Tape	3.00	8.39	8.88	14.21
Total	40.19	88.60	103.37	92.36
boxes	2.73	8.01	8.01	3.20
Total Installation				
CPU (kSI2k)	65.48	321.70	706.03	936.62
Disk (TB)	48.26	192.77	421.73	785.44
Tape (TB)	29.38	111.63	235.01	432.41
Boxes (2U)	2.73	10.74	18.74	21.94
Operating Costs (k$)				
CPU	7.32	33.55	54.07	64.85
Disk	10.67	25.83	39.22	61.26
Tape	3.91	14.85	32.67	60.11
Total ($k)	21.89	74.23	125.96	186.22
Total Costs ($k, Capital & Ops)				
CPU	18.45	61.73	86.74	77.53
Disk	36.73	77.85	101.04	126.73
Tape	6.90	19.33	26.03	41.65
Total	62.08	158.92	213.81	245.91
Total/Capital	1.54	1.79	2.07	2.66

Table A.1: Detailed costs per year of US ATLAS-HI reconstruction and analysis computing, according to the plan in Figure 8.8

			FY08	FY09	FY10	FY11	FY12
TapeCost(k$)	unburdened		2.27	4.23	6.35	4.48	4.48
TapeCost(k$)	burdened		5.23	9.75	14.63	13.13	13.13
Cpu Installed	kSI2		0.00	154.95	302.68	454.03	454.03
New Cpu	kSI2		154.95	147.74	151.34	0.00	154.95
Cpu (k$)	Installed		37.19	62.30	78.95	78.95	54.93
Cpu (k$)	New		37.19	25.12	16.65	0.00	13.17
Cpu (k$)	operating	20% of capital.	7.44	12.46	15.79	15.79	10.99
Boxes	additional		9.68	6.16	4.73	0.00	2.15
Boxes	total		9.68	15.84	20.57	20.57	13.04
Disk (K$)			15.40	16.20	14.76	5.33	7.38
Disk (K$)	op	20% of capital.	3.08	6.32	9.27	7.26	5.49
total capital			52.59	41.32	31.41	5.33	20.55
total op			10.52	18.78	25.06	23.05	16.48
tapes	at ACF		5.23	9.75	14.63	13.13	13.13
TOTAL COST	**($k)**		**68.33**	**69.85**	**71.10**	**41.52**	**50.17**

Table A.2: Detailed costs per year of US ATLAS-HI Monte Carlo computing, according to the plan in Figure 8.8

Bibliography

[1] *The Frontiers of Nuclear Science: A Long-Range Plan for the Next Decade*, 2007 NSAC Long Range Plan, `http://www.er.doe.gov/np/nsac/docs/Nuclear-Science.Low-Res.pdf`.

[2] *Superdense Matter: Neutrons Or Asymptotically Free Quarks?*, J. C. Collins and M. J. Perry, Phys. Rev. Lett. **34**, 1353 (1975).

[3] *Can a Neutron Star Be a Giant MIT Bag?*, G. Baym and S. A. Chin, Phys. Lett. **B62**, 241 (1976).

[4] *Quark Star Phenomenology*, B. Freedman and L. D. McLerran, Phys. Rev. **D17**, 1109 (1978).

[5] *Exponential Hadronic Spectrum and Quark Liberation*, N. Cabibbo and G. Parisi, Phys. Lett. **B59**, 67 (1975).

[6] *Quark-Gluon Plasma and Hadronic Production of Leptons, Photons and Psions*, E. V. Shuryak, Phys. Lett. **B78**, 150 (1978).

[7] *New forms of QCD matter discovered at RHIC*, M. Gyulassy and L. McLerran, Nucl. Phys. **A750**, 30 (2005), arXiv:nucl-th/0405013.

[8] *What RHIC experiments and theory tell us about properties of quark-gluon plasma?*, E. V. Shuryak, Nucl. Phys. **A750**, 64 (2005), arXiv:hep-ph/0405066.

[9] *Hadronic signals of deconfinement at RHIC*, B. Muller, Nucl. Phys. **A750**, 84 (2005), arXiv:nucl-th/0404015.

[10] *Formation of dense partonic matter in relativistic nucleus nucleus collisions at RHIC: Experimental evaluation by the PHENIX collaboration*, K. Adcox et al. (PHENIX), Nucl. Phys. **A757**, 184 (2005), arXiv:nucl-ex/0410003.

[11] *The PHOBOS perspective on discoveries at RHIC*, B. B. Back et al., Nucl. Phys. **A757**, 28 (2005), arXiv:nucl-ex/0410022.

[12] *Experimental and theoretical challenges in the search for the quark gluon plasma: The STAR collaboration's critical assessment of the evidence from RHIC collisions*, J. Adams et al. (STAR), Nucl. Phys. **A757**, 102 (2005), arXiv:nucl-ex/0501009.

[13] *Quark gluon plasma and color glass condensate at RHIC? The perspective from the BRAHMS experiment*, I. Arsene et al. (BRAHMS), Nucl. Phys. **A757**, 1 (2005), arXiv:nucl-ex/0410020.

[14] *Elliptic flow in Au + Au collisions at $\sqrt{s_{NN}}$ = 130 GeV*, K. H. Ackermann et al. (STAR), Phys. Rev. Lett. **86**, 402 (2001), arXiv:nucl-ex/0009011.

[15] *Flow measurements via two-particle azimuthal correlations in Au + Au collisions at $\sqrt{s_{NN}}$ = 130 GeV*, K. Adcox et al. (PHENIX), Phys. Rev. Lett. **89**, 212301 (2002), arXiv:nucl-ex/0204005.

[16] *Pseudorapidity and centrality dependence of the collective flow of charged particles in Au + Au collisions at $\sqrt{s_{NN}}$ = 130 GeV*, B. B. Back et al. (PHOBOS), Phys. Rev. Lett. **89**, 222301 (2002), arXiv:nucl-ex/0205021.

[17] *Saturation of elliptic flow at RHIC: Results from the covariant elastic parton cascade model MPC*, D. Molnar and M. Gyulassy, Nucl. Phys. **A697**, 495 (2002), arXiv:nucl-th/0104073.

[18] *Effect of shear viscosity on spectra, elliptic flow, and Hanbury Brown-Twiss radii*, D. Teaney, Phys. Rev. **C68**, 034913 (2003), arXiv:nucl-th/0301099.

[19] *The large N limit of superconformal field theories and supergravity*, J. M. Maldacena, Adv. Theor. Math. Phys. **2**, 231 (1998), arXiv:hep-th/9711200.

[20] *Gauge theory correlators from non-critical string theory*, S. S. Gubser, I. R. Klebanov, and A. M. Polyakov, Phys. Lett. **B428**, 105 (1998), arXiv:hep-th/9802109.

[21] *Anti-de Sitter space and holography*, E. Witten, Adv. Theor. Math. Phys. **2**, 253 (1998), arXiv:hep-th/9802150.

[22] *The shear viscosity of strongly coupled N = 4 supersymmetric Yang-Mills plasma*, G. Policastro, D. T. Son, and A. O. Starinets, Phys. Rev. Lett. **87**, 081601 (2001), arXiv:hep-th/0104066.

[23] *From AdS/CFT correspondence to hydrodynamics*, G. Policastro, D. T. Son, and A. O. Starinets, JHEP **09**, 043 (2002), arXiv:hep-th/0205052.

[24] *Drag force in AdS/CFT*, S. S. Gubser, Phys. Rev. **D74**, 126005 (2006), arXiv:hep-th/0605182.

[25] *Calculating the jet quenching parameter from AdS/CFT*, H. Liu, K. Rajagopal, and U. A. Wiedemann, Phys. Rev. Lett. **97**, 182301 (2006), arXiv:hep-ph/0605178.

[26] *Sonic booms and diffusion wakes generated by a heavy quark in thermal AdS/CFT*, S. S. Gubser, S. S. Pufu, and A. Yarom, Phys. Rev. Lett. **100**, 012301 (2008), arXiv:0706.4307.

[27] *Heavy ion collisions and AdS/CFT*, H. Liu, J. Phys. **G34**, S361 (2007), arXiv:hep-ph/0702210.

[28] *Suppression of hadrons with large transverse momentum in central Au + Au collisions at $\sqrt{s_{NN}}$ = 130 GeV*, K. Adcox et al. (PHENIX), Phys. Rev. Lett. **88**, 022301 (2002), arXiv:nucl-ex/0109003.

[29] *Suppressed π^0 production at large transverse momentum in central Au + Au collisions at $\sqrt{s_{NN}}$ = 200 GeV*, S. S. Adler et al. (PHENIX), Phys. Rev. Lett. **91**, 072301 (2003), arXiv:nucl-ex/0304022.

[30] *Centrality dependence of high p_T hadron suppression in Au + Au collisions at $\sqrt{s_{NN}}$ = 130 GeV*, C. Adler et al. (STAR), Phys. Rev. Lett. **89**, 202301 (2002), arXiv:nucl-ex/0206011.

[31] *Disappearance of back-to-back high p_T hadron correlations in central Au + Au collisions at $\sqrt{s_{NN}}$ = 200-GeV*, C. Adler et al. (STAR), Phys. Rev. Lett. **90**, 082302 (2003), arXiv:nucl-ex/0210033.

[32] *High-p_T charged hadron suppression in Au + Au collisions at $\sqrt{s_{NN}}$ = 200 GeV*, S. S. Adler et al. (PHENIX), Phys. Rev. **C69**, 034910 (2004), arXiv:nucl-ex/0308006.

[33] *Transverse momentum and collision energy dependence of high p_T hadron suppression in Au + Au collisions at ultrarelativistic energies*, J. Adams et al. (STAR), Phys. Rev. Lett. **91**, 172302 (2003), arXiv:nucl-ex/0305015.

[34] *Nuclear modification of electron spectra and implications for heavy quark energy loss in Au + Au collisions at $\sqrt{s_{NN}}$ = 200 GeV*, S. S. Adler et al. (PHENIX), Phys. Rev. Lett. **96**, 032301 (2006), arXiv:nucl-ex/0510047.

[35] *Modifications to di-jet hadron pair correlations in Au + Au collisions at $\sqrt{s_{NN}}$ = 200 GeV*, S. S. Adler et al. (PHENIX), Phys. Rev. Lett. **97**, 052301 (2006), arXiv:nucl-ex/0507004.

[36] *Minijet deformation and charge-independent angular correlations on momentum subspace (eta, phi) in Au-Au collisions at $\sqrt{s_{NN}}$ = 130 GeV*, J. Adams et al. (STAR), Phys. Rev. **C73**, 064907 (2006), arXiv:nucl-ex/0411003.

[37] *Jet Quenching in Dense Matter*, M. Gyulassy and M. Plumer, Phys. Lett. **B243**, 432 (1990).

[38] *Multiple collisions and induced gluon Bremsstrahlung in QCD*, M. Gyulassy and X.-n. Wang, Nucl. Phys. **B420**, 583 (1994), arXiv:nucl-th/9306003.

[39] *Radiative energy loss of high energy quarks and gluons in a finite-volume quark-gluon plasma*, R. Baier, Y. L. Dokshitzer, A. H. Mueller, S. Peigne, and D. Schiff, Nucl. Phys. **B483**, 291 (1997), arXiv:hep-ph/9607355.

[40] *Reaction operator approach to non-Abelian energy loss*, M. Gyulassy, P. Levai, and I. Vitev, Nucl. Phys. **B594**, 371 (2001), arXiv:nucl-th/0006010.

[41] *Jet quenching and radiative energy loss in dense nuclear matter*, M. Gyulassy, I. Vitev, X.-N. Wang, and B.-W. Zhang (2003), arXiv:nucl-th/0302077.

[42] *Small Shear Viscosity of a Quark-Gluon Plasma Implies Strong Jet Quenching*, A. Majumder, B. Muller, and X.-N. Wang, Phys. Rev. Lett. **99**, 192301 (2007), arXiv:hep-ph/0703082.

[43] *High p_T probes of dense matter created in heavy ion collisions at RHIC*, B. A. Cole, Nucl. Phys. **A774**, 225 (2006).

[44] *The QCD collisional energy loss revised*, A. Peshier, Phys. Rev. Lett. **97**, 212301 (2006), arXiv:hep-ph/0605294.

[45] *Parton energy loss in an expanding quark-gluon plasma: Radiative vs collisional*, B. G. Zakharov, JETP Lett. **86**, 444 (2007), arXiv:0708.0816.

[46] *Radiative and Collisional Jet Energy Loss in the Quark- Gluon Plasma at RHIC*, G.-Y. Qin et al., Phys. Rev. Lett. **100**, 072301 (2008), arXiv:0710.0605.

[47] *Low-p_T collective flow induces high-p_T jet quenching*, N. Armesto, C. A. Salgado, and U. A. Wiedemann, Phys. Rev. **C72**, 064910 (2005), arXiv:hep-ph/0411341.

[48] *Flow dependence of high p_T parton energy loss in heavy- ion collisions*, T. Renk and J. Ruppert, Phys. Rev. **C72**, 044901 (2005), arXiv:hep-ph/0507075.

[49] *The fragility of high-p_T hadron spectra as a hard probe*, K. J. Eskola, H. Honkanen, C. A. Salgado, and U. A. Wiedemann, Nucl. Phys. **A747**, 511 (2005), arXiv:hep-ph/0406319.

[50] *Prospects of Jet Tomography Using Hard Processes inside a Soft Medium*, T. Renk and K. J. Eskola, PoS **LHC07**, 032 (2006), arXiv:0706.4380.

[51] *Transverse momentum and centrality dependence of high-pt non-photonic electron suppression in Au+Au collisions at $\sqrt{s_{NN}}$ = 200 GeV*, B. I. Abelev et al. (STAR), Phys. Rev. Lett. **98**, 192301 (2007), arXiv:nucl-ex/0607012.

[52] *Search for color charge dependence of energy loss at RHIC*, B. Mohanty (STAR) (2007), arXiv:0705.0953.

[53] *A d- Au data-driven prediction of cold nuclear matter effects on J/ψ production in Au - Au collisions at RHIC*, R. Granier de Cassagnac, J. Phys. **G34**, S955 (2007), arXiv:hep-ph/0701222.

[54] *Enhanced J/ψ production in deconfined quark matter*, R. L. Thews, M. Schroedter, and J. Rafelski, Phys. Rev. **C63**, 054905 (2001), arXiv:hep-ph/0007323.

[55] *Sequential charmonium dissociation*, F. Karsch, D. Kharzeev, and H. Satz, Phys. Lett. **B637**, 75 (2006), arXiv:hep-ph/0512239.

[56] *Can quarkonia survive deconfinement ?*, A. Mocsy and P. Petreczky, Phys. Rev. **D77**, 014501 (2008), arXiv:0705.2559.

[57] *Color Screening Melts Quarkonium*, A. Mocsy and P. Petreczky, Phys. Rev. Lett. **99**, 211602 (2007), arXiv:0706.2183.

[58] *The eccentricity in heavy-ion collisions from color glass condensate initial conditions*, H.-J. Drescher, A. Dumitru, A. Hayashigaki, and Y. Nara, Phys. Rev. **C74**, 044905 (2006), arXiv:nucl-th/0605012.

[59] *Manifestations of high density QCD in the first RHIC data*, D. Kharzeev and E. Levin, Phys. Lett. **B523**, 79 (2001), arXiv:nucl-th/0108006.

[60] *Relating high-energy lepton hadron, proton nucleus and nucleus nucleus collisions through geometric scaling*, N. Armesto, C. A. Salgado, and U. A. Wiedemann, Phys. Rev. Lett. **94**, 022002 (2005), arXiv:hep-ph/0407018.

[61] *Heavy Ion Collisions at the LHC - Last Call for Predictions*, e. . Armesto, N. et al., J. Phys. **G35**, 054001 (2008), arXiv:0711.0974.

[62] *Scaling of transverse energies and multiplicities with atomic number and energy in ultrarelativistic nuclear collisions*, K. J. Eskola, K. Kajantie, P. V. Ruuskanen, and K. Tuominen, Nucl. Phys. **B570**, 379 (2000), arXiv:hep-ph/9909456.

[63] *Hadron multiplicities, p_T spectra and net-baryon number in central Pb + Pb collisions at the LHC*, K. J. Eskola, H. Honkanen, H. Niemi, P. V. Ruuskanen, and S. S. Rasanen (2007), arXiv:0705.1770.

[64] *Hard probes in heavy ion collisions at the LHC: Jet physics*, A. Accardi et al. (2004), CERN Yellow Report CERN-2004-009, arXiv:hep-ph/0310274.

[65] *Medium modification of jet shapes and jet multiplicities*, C. A. Salgado and U. A. Wiedemann, Phys. Rev. Lett. **93**, 042301 (2004), arXiv:hep-ph/0310079.

[66] *Modified fragmentation function and jet quenching at RHIC*, X.-N. Wang, Nucl. Phys. **A702**, 238 (2002), arXiv:hep-ph/0208094.

[67] *Simulation of jet quenching and high-p_T particle production at RHIC and LHC*, I. P. Lokhtin, S. V. Petrushanko, A. M. Snigirev, and C. Y. Teplov, PoS **LHC07**, 003 (2006), arXiv:0706.0665.

[68] I.P. Lohktin, private communication.

[69] *Radiative energy loss and p_T-broadening of high energy partons in nuclei*, R. Baier, Y. L. Dokshitzer, A. H. Mueller, S. Peigne, and D. Schiff, Nucl. Phys. **B484**, 265 (1997), arXiv:hep-ph/9608322.

[70] *The production of J/ψ in 200-GeV/nucleon Oxygen +Uranium interactions*, C. Baglin et al. (NA38), Phys. Lett. **B220**, 471 (1989).

[71] *Heavy Ion Physics with the ATLAS Detector* (2004), ATLAS Collaboration, LHCC 2004-009I-013.

[72] *A detailed study of high-p_T neutral pion suppression and azimuthal anisotropy in Au + Au collisions at $\sqrt{s_{NN}}$ = 200 GeV*, S. S. Adler et al. (PHENIX), Phys. Rev. **C76**, 034904 (2007), arXiv:nucl-ex/0611007.

[73] *Two particle azimuthal correlations at high transverse momentum in Pb - Au at 158-AGeV/c*, M. Ploskon (CERES), Nucl. Phys. **A783**, 527 (2007), arXiv:nucl-ex/0701023.

[74] *Two- and three-particle azimuthal correlations of high- p_T charged hadrons in Pb+Au collisions at 158-AGeV/c*, S. Kniege and M. Ploskon (CERES), J. Phys. **G34**, S697 (2007), arXiv:nucl-ex/0703008.

[75] *Jets as a Probe of Quark Gluon Plasma*, D. A. Appel, Phys. Rev. **D33**, 717 (1986).

[76] *Mach cones and dijets: Jet quenching and fireball expansion dynamics*, T. Renk (2006), arXiv:hep-ph/0608333.

[77] *High transverse momentum η meson production in p+p, d +Au and Au+Au collisions at $\sqrt{s_{NN}}$ = 200 GeV*, S. S. Adler et al. (PHENIX), Phys. Rev. **C75**, 024909 (2007), arXiv:nucl-ex/0611006.

[78] *Evidence from d + Au measurements for final-state suppression of high p_T hadrons in Au + Au collisions at RHIC*, J. Adams et al. (STAR), Phys. Rev. Lett. **91**, 072304 (2003), arXiv:nucl-ex/0306024.

[79] *Jet properties from dihadron correlations in p + p collisions at $\sqrt{s}$ = 200 GeV*, S. S. Adler et al. (PHENIX), Phys. Rev. **D74**, 072002 (2006), arXiv:hep-ex/0605039.

[80] *Energy loss and flow of heavy quarks in Au + Au collisions at $\sqrt{s_{NN}}$ = 200 GeV*, A. Adare et al. (PHENIX), Phys. Rev. Lett. **98**, 172301 (2007), arXiv:nucl-ex/0611018.

[81] *Testing AdS/CFT Drag and pQCD Heavy Quark Energy Loss*, W. A. Horowitz and M. Gyulassy (2008), arXiv:0804.4330.

[82] *Heavy quark colorimetry of QCD matter*, Y. L. Dokshitzer and D. E. Kharzeev, Phys. Lett. **B519**, 199 (2001), arXiv:hep-ph/0106202.

[83] *Collective Flow signals the Quark Gluon Plasma*, H. Stoecker, Nucl. Phys. **A750**, 121 (2005), arXiv:nucl-th/0406018.

[84] *Conical flow induced by quenched QCD jets*, J. Casalderrey-Solana, E. V. Shuryak, and D. Teaney, J. Phys. Conf. Ser. **27**, 22 (2005), arXiv:hep-ph/0411315.

[85] *System size and energy dependence of jet-induced hadron pair correlation shapes in Cu + Cu and Au + Au collisions at $\sqrt{s_{NN}} = 200$ GeV and 62.4 GeV*, A. Adare et al. (PHENIX), Phys. Rev. Lett. **98**, 232302 (2007), arXiv:nucl-ex/0611019.

[86] *Two- and three-particle jet correlations from STAR*, J. G. Ulery (STAR), Nucl. Phys. **A774**, 581 (2006), arXiv:nucl-ex/0510055.

[87] *Identification of exotic jet topologies via three particle correlations in PHENIX*, N. N. Ajitanand (PHENIX), Acta Phys. Hung. **A27**, 197 (2006), arXiv:nucl-ex/0511029.

[88] *Near-side $\Delta\eta$ correlations of high-p_T hadrons from STAR*, J. Putschke (STAR), AIP Conf. Proc. **842**, 119 (2006).

[89] *High p_T Triggered $\Delta\eta$,$\Delta\phi$ Correlations over a Broad Range in $\Delta\eta$*, E. Wenger (PHOBOS) (2008), arXiv:0804.3038.

[90] *Low- and intermediate-p_T di-hadron distributions in Au + Au collisions at $\sqrt{s_{NN}}$ = 200 GeV from STAR*, M. J. Horner (STAR), J. Phys. **G34**, S995 (2007), arXiv:nucl-ex/0701069.

[91] *Quantitative Constraints on the Opacity of Hot Partonic Matter from Semi-Inclusive Single High Transverse Momentum Pion Suppression in Au+Au collisions at $\sqrt{s_{NN}}$ = 200 GeV*, A. Adare et al. (2008), arXiv:0801.1665.

[92] *Medium-evolved fragmentation functions*, N. Armesto, L. Cunqueiro, C. A. Salgado, and W.-C. Xiang, JHEP **02**, 48 (2008), arXiv:arXiv 0710.3073.

[93] *HIJING: A Monte Carlo model for multiple jet production in p+p, p+A and A+A collisions*, X.-N. Wang and M. Gyulassy, Phys. Rev. **D44**, 3501 (1991).

[94] *Jets from Quantum Chromodynamics*, G. Sterman and S. Weinberg, Phys. Rev. Lett. **39**, 1436 (1977).

[95] *QCD studies using a cone based jet finding algorithm for $e^+ + e^-$ collisions at LEP*, R. Akers et al. (OPAL), Z. Phys. **C63**, 197 (1994).

[96] *Experimental Investigation of the Energy Dependence of the Strong Coupling Strength*, S. Bethke et al. (JADE), Phys. Lett. **B213**, 235 (1988).

[97] *Longitudinally invariant k_T clustering algorithms for hadron hadron collisions*, S. Catani, Y. L. Dokshitzer, M. H. Seymour, and B. R. Webber, Nucl. Phys. **B406**, 187 (1993).

[98] *Successive combination jet algorithm for hadron collisions*, S. D. Ellis and D. E. Soper, Phys. Rev. **D48**, 3160 (1993), arXiv:hep-ph/9305266.

[99] *FastJet: Dispelling the N^3 myth for the k_T jet- finder*, M. Cacciari (2006), arXiv:hep-ph/0607071.

[100] *PYTHIA 6.3: Physics and manual*, T. Sjostrand, L. Lonnblad, S. Mrenna, and P. Skands (2003), arXiv:hep-ph/0308153.

[101] ATLAS offline reconstruction and analysis evenironment (Athena), version 12.0.6.

[102] *Prompt Photon Production at Large p_T Scheme Invariant QCD Predictions and Comparison with Experiment*, P. Aurenche, R. Baier, M. Fontannaz, and D. Schiff, Nucl. Phys. **B297**, 661 (1988).

[103] *Energy loss of leading hadrons and direct photon production in evolving quark-gluon plasma*, S. Turbide, C. Gale, S. Jeon, and G. D. Moore, Phys. Rev. **C72**, 014906 (2005), arXiv:hep-ph/0502248.

[104] *Multiplicity distributions for jet parton showers in a medium*, N. Borghini and U. A. Wiedemann, Nucl. Phys. **A774**, 549 (2006), arXiv:hep-ph/0509364.

[105] *Rapidity and angular distributions of charged secondaries according to the hydrodynamical model of particle production*, P. Carruthers and M. Doung-van, Phys. Rev. **D8**, 859 (1973).

[106] *Entropy production at high energy and mu(B)*, P. Steinberg, PoS **CPOD2006**, 036 (2006), arXiv:nucl-ex/0702019.

[107] *Charged-particle pseudorapidity distributions in Au + Au collisions at $\sqrt{s_{NN}}$ = 62.4 GeV*, B. B. Back et al. (PHOBOS), Phys. Rev. **C74**, 021901 (2006), arXiv:nucl-ex/0509034.

[108] *Centrality and energy dependence of charged-particle multiplicities in heavy ion collisions in the context of elementary reactions*, B. B. Back et al. (PHOBOS), Phys. Rev. **C74**, 021902 (2006).

[109] *The significance of the fragmentation region in ultrarelativistic heavy ion collisions*, B. B. Back et al., Phys. Rev. Lett. **91**, 052303 (2003), arXiv:nucl-ex/0210015.

[110] *Importance of Correlations and Fluctuations on the Initial Source Eccentricity in High-Energy Nucleus-Nucleus Collisions*, B. Alver et al., Phys. Rev. **C77**, 014906 (2008), arXiv:0711.3724.

[111] *Differential elliptic flow prediction at the LHC from parton transport*, D. Molnar (2007), arXiv:0707.1251.

[112] *ATLAS Technical Design Report Volume 1* (1997), ATLAS Collaboration, LHCC 97-16.

[113] *Glauber modeling in high energy nuclear collisions*, M. L. Miller, K. Reygers, S. J. Sanders, and P. Steinberg (2007), arXiv:nucl-ex/0701025.

[114] *The physics of the centrality dependence of elliptic flow*, S. A. Voloshin and A. M. Poskanzer, Phys. Lett. **B474**, 27 (2000), arXiv:nucl-th/9906075.

[115] *Methods for analyzing anisotropic flow in relativistic nuclear collisions*, A. M. Poskanzer and S. A. Voloshin, Phys. Rev. **C58**, 1671 (1998), arXiv:nucl-ex/9805001.

[116] *Directed flow at RHIC from Lee-Yang zeroes*, N. Borghini and J. Y. Ollitrault, Nucl. Phys. **A742**, 130 (2004), arXiv:nucl-th/0404087.

[117] *Simultaneous pattern recognition and track fitting by the Kalman filtering method*, P. Billoir and S. Qian, Nucl. Instrum. Meth. **A294**, 219 (1990).

[118] *Measuring the pseudo-rapidity density and transverse momentum spectrum of charged particles at* $\sqrt{s} = 14TeV$, M. Leyton (ATLAS) (2007), ATLAS Note, ATL-COM-PHYS-2007-051.

[119] *J/ψ Suppression by Quark-Gluon Plasma Formation*, T. Matsui and H. Satz, Phys. Lett. **B178**, 416 (1986).

[120] *J/ψ and eta$_c$ in the deconfined plasma from lattice QCD*, M. Asakawa and T. Hatsuda, Phys. Rev. Lett. **92**, 012001 (2004), arXiv:hep-lat/0308034.

[121] *Behavior of charmonium systems after deconfinement*, S. Datta, F. Karsch, P. Petreczky, and I. Wetzorke, Phys. Rev. **D69**, 094507 (2004), arXiv:hep-lat/0312037.

[122] *J / psi and Drell-Yan cross-sections in Pb+Pb interactions at 158 GeV/c per nucleon*, M. C. Abreu et al. (NA50), Phys. Lett. **B410**, 327 (1997).

[123] *Observation of a threshold effect in the anomalous J/ψ suppression*, M. C. Abreu et al. (NA50), Phys. Lett. **B450**, 456 (1999).

[124] *J/ψ production vs transverse momentum and rapidity in p+p collisions at* $\sqrt{s}$ *= 200 GeV*, A. Adare et al. (PHENIX), Phys. Rev. Lett. **98**, 232002 (2007), arXiv:hep-ex/0611020.

[125] *A new measurement of J/ψ suppression in Pb - Pb collisions at 158-GeV per nucleon*, B. Alessandro et al. (NA50), Eur. Phys. J. **C39**, 335 (2005), arXiv:hep-ex/0412036.

[126] *J/ψ production in Indium-Indium collisions at 158- GeV/nucleon*, R. Arnaldi et al. (NA60), Phys. Rev. Lett. **99**, 132302 (2007).

[127] *Hard scattering cross sections at LHC in the Glauber approach: From p+p to p+A and A+A collisions*, D. G. d'Enterria (2003), arXiv:nucl-ex/0302016.

[128] L. Rosselet, P. Nevski, and S. Timoshenko (ATLAS) (2008), ATLAS Analysis Note CERN-ATL-COM-PHYS-2008-002.

[129] *Zero Degree Calorimeters for ATLAS* (2007), CERN/LHCC/2007-001.

[130] *Eccentricity fluctuations and elliptic flow at RHIC*, R. S. Bhalerao and J.-Y. Ollitrault, Phys. Lett. **B641**, 260 (2006), arXiv:nucl-th/0607009.

[131] *Incident-energy and system-size dependence of directed flow*, G. Wang, J. Phys. **G34**, S1093 (2007), arXiv:nucl-ex/0701045.

[132] *Probing small x parton densities in ultraperipheral A+A and p+A collisions at the LHC*, M. Strikman, R. Vogt, and S. White, Phys. Rev. Lett. **96**, 082001 (2006), arXiv:hep-ph/0508296.

[133] *ATLAS high-level trigger, data acquisition and controls: Technical design report*, CERN-LHCC-2003-022.

[134] *ATLAS first-level trigger: Technical design report*, CERN-LHCC-98-14.

[135] *The LHC as a Nucleus-Nucleus Collider*, J. Jowett, plenary talk at the Quark Matter 2008 conference (2008).

[136] M. Ernst, Talk at RHIC Science and Technology Review, July 18-20, 2007 (`http://www.bnl.gov/npp/docs/RHICst07/ernst_DOE-Nuclear-Review-07-2007.pdf`).

[137] M. Ernst, private communication .

[138] Obtained from http://www.oanda.com/.

[139] *CMS physics technical design report: Addendum on high density QCD with heavy ions*, E. . d'Enterria, David G. et al., J. Phys. **G34**, 2307 (2007).

List of Figures

List of Tables